UNDERSTANDING THE ATOMISTIC STRUCTURES OF AMORPHOUS NANOMATERIALS

Karen M. Ehrhardt

A dissertation submitted to the faculty at the University of North Carolina at Chapel Hill in partial fulfillment of the requirement for the degree of Doctor of Philosophy in the Department of Chemistry in the School of Arts and Sciences.

Chapel Hill
2025

Approved by:

Scott C. Warren

James F. Cahoon

Jillian L. Dempsey

Joanna M. Atkin

Megan N. Jackson

© 2025
Karen M. Ehrhardt
ALL RIGHTS RESERVED

ABSTRACT

Karen M. Ehrhardt: Understanding the Atomistic Structures of Amorphous Nanomaterials
(Under the direction of Scott C. Warren)

Amorphous materials are distinguished by their disordered packing of atoms, which results in structures that lack periodicity. This disorder can give rise to properties that have demonstrated superior performance to crystals in numerous applications, from ion transport to catalytic activity. Despite these advantages, structure-property relationships in amorphous materials remain largely underexplored because amorphous structures do not produce Bragg scattering, which is routinely used to determine structure in crystals. As a result, extracting specific structural features has been exceedingly challenging with existing methodologies. This issue is compounded at the nanoscale, where both fabrication and characterization techniques are limited. In this work, we address these challenges by developing strategies to prepare and characterize amorphous nanomaterials.

To enable experimental investigations, we first design a fabrication process for freestanding large-area, ultrathin amorphous materials by atomic layer deposition (ALD). By irradiating single-crystal NaCl substrates with plasma, we form surface F-centers that are subsequently replaced by embedded hydroxyls that act as reactive sites to nucleate ALD. Using a polymer-assisted transfer method, the NaCl substrate can be gently removed to produce a freestanding ALD material than can be transferred to an arbitrary substrate.

We then develop pyHRMC, a software for obtaining experimentally-derived atomistic models of amorphous nanomaterials. We develop this software to perform Hybrid Reverse Monte Carlo (HRMC) using electron scattering, which iteratively fits a structure to scattering data. By

using electron scattering, we are able to investigate materials with small sample areas and volumes, in contrast to strategies that rely on X-ray and neutron scattering. Additionally, our implementation demonstrates increased accuracy in replicating a ground-truth structure of Al_2O_3 compared to a conventional Reverse Monte Carlo method.

We lastly apply these methods to characterize the structure of amorphous alumina from ALD. Alumina prepared by ALD typically contains nontrivial amounts of hydrogen, but measuring this hydrogen is difficult because it scatters very weakly. Using pyHRMC, we constrain the hydrogen positions using a machine-learned interatomic potential while simultaneously fitting structures to experimental electron scattering. We find that models with hydrogen form structures with different distributions of coordination number, resulting in lower average coordination than an Al_2O_3 model.

To Dad, my favorite teacher.

ACKNOWLEDGEMENTS

I have been incredibly fortunate during my time in Chapel Hill. Along each step of the graduate school journey, I have received overwhelming support and encouragement from family, friends, and mentors. While it's impossible to name everybody who has been a part of my life for these past five years, please know that I feel immense gratitude to each and every one of you.

Scott, thank you for your tireless mentoring. I deeply appreciate how carefully you guide us through our development as researchers, from designing experiments to sharing our work. I'm especially grateful for your lessons in scientific communication. Your passion for science is contagious and I will carry the lessons from my time in your group with me wherever I go.

I also can't describe my graduate school experience without also thanking my labmates: Becca, Lauren, Jack, Matt, Jessica, Duncan, Connor, Don, Hye Sol, and Sam. Thank you for endless conversations about research and graduate school, fun social activities, and always being an understanding shoulder to lean on. I have learned so much about collaboration and sharing knowledge through each of you.

I've been fortunate enough to be a part of a vibrant community in a broader Triangle area as well. The ultimate community in NC is unmatched in terms of opportunity, dedication, and generosity. To everyone who has been a part of Phoenix and Radiance: thank you for being the best friends, teammates, and coaches that I could ever ask for. Soo and DA, it's been amazing to be on a team with the people I've admired for such a long time. Having this community and sport is truly what helped me through the roughest patches of graduate school.

I also need to thank the Carrboro crew in particular. Maya, Annie, and Anna: it's been a joy to live with you and surely one of the best periods of my life. From jam nights to dinner parties, every single day at Pine Street has been an adventure in the best way. Rev, X, and Dawn: it's been so fun to have our Carrboro hangout nights. It's hard to find a group of people that can have so much fun without any plans at all. Lastly, Alex, thanks for being such a rock. You always bring light to my day.

Finally, I have endless gratitude and love for my family. Thank you for supporting me every step of the way, even during periods that were challenging for all of us. Taka, Kenji, and Obaachan: thank you for your constant encouragement. I'm always counting down the days until I can visit next. Grandma and Papa: thank you for supporting me throughout my education and always asking for research updates. Alyssa, you're my built-in best friend forever and I wouldn't have it any other way. I admire your resilience and kindness so much. Mom, you're the support behind every success that I've had. You're always there through highs and lows, and for that, I'm forever grateful.

And Dad, although you can't read this, I know you'd be proud.

TABLE OF CONTENTS

LIST OF TABLES xiii

LIST OF FIGURES xiv

LIST OF ABBREVIATIONS xvi

CHAPTER 1: INTRODUCTION 1

1.1 Motivation 1

1.2 Pair Distribution Functions 3

1.2.1 Introduction to pair distribution functions 3

1.2.2 Foundations of total scattering 8

1.2.3 Nature of electron-atom interactions 9

1.2.4 The origin of total scattering 11

1.2.5 Physical insight through diffraction and ePDF 13

1.2.6 Errors in the ePDF analysis 15

1.2.7 Available software packages 16

1.2.8 X-ray and neutron pair distribution functions 18

1.3 Applications to disordered material systems 19

1.3.1 Highly local atomic arrangements in bulk metallic glasses 19

1.3.2 Metal oxides 23

1.3.3 Phase transitions 26

1.3.4 Ultrafast electron diffraction 30

1.3.5 Organic samples 32
1.4 Approaches to structural modeling 34
1.4.1 Existing techniques for ePDF-based modeling 35
1.4.2 Open questions in modeling structures from ePDFs 37
1.5 Research Overview 38
REFERENCES 41
CHAPTER 2: METHODS 49
2.1 Introduction 49
2.2 Construction of atomic layer deposition reactor 49
2.2.1 Reactor design 50
2.2.2 Leak testing 53
2.2.3 LabVIEW program 55
2.2.4 Validations of ALD conditions 56
2.2.5 Capacitively coupled plasma generator 57
2.3 Synthesis methods 59
2.3.1 Preparation of ALD materials of NaCl 59
2.3.2 Transfer of ALD materials 60
2.4 Transmission electron microscopy 62
2.4.1 Sample preparation 62

2.4.2 Electron scattering 63

2.4.3 Imaging 64

2.4.4 Pair distribution function analysis 65

2.5 Core Pythonic concepts.....66

2.5.1 Classes and object-oriented programming.....66

2.5.2 Parallelization 67

2.5.3 LAMMPS interfacing in Python.....70

REFERENCES 72

CHAPTER 3: FREESTANDING 2D GLASSES BY ATOMIC LAYER DEPOSITION 74

3.1 Introduction.....74

3.2 Results and discussion 77

3.2.1 Film-type growth on NaCl substrates with plasma pre-treatment 77

3.2.2 Mechanism of NaCl surface activation.....83

3.2.3 Hydroxylation of surface-activated NaCl 89

3.2.4 Fabrication of freestanding titania 93

3.3 Methods.....97

3.3.1 Preparation of alumina on NaCl 97

3.3.2 Preparation of titania on NaCl 97

3.3.3 NaCl removal and PMMA-assisted transfer 98

3.3.4 Materials characterization 98

3.3.5 Quantification of F-centers 99

3.3.6 DFT Calculations 100

3.4 Conclusions 100

REFERENCES 102

CHAPTER 4: PYHRMC: HYBRID REVERSE MONTE CARLO FOR ELECTRON TOTAL SCATTERING 110

4.1 Introduction 110

4.2 Methods 114

4.2.1 The HRMC algorithm 114

4.2.2 Implementation 117

4.2.2.1 Organization of pyHRMC 117

4.2.2.2 Experimental ePDF constraint 118

4.2.2.3 Structural energy constraint 120

4.2.2.4 Physical cosntraints 121

4.2.2.5 Parallelization 122

4.2.3 Usage 123

4.3 Demonstration with amorphous Al_2O_3 123

4.3.1 MLIP training and molecular dynamics....123

4.3.2 Comparing Al_2O_3 models from RMC and HRMC....124

4.4 Conclusions....131

REFERENCES....133

CHAPTER 5: THE STRUCTURE OF ALD ALUMINA....137

5.1 Introduction....137

5.2 Methods....139

5.2.1 Alumina preparation and TEM characterization....139

5.2.2 HRMC calculations....140

5.3 Results and Discussion....142

5.3.1 Convergence of PDF and residual energy....142

5.3.2 Structural effects of hydrogen in alumina....144

5.4 Conclusions....146

REFERENCES....148

LIST OF TABLES

Table 1.1: Open-source software for calculating electron pair distribution functions.....17

Table 3.1: Quantified elemental composition from XPS of ALD alumina on Si wafer 82

Table 3.2: DFT-calculated energies of F-centers in NaCl.....89

Table 3.3: Quantified elemental composition from XPS of ALD titania on Si wafer 95

Table 5.1: Coordination number constraints for HRMC calculations 142

LIST OF FIGURES

Figure 1.1: Steps involved in calculated a pair distribution function 5

Figure 1.2: Types of electron scattering and effects of interference 11

Figure 1.3: Types of common pair correlation functions for amorphous Al_2O_3 15

Figure 1.4: Electron pair distribution function from shear band in Vitreloy 105 BMG 22

Figure 1.5: Pair distribution functions of ZrO_2 nanocrystals before and after ligand exchange ...26

Figure 1.6: Reverse Monte Carlo of $Ge_2Sb_2Te_5$.....29

Figure 1.7: Time-differential pair distribution functions of excited twisted bilayer graphene 32

Figure 2.1: Schematic of custom atomic layer deposition reactor.....51

Figure 2.2: LabVIEW program to plot real-time reactor pressure reading.....52

Figure 2.3: Bleed-up leak testing of reactor.....55

Figure 2.4: LabVIEW program to control precursor valves for automated ALD.....56

Figure 2.5: Code block for parallelizing step generation in pyHRMC.....69

Figure 2.6: Code block for interfacing with LAMMPS in pyHRMC.....70

Figure 3.1: Scheme of fabrication and transfer processes for freestanding ALD materials 77

Figure 3.2: Bright-field optical microscopy and TEM images of ALD alumina 79

Figure 3.3: Electron pair distribution and TEM images of ultrathin ALD alumina.....80

Figure 3.4: XPS of ALD alumina on Si wafer 81

Figure 3.5: AFM-IR and corresponding topology scan of ALD alumina in Si wafer 83

Figure 3.6: AFM topology and UV-vis spectra of plasma-treated NaCl single crystals.....84

Figure 3.7: Modeled absorption coefficients of Na colloids with Mite theory 86

Figure 3.8: Bright field and polarized light microscopy before and after plasma treatment 87

Figure 3.9: XPS of O 1s in NaCl with varying plasma treatments 90

Figure 3.10: Electron pair distribution function and TEM analysis of ALD titania 94

Figure 3.11: XPS of ALD titania on Si wafer 96

Figure 4.1: The Hybrid Reverse Monte Carlo algorithm.....115

Figure 4.2: Organization of modules in pyHRMC 117

Figure 4.3: Residual and energy of RMC and HRMC Al_2O_3 calculations 126

Figure 4.4: Coordination number and bond angle distributions of Al_2O_3 calculations 129

Figure 5.1: TEM characterization of alumina by ALD at 33 °C and 150 °C.....140

Figure 5.2: Convergence metrics of HRMC calculations on ALD alumina 143

Figure 5.3: Coordination number distributions of ALD alumina structures 144

Figure 5.4: CrystalNNFingerprints of ALD alumina by atom type 145

LIST OF ABBREVIATIONS

1D One dimensional

2D Two dimensional

3D Three dimensional

4D Four dimensional

4D-STEM Four dimensional-scanning transmission electron microscopy

ADF Bond angle distribution function

AET Atomic electron tomography

ALD Atomic layer deposition

AFM Atomic force microscopy

EDS Energy dispersive x-ray spectroscopy

EPSR Empirical potential structure refinement

BF Bright-field

BMG Bulk metallic glass

CCD Charge-coupled device

CVD Chemical vapor deposition

DFT Density functional theory

DLD Delay-line detector

ePDF Electron pair distribution function

FLARE Fast learning of atomistical rare events

FT Fourier transform

FWHM Full width at half maximum

G(r) Reduced pair distribution function

g(r) Pair distribution function

GUI Graphical user interface

HAADF High-angle annular dark field

HRMC Hybrid Reverse Monte Carlo

IFT Inverse Fourier transform

IMFP Inelastic mean free path

IR Infrared spectroscopy

LAMMPS Large-scale atomic/molecular massively parallel simulator

MD Molecular dynamics

ML Machine-learning

MLIP Machine-learned interatomic potential

MS Molecular statics

NMR Nuclear magnetic resonance spectroscopy

PDF Pair distribution function

PEALD Plasma-enhanced atomic layer deposition

PMMA Poly(methyl)methacrylate

RDF Radial distribution function

R(r) Radial distribution function

RMC Reverse Monte Carlo

RMC-MS Reverse Monte Carl0-Molecular Statics

SAED Selected area electron diffraction

S(q) Structure factor

STEM Scanning transmission electron microscopy

TCS Total scattering cross-section

TDMA-Ti Tetrakis(dimethlyamino)titanium(IV)

TEM Transmission electron microscopy

TMA Trimethylaluminum

UED Ultrafast electron diffraction

VASP Vienna ab-initio simulation package

XPS X-ray photoelectron spectroscopy

XRD X-ray diffraction

CHAPTER 1: INTRODUCTION

1.1 Motivation

Understanding atomic structure – especially disorder – and its relationship to the properties of a given material is a core endeavor of materials research. Disorder arises readily at surfaces and interfaces and is therefore a fundamental part of almost every material. Moreover, disorder greatly influences material properties and performance, as exemplified by defects that promote carrier recombination in a solar cell.[1] In fact, from the solid-electrolyte interphase in batteries to the local structure of catalytic sites to the charged traps in transistors, understanding and controlling disorder are essential to the application of most materials.[2–7] Direct insight into the structure of these defects is therefore imperative to developing a complete understanding and improving the performance of materials across functional applications.

Despite the importance of disorder on material properties, characterizing short-range structure remains a challenge. Routine techniques for assessing structure, such as single crystal and powder x-ray diffraction, rely on periodicity and provide little insight into point defects, interfaces, and surfaces. Structures that lack periodicity must therefore be described in terms of local of atoms that do not strictly apply to the rest of the material, unlike crystalline structures in which unit cells repeat throughout. This distinction produces two notable consequences. First, in these situations, much of the language and concepts of materials characterization no longer apply. For example, the classification of crystalline materials into space groups cannot be replicated for amorphous structures, which lack distinct unit cells. Second, the variety of possible structures that disordered regions may possess challenges current abilities to extract information and describe the

overall arrangement, requiring a strategy that takes a local perspective. This complexity associated with investigating disorder has made it a cutting-edge research topic, but methods to perform these studies have been limited. Therefore, a need exists for techniques that provides information about local structure while also including insight into the many variations of local structure within a single material.

This challenge is further compounded in materials with ultrathin to 2D geometries. Such small sample quantities require high spatial resolution and strong probe-sample interactions to yield adequate signal. As described below, some structural characterization methods with these qualities exist, such as atomic electron tomography.[8] However, this and similar techniques face significant limitations in the detection of lighter elements and materials that are not stable under very high doses of electron irradiation. As a result, a large gap exists not only in the knowledge, but also the capability to rationally design ultrathin amorphous materials.

This work seeks to bridge this gap through the development of synthetic and computational methods. First, we present a deposition strategy to fabricate uniform and ultrathin amorphous materials as freestanding structures. The materials produced by this strategy are then used as a model system for our modelling package, which employs a Monte Carlo-type algorithm to solve for an experimental amorphous structure. Our software is able to include light elements, including H, and requires low doses of electron irradiation, thereby mitigating challenges in existing methods. This approach is enabled by the pair distribution function, which provides essential insights into structure and is described in detail below. Using our strategies to obtain structural models allows the experimental investigation of synthesis-structure and structure-property relationships of nanoscale amorphous materials, offering an avenue toward key design principles for amorphous materials applications.

In this chapter, we describe the qualities of ePDF and organize its range of applications in materials characterization. In section 1.2, we provide a brief overview of the theoretical basis for PDF and how it is calculated. We follow this discussion with a description of ePDF applications to several research fields in section 1.3, where ePDF has shed insight on difficult questions of a material's structure and how this information has been correlated to the mechanical, chemical, and electronic properties of these materials. Section 1.4 covers other techniques that offer a look at the local atomic environment of a material, particularly focusing on approaches that provide an unusual degree of structural insight when paired with ePDF. Finally, section 1.5 outlines the research that is described in the following chapters of this work, where novel synthetic and computational methods have been developed for the structural characterization of amorphous thin materials.

1.2 Pair Distribution Functions

1.2.1 Introduction to pair distribution functions

Although it may appear that diffraction-based techniques are not useful for characterizing amorphous and disordered materials, in fact, there are powerful strategies that can extract useful structural information from a diffraction pattern. One such tool is the pair distribution function (PDF), which is obtained from x-ray, neutron, or electron diffraction patterns and provides insight into the local structure by showing the prevalence of pairwise distances between atoms. When plotted, the graphs display peaks as a function of distance in real space, among other information based on the shape and size of the peaks.

While any type of radiation may be used to collect diffraction patterns for PDF, electrons hold a unique advantage over x-rays and neutrons for the study of disordered and heterogenous materials. When using PDF to examine local atomic structures in nanomaterials, one needs the

irradiation to be focused down to the size of the structure being probed. Therefore, transmission electron microscopy (TEM) is a natural tool for this purpose, due to its ability to focus electron beams to nano- or angstrom-sized diameters. At present, only electrons can be focused to create a nanoscale beam. Electron diffraction patterns will therefore contain only information specific to a local nano-sized region, rather than averaged short-range structures that result from larger irradiated regions with x-ray or neutron diffraction. As we show in this review, the description of the structural relationship through electron pair distribution functions (ePDFs) is uniquely suited for the analysis of nanoscale disordered materials.

PDF profiles show the prevalence of interatomic distances in an irradiated area, giving a picture of the distribution of bond lengths. To calculate a PDF, one begins with a diffraction pattern, which contains both Bragg and diffuse scattering, a so-called total scattering approach (Figure 1.1). This diffraction pattern is then rotationally integrated and normalized into the total-scattering structure function in reciprocal space, which is a function of the wavevector Q. Through a Fourier transform, the structure function is converted into an atomic pair distribution function in real space. Computer modeling may be used as an additional step to generate 3D structures with theoretical PDFs that are fitted to the experimental PDF. Doing so offers a wide range of information that can be extrapolated from the model, including bond angles and distributions of short-range structural motifs.

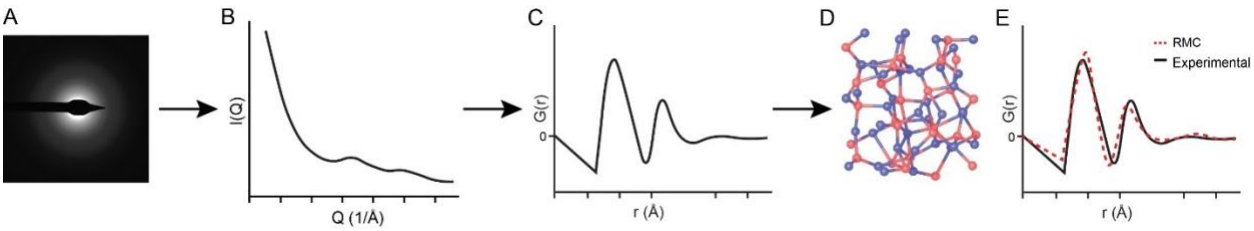


Figure 1.1. Illustration of the steps involved in calculating a pair distribution function (PDF) from electron diffraction. (A) A diffraction pattern is collected in a transmission electron microscope (TEM) and (B) rotationally integrated to produce a 1D intensity profile called the structure function. (C) A Fourier transform (FT) of the structure function produces the PDF, which indicates the prevalence of pairwise distances on the y axis over a range of real space distance of the x axis. (D) The PDF can be used an input for computer modeling methods such as Reverse Monte Carlo modeling and molecular dynamics, which (E) fit theoretical PDFs of structural models to the experimental PDF and yield further structural information.

Several kinds of information can be extracted from a PDF profile. The location of peaks indicates bond distances that are frequently encountered within the sample. Typically, these peaks signify coordination shells surrounding a central atom, with a common nearest neighbor corresponding to the first peak in the profile, the second prominent peak corresponding to second nearest neighbors, and so on. In some cases, the distance to which peaks extend in real space can give an indication of particle size. Additionally, in a single crystal with a preferred exposed facet, systematic differences in peak intensities will be observed due to an absence of bonds in a certain crystallographic direction. Especially when combined with a 3D structure from computational modeling, this information aids the understanding of typical facets within a crystalline material. Disorder of the materials is indicated by peak width, although this variable is also influenced by resolution limits. Sharp, narrow peaks are characteristic of crystalline structures due to their highly

periodic and consistent bond distances, while broad peaks indicate a range of bond distances within the nearest neighbor shell. In PDFs that have been normalized and corrected, the profile may be integrated to yield the average coordination number of an atom. Reduced density functions, which are closely related to PDFs, also yield sample density. Further structural information may also be extrapolated from structural modeling based on PDF information, as is expanded upon in section 1.4. This multitude of structural data from PDF offers a uniquely multifaceted and site-specific perspective on the atomic arrangement of amorphous materials, as well as crystalline materials that contain defects.

Early examples of PDF emerged gradually from x-ray diffraction.[9] Original x-ray diffraction experiments by Debye in the early 1900s set the stage.[10] Zernike and Prins soon after derived the relationship between pair correlations in real space and scattering functions in reciprocal space that foreshadowed distribution functions, but such efforts at the time were limited by the lack of advanced computer technology to process the data.[9,11] The poor resolution of x-ray diffraction during this period also contributed to general preferences to directly interpret diffraction patterns instead of rigorous post-processing. One of the first examples of x-ray PDF on amorphous materials include a study on amorphous Se, but it could not provide conclusive evidence of the atomic structure of the sample, indicating the poor quality of information yielded by PDFs at the time.[12] These challenges were overcome during the second half of the century with the development of computer modelling, using methods such as Reverse Monte Carlo and molecular dynamics.[13,14] As standard computer processing power increased, these models revolutionized the fields of PDF by allowing researchers to generate structural models and improved PDFs.

As electron diffraction entered the scene with the increasing presence of TEMs at research facilities, PDFs from molecules in the gas phase were obtained, but the application of ePDF to amorphous materials was not performed until the groundbreaking work by Moss and Graczyk on amorphous Si in 1969.[15,16] Nearly two decades later, Cockayne and McKenzie developed an improved diffraction setup by using an energy filter to reduce undesirable inelastic scattering.[17] As researchers sought to study smaller and smaller nanoregions of their materials, methods to deconvolute information for small, but convergent beams arose in the early 2000s.[18–20] In the 2010s, focus shifted to developing data correction methods that increase the accessibility to ePDF to users of TEMs without energy filters.[21–23] In recent years, detectors of modern CCD cameras and imaging plates allow ePDF patterns to be calculated from standard TEMs to provide a great deal of qualitative information while distinguishing nanometer-sized features.

TEM-based electron diffraction provides two features that facilitate its use in probing nanoscopic structures, which is unmatched by x-ray or neutron diffraction. Strong interactions between high-energy electrons and sample atoms result in large scattering cross sections, meaning that very little sample is required to acquire a diffraction pattern with an adequate signal-to-noise ratio. Precise control over beam parameters can produce coherent beams with sub-nanometer diameters, illuminating extremely small regions of the sample. Both of these features enable studies at the nanoscale to examine specific local structures that are otherwise impossible to distinguish. The ability of electron scattering to probe such small and specific sites is demonstrated clearly in the example of Al Josephson junctions.[24] In these materials, an ultrathin layer of AlO_x acts as an electronic barrier between two Al electrodes. The atomic structure of this barrier imparts critical tunneling properties to the junction, but the direct study of this material is difficult due to its thickness of less than 1 nm and placement between layers of Al. A study directly observed the

structure of this AlO_x layer for the first time using ePDF, demonstrating just one of many cases in which sample limitations require the precision of an electron probe.[24] Additionally, x-ray synchrotrons and neutron spallation sources are also less accessible to many researchers, requiring longer waiting periods and higher expenses, while TEMs are now commonplace at research facilities. These factors highlight the potential of the widespread adoption of ePDF within the materials research community.

1.2.2 Foundations of total scattering

The fields of electron, x-ray, and neutron diffraction are based primarily on Bragg diffraction—the simple relationship between periodic structures in a material and the resulting diffraction:

$$2d \sin\theta = n\lambda, \text{ (1-1)},$$

where d is the repeat distance, Θ measures the angle of diffraction, and λ is the wavelength of the radiation. Despite the utility of Bragg diffraction, real materials, whether single crystal, polycrystalline, or amorphous, also scatter radiation at angles that are not predicted by the Bragg equation. This non-Bragg scattering is called diffuse scattering, and the analysis of diffuse scattering can give insight into the disorder present in a material. Therefore, by measuring and analyzing both Bragg diffraction and diffuse scattering, an understanding of both order and disorder can be obtained. The strategy of using Bragg and diffuse scattering is often called total scattering because it utilizes most of the radiation scattered from a sample.[9] For an overview of additional basic concepts in electron diffraction, comprehensive textbook references exist for the reader.[25]

The total scattering of electrons shares the same theoretical foundation as the total scattering of x-rays or neutrons. This shared foundation has been the subject of several excellent

books and reviews, and we direct the reader to these helpful resources.[9,26] Here, we focus our discussion on the total scattering of electrons in a TEM and the ePDF method of data interpretation. The discussion in this section has the following parts: (1) the nature of the electron-atom interaction, (2) the origin of total scattering, (3) a description of how to understand physical structure of both crystalline and amorphous materials by taking the Fourier transform of the diffraction pattern, which leads to the ePDF analysis, (4) a discussion of the errors associated with ePDF analyses, including the challenges of multiple scattering, (5) an overview of software packages that are available for ePDF analysis, and (6) a brief discussion of the qualities of x-ray and neutron scattering for ePDF.

1.2.3 Nature of electron-atom interactions

Electrons scatter from atoms because of both Coulombic and magnetic interactions. Because most samples are only weakly magnetic, electron-sample interactions usually arise solely from Coulombic effects. These charge-based interactions occur when a TEM electron passes within an atom's electron cloud. Inside the cloud, the electron is attracted towards the nucleus, deflecting the electron in the direction of the nucleus.

Relative to x-rays and neutrons, the probability of electron scattering is quite large. For example, the scattering cross-section from carbon is approximately 1,000 to 100,000 times higher for an electron.[27] Likewise, the mean free path of a TEM electron within a material is typically between 10 and 100 nm, vs. 10 μm to 1 mm for x-rays. These differences have profound consequences for the TEM diffraction experiment. Most importantly, the strong interaction facilitates the analysis of extremely small quantities of sample—or of very small regions within a larger sample. This can provide important insight, especially in samples that are heterogeneous. However, because of the strong interaction, TEM samples must be extremely thin to avoid the

complicated diffraction patterns—called dynamical diffraction—that arise when electrons are scattered several times before exiting a sample. Indeed, most quantitative approaches for analysis of total scattering require that an electron has only been scattered once, which is called kinematic diffraction. Kinematic diffraction can be achieved not just by decreasing sample thickness, but also by increasing the electron beam's accelerating energy. Faster electrons spend less time within a sample and therefore have a lower probability of being scattered.

Quantitative analysis of total scattering also requires a knowledge of a sample's composition because different atoms have different probabilities of scattering an electron. The scattering probability—which is often expressed as the electron scattering cross-section—depends strongly on an atom's polarizability because the scattering event causes the atom's wavefunction to become polarized. In general, polarizability depends on atomic number, Z, and oxidation state, and these parameters are therefore good predictors of scattering cross-section. For example, Na (Z=11) has a scattering cross-section that is about four times larger than Li (Z=3), and Na^+ has about half the scattering cross-section as neutral Na.[28] However, as Z increases, the influence of oxidation state becomes diminished, and it is typical to neglect oxidation state entirely in assessing an atom's scattering cross-section. Overall, the scattering cross-section increases faster than Z but slower than Z^2. This behavior is like that of x-rays, whose scattering cross-section scales as Z^2.

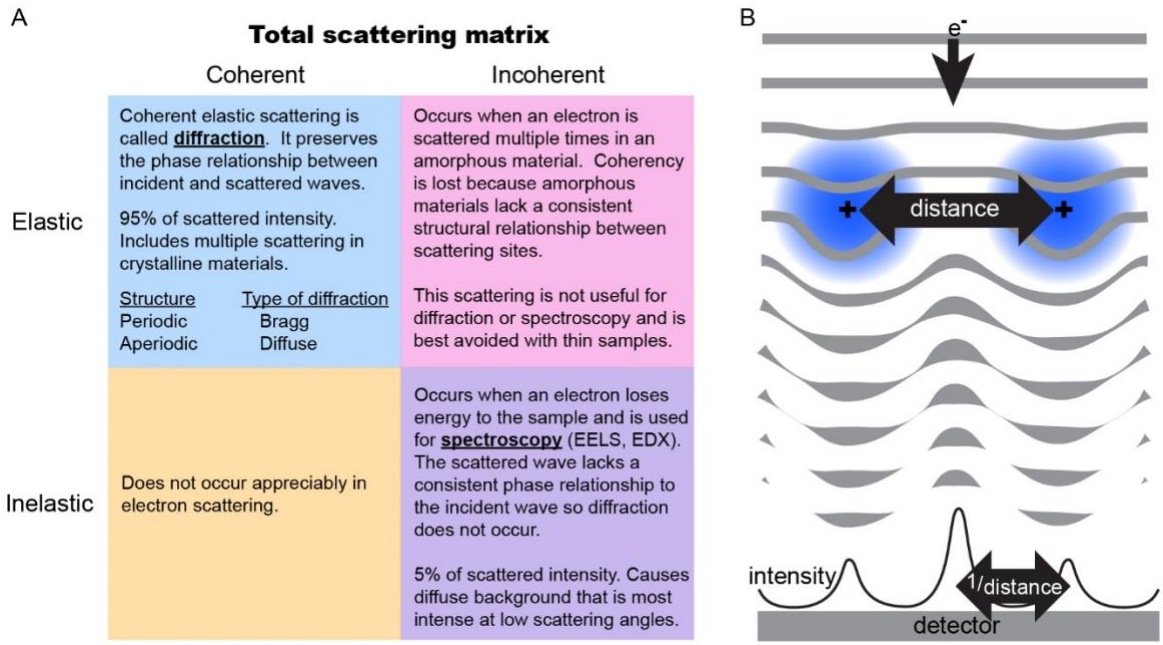


Figure 1.2. (A) Types of scattering that occur between TEM electrons and a sample. Insight into sample structure is obtained primarily through coherent elastic scattering, while insight into sample composition occurs primarily through inelastic incoherent scattering. (B) Illustration of diffraction arising from the interference between incident and scattered waves that occurs when an electron plane wave interacts with a pair of atoms. A Fourier transform of the diffraction pattern recovers real space distances.

1.2.4 The origin of total scattering

Although the brightness of an electron gun in a TEM can be quite high, individual electrons in the electron beam are typically well-separated in both space and time, and therefore pass through a sample one by one. As the electron passes through a sample, the electron has some probability of undergoing several processes: coherent elastic scattering (diffraction), inelastic incoherent scattering, and, in some samples, elastic incoherent scattering. In addition, diffraction can be divided into single scattering and multiple scattering.[26] Single scattering phenomena are described

by kinematic theory, which simplifies the event to wholly neglect multiple scattering events. In multiple scattering cases, a more rigorous approach is required using dynamical theory. These types of scattering are further described in Figure 1.2A.

The focus in this review is coherent elastic scattering (Figure 1.2B). This type of scattering maintains temporal coherency because there is no energy transfer, therefore any shift in the phase of scattered waves arises from path length differences; as such, the phase difference between scattered wavelets gives information about the relative position of two scatterers, as described by:

$$\Psi(Q) = \sum_v \frac{b_v}{\langle b \rangle} e^{iQ \cdot R_v} \text{ (1-2)},$$

where b_v is the scattering amplitude of atom v, $\langle b \rangle$ is the average scattering amplitude of all atoms, Q is the diffraction vector, which describes the direction of momentum transfer upon scattering, and R_v describes the position of the atom in the sample. When this summation is performed over all atoms in a crystalline sample, one finds that the amplitude of the scattered waves can be combined constructively, destructively, or some combination of the two (some phase difference other than 0° or 180°).

For electrons, we can divide the coherent elastic scattering into two parts: Bragg diffraction and diffuse diffraction. Here, we use the term 'diffuse diffraction' to distinguish this from the 'diffuse scattering', which is primarily caused by inelastic incoherent interactions with the sample. Despite their different names, the physical origin of diffuse and Bragg diffraction is the same: interference among incident and scattered waves. Bragg diffraction is likely most familiar: it is observed at well-defined scattering angles and arises through constructive interference from crystalline samples. Because Bragg diffraction probes a sample's periodicity, the information gained—e.g., an understanding of a unit cell—naturally capture that periodicity. Thus, Bragg diffraction is said to measure a sample's global structure. In contrast, diffuse diffraction does not

require periodicity as it arises from the constructive interference between pairs of scattering objects (e.g., atoms, Figure 1.2B). Because this contains no information about a sample's periodicity—only information about pair-wise interactions—diffuse diffraction is said to measure a sample's local structure. It is important to note that crystalline samples have almost entirely Bragg diffraction, while amorphous samples have almost entirely diffuse diffraction.

1.2.5 Physical insight through diffraction and ePDF

The basic strategy in interpreting a diffraction pattern is to convert its information into a model of the sample's structure. This is done by performing a Fourier transform (FT) of the diffraction pattern, because the diffraction pattern is just the inverse Fourier transform (IFT) of the real-space structure.[11] The FT/IFT converts a signal between two domains—for example, between time and frequency domains—by decomposing the signal into a combination of sine and cosine waves of varying frequency. Therefore, because the diffraction pattern contains information about spatial frequencies (inverse distances), an FT of the diffraction pattern will yield information about real-space distances in the sample:

$$\frac{I_{coherent}}{\langle b \rangle^2} \xrightarrow{FT} g(r) \text{ (1-3)},$$

where $I_{coherent}$ is the experimentally measured intensity of coherent scattering and g(r) is the pair distribution function. In this equation, $\langle b \rangle^2$ normalizes the scattered intensity by accounting for the increased scattering by heavy atoms. Thus, a FT of the structure factor gives information about the distances between atoms in a sample. The pair distribution function is defined as:

$$g(r) = \frac{1}{4\pi r^2 N \rho_0} \sum_\nu \sum_\mu \delta\left(r - \left|r_\mu - r_\nu\right|\right) \text{ (1-4)},$$

where r is the radial distance from an atom, N is the number of atoms in the sample, ρ_0 is the number of atoms per unit volume, r_ν and r_μ are the positions of the ν_{th} and μ_{th} atoms, and δ is the delta function. The delta function returns a value of one if the radial distance r is equal to the

distance between atoms ν and μ and returns zero otherwise. The double summation performs the delta function over all pairs of atoms within a sample. The factor that precedes the summation rescales the summation so that g(r) converges to a value of 1 at large r. For radial distances that are shorter than any bond, g(r) has a value of zero. Figure 1.3A shows an example of g(r) for an amorphous sample of alumina. The data identifies a first nearest neighbor distance of about 2 Å, and a second nearest neighbor distance of about 3 Å. At larger r, the peaks become less distinct because of the irregular spacing of atoms within the amorphous sample.

Although g(r) is the "simplest" type of PDF function, there are related functions that are more widely used. The challenge with g(r) is that one must know ρ_0, to calculate g(r). Instead, the reduced pair distribution function G(r) is more widely used since it can be calculated without this information. G(r) is defined as:

$$G(r) = 4\pi r\rho_0(g(r) - 1) \quad (1\text{-}5)$$

and is obtained by taking the Fourier transform of the scattered intensity, namely Q(S(Q)-1). G(r) also facilitates error analysis because the weighting of the G(r) function causes random uncertainties in G(r) to be constant as a function of r, and an example is given in Figure 1.3B for the same amorphous alumina material.

An additional type of PDF function is the radial distribution function, R(r). The radial distribution function is related to the g(r) by:

$$R(r) = 4\pi r^2\rho_0 g(r) \quad (1\text{-}6).$$

The advantage of the radial distribution is that integration of each peak gives the number of atoms found at that distance. In this way, one can determine the number of first- or second-nearest neighbor atoms, which facilitates the construction of complex 3D models of a material. An example is shown in Figure 1.3C.

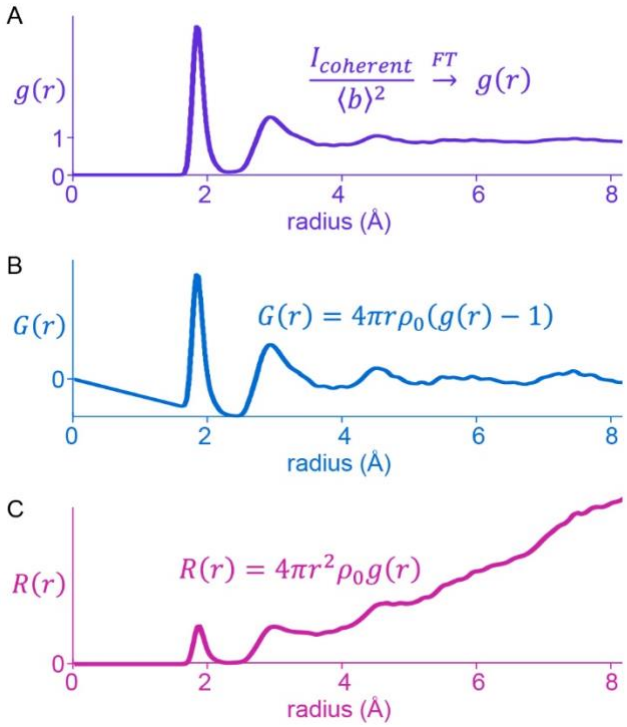


Figure 1.3. The three most common pair correlation functions, as illustrated for amorphous Al_2O_3. (A) The pair distribution function (PDF), g(r). (B) The reduced pair distribution function, G(r). (C) The radial distribution function (RDF), R(r). In the equations shown here, r is the distance (radius) from an atom and ρ_0 is the number of atoms per unit of volume.

1.2.6 Errors in the ePDF analysis

The creation of the ePDF involves several important errors. Typically, the most important error is called a termination error. This arises because the diffraction pattern is collected at a limited range of scattering angles—from $2\Theta_{min}$ to $2\Theta_{max}$, or, equivalently, from Q_{min} to Q_{max} (the minimum and maximum diffraction vectors, respectively). The absence of information beyond Q_{max} causes oscillations in the PDF of a frequency equal $1/Q_{max}$ (or $2\pi/Q_{max}$ for x-ray). These oscillations.

which increase in amplitude at high distance r, can be mistaken for peaks in the PDF and can lead to incorrect assignments of interatomic distances.

The primary solution to termination errors is to collect diffraction patterns out to a large Q_{max}—a value of about 30 $Å^{-1}$—at which the frequency and magnitude of these oscillations becomes quite small. This value of 30 $Å^{-1}$ is a rule of thumb, derived from the Debye-Waller factor.[9] Fortunately, the collection of diffraction data out to (or beyond) 30 $Å^{-1}$ is practical in most TEMs, because methods of tilting or offsetting the beam significantly increase the range of Q that is accessible.

A second important contribution is inelastic scattering. Because this is incoherent, it contributes intensity to the background and can be difficult to distinguish from diffraction. Ideally, inelastic scattering is removed with energy filtering. However, it has been found that removal of incoherent scattering is not always needed because it contributes a relatively small amount to the total scattering (ca. 5%).[28]

Overall, improvements in data collection and analysis are allowing practitioners of the ePDF technique to obtain quantitative models of crystalline and amorphous samples. Specific strategies and methods will be described in the following section.

1.2.7 Available software packages

The data processing step of ePDF analysis is thankfully supported by numerous software that encourage easy adoption of the technique. These programs generate ePDF profiles from inputted electron diffraction data, are open source, and are staple tools among users of this method. A list of available software is included in Table 1.1.

Table 1.1. Open-source software that is available to researchers and compatible with electron diffraction data for calculating ePDFs.

Software Package	Intended Method	Description
GSAS-II[29]	X-ray or neutron diffraction	A python package that calculates PDF from x-ray diffraction. Includes a wide range of features for crystallographic analysis beyond PDF analysis.
PDFgetX3[30]	X-ray or neutron diffraction	Batch-processing software for converting diffraction patterns to PDF, enabling high throughput. Can be used as a standalone program or implemented in xPDFsuite.
ProcessDiffraction[31]	Electron diffraction	Stand-alone program that calculates PDF from diffraction patterns. Includes a functionality to compare data with known structures from a XRD database.
SUePDF[32]	Electron diffraction	Matlab GUI that calculates PDFs. Simple interface suitable for new users but requires pre-processed intensity profiles as input. Automated empirical background subtraction may be performed with minimal effort.
eRDF Analyser[33]	Electron diffraction	Matlab GUI with a simple interface that calculates reduced density functions from either diffraction data or intensity profiles. It includes theoretically determined background subtraction and azimuthal variance output.
ePDF tools[34]	Electron diffraction	A package for DigitalMicrograph that calculates PDFs from diffraction patterns. Azimuthal rotation-averaging improves signal-to-noise ratios and real -time results aid user calibrations.
RDFTools[35]	Electron diffraction	A package for DigitalMicrograph that calculates reduced density functions from diffraction patterns. Available functionalities in intensity profile generation and G(r) calculation parameters allow users a high degree of control and rapid processing.
py4DSTEM[36]	4D-STEM	A python package with a suite of data analysis tools useful for initial processing of complex 4D data prior to PDF generation.

Additionally, the numerous software packages that exist for synchrotron x-ray PDF may also be applied for ePDF analysis. The similarity between PDFs created by electron- and x-ray

specific scattering software were shown to be satisfactory.[28] Specifically, GSAS-II and PDFgetX3 have been compared to ePDF-based SUePDF and provide similar results due to similarities between the physics of electron and x-ray scattering.[28]

1.2.8 X-ray and neutron pair distribution functions

As discussed, neutron and X-ray PDF analyses have previously been more common than ePDF, but these analyses must take place at x-ray synchrotrons and spallation neutron sources that are not readily available to most researchers. Still, these techniques can sometimes provide information that cannot be obtained by ePDF alone. Most notably, powerful x-ray and neutron sources are able to gain information at higher Q values in reciprocal space than a standard electron source.[9] This corresponds to higher resolution in real space, which can help to characterize disorder in highly crystalline materials, where peaks are sharp and defined. In amorphous materials, this level of resolution is not as beneficial because their peaks are broader and would not become sharper with higher resolution.

X-ray and neutron diffraction experiments additionally both have their own strengths, and may be a more suitable method than ePDF if specific information is needed. X-rays have the distinct advantage of being able to create differential PDFs, or pair correlation functions between a given element and all of its neighbors. Differential PDFs are created by tuning the excitation energy of the x-ray to perform PDF directly above and below the absorption edge of an element, therefore only elucidating bonds containing that element.[9] This additional information can be entered into RMC models to produce a more accurate structural representation of a sample.

Neutron diffraction is sensitive to a distinct set of elements, which may make it more valuable than electron or x-ray PDF for some materials. X-ray and electron scattering increases with heavier atoms, making light atoms extremely difficult or impossible to study. Neutrons,

though, do not face this issue and therefore can be an invaluable probe for materials with H, Li and other elements with low masses.[9] For example, White et al. used neutron PDF, rather than x-ray or electron, to detect the amount of water in aluminosilicate cements because of the particular sensitivity to hydrogen.[37]

In cases where x-ray or neutron PDF offers an advantage over ePDF for any of the reasons mentioned above, but local information is still desirable, various methods of PDF analysis can be combined for their respective strengths. This will create a more robust dataset of PDF measurements and bond length, and allows for comparison of different methods and their accuracies for a variety of materials. In fact, comparisons between x-ray PDF and TEM were an essential aspect of validating ePDF as a reliable source for interatomic spacings.

1.3 Applications to disordered material systems

In this section, we explore a range of systems on which ePDF has been applied. This overview begins with examples of common materials and phenomena encountered in materials, such as understanding short-range order and mechanical deformations in bulk metallic glasses (BMGs), metal oxides, phase transitions, and organic systems. The section concludes with a look at the combination of pump-probe analysis and PDF to track femtosecond processes in real time, which is expected to give mechanistic insights into the range of applications listed above.

1.3.1 Highly local atomic arrangements in bulk metallic glasses

BMGs are increasingly finding a wide scope of industrial applications, largely due to their unique set of physical properties. They are notable for their low critical cooling rates and outstanding mechanical properties such as high strength and corrosion resistance, which researchers have sought to understand through atomic structure.[38,39] Interesting structural configurations in BMGs occur at a short-range scale, necessitating a technique to inform the

arrangement of atoms within extremely small regions. Through ePDF, researchers have correlated numerous properties to the characteristic short-range clustering of a material, ranging from ductility and strain-induced shearing of atoms to permeability and free volume. Structural models yielded by ePDF and RMC may be analyzed to extract information in addition to bond distances, such as bond angles and polyhedral structural motifs.

To construct the local atomic structure of BMGs, Voronoi polyhedral analysis is commonly combined with the outputs of RMC from experimental ePDFs. An early example demonstrated the structures and fractions of $Zr_{70}Pd_{30}$, showing that the distribution of polyhedra centered around Pd does not change with annealing but the proportion of icosahedral structures surrounding Zr increases.[40] These results align with observations of a nanocrystalline icosahedral phase that precipitates out during annealing of this alloy. In another study, Hirata et al. used Voronoi analysis to identify several polyhedra with high fractions within a sample of $Zr_{66.7}Ni_{33.3}$ by weighing contributions of simulated diffraction patterns from individual motifs.[41] The authors were able to parse out the interconnected geometries of the polyhedra, finding that face-sharing is common in densely packed clusters. More recently, Voronoi analysis was combined with atomic electron tomography and ePDF for the study of monoatomic amorphous Ta and Pd materials.[42] The authors demonstrated that experimental PDFs of amorphous regions were consistent with a MD-generated PDF of Ta liquid, indicating that the packing of atoms in these two phases closely resemble each other. The commonality of bipyramidal motifs between phases that was observed in PDF and Voronoi analysis suggested a quenching mechanism that formed icosahedra from these motifs. These results were further supported through MD simulations. The use of Voronoi analysis on *ab initio* and experimentally-based RMC models should be broadly generalizable for glassy solid structures to obtain a statistical view of highly local atomic environments.

Averaged measurements, such as those obtained by x-ray PDF, are particularly difficult to apply to heterogenous materials because of the presence of nano-sized structures within the material. Such nanoscale regions arise for numerous reasons, including intentional synthetic design, phase separation, and areas of strain-induced plastic deformation, called shear bands. If localized structures such as these can be detected, the anisotropy in these materials may correlate to bulk properties and offer design principles for novel materials and applications. For example, the limited ductility of BMGs is a significant obstacle to their employment as functional materials and has been shown to closely relate to shear band formation.[43,44] However, the study of these nanoscale regions is impeded by the lack of contrast differences in TEM imaging when samples have uniform thickness.[45] An alternative method of directly studying the atomic arrangement is necessary to elucidate the mechanism behind shear band formation.

As a solution to this issue, ePDF has demonstrated the ability to detect measurable differences in shear bands compared to the rest of the material.[45–47] This approach was first employed by Chen et al., who studied $Pd_{40}Ni_{40}P_{20}$ BMG shear bands to find minor structural differences between shear bands and undeformed regions.[45] The low-Q peaks of the PDF showed slight broadening and lower intensities in the bands, indicating that greater variation exists in the short-range atomic arrangement of the BMG. From the diminished structural ordering, the authors could also infer a corresponding increase in free volume within the bands.

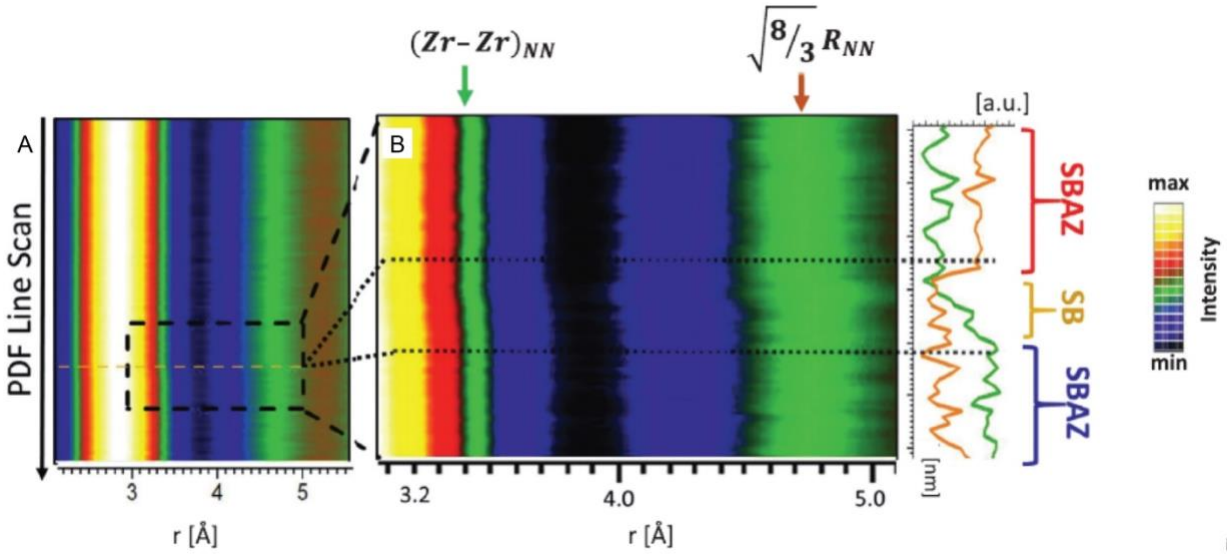


Figure 1.4. (A) Electron PDFs acquired while moving the electron beam across a shear band in a Vitreloy 105 BMG. (B) An expanded view of the selected region of A. The region between the dotted lines shows the PDF of the shear band, while regions above and below are shear band affected zones. The intensity at the pairwise distances are indicated by the green (3.4) and brown (4.8) arrows in (B), showing changes in the prevalence of Zr-based tetrahedra. Colors indicate the intensity of PDF peaks. Reproduced with permission from Mu et al.[47]

The regions immediately in the vicinity of shear bands, called shear band affected zones, also feature distinct atomic clusters compared to undeformed areas.[47] These regions serve to store residual energy from deformation in addition to the shear bands.[47] In one example, a scan over shear bands and shear band effected zones allowed the authors to create a two-dimensional ePDF that illustrated differences in intensity over an area of the material (Figure 1.4). This characterization, along with elemental mapping and nearest neighbor distribution analysis, showed that the most favorable face-sharing tetrahedra present in an undeformed Vitreloy BMG had a rapid concentration drop in deformed areas and were replaced by less efficient fragmented structures that increased free volume and allowed plastic flow.[47] These findings are promising for

future studies to fully unravel the structural relationships with the mechanical properties of amorphous materials.

1.3.2 Metal oxides

While amorphous metal oxides encompass a wide range of compositions and uses, the study of these materials is often united by the challenge of describing the material's structure. There is a need to directly observe coordination geometries of a binary system, benefitting from a technique that can distinguish prevalent bond distances and can be used in conjunction with additional information to model these structures. In an early example, ePDF was used to demonstrate the preparation of 2D SiO_2 on graphene.[48] Films of this thickness would be challenging to study with other methods due to the weaker sample-probe interactions of x-rays or neutrons. Other cases show that the short-range motifs within a sample vary due to preparation methods, leading to distinct difference in performance that opens avenues for tuning. Metal oxides also often suffer from similar issues like beam damage under the electron microscope, even at low accelerating voltages. Electron PDF has begun to take a larger role in studies that rationalize these relationships and processes.

Differences in synthetic procedures are the first of numerous factors contributing to different short-range structures. This effect is demonstrated in samples produced by atomic layer deposition (ALD), a common method for preparing films and coatings in semiconductors, textiles, and membranes.[28] Metal oxides grown under ALD conditions are well suited for ePDF study based on their amorphous nature and thin film geometry. Thin films are difficult to characterize with x-ray or neutron diffraction, which require larger sample sizes due to smaller scattering cross sections.

Jasim et al. show the synthetic considerations of Al_2O_3 fabricated by ALD through a series of ePDF experiments.[28] Lower temperatures resulted in lower Al-O bond lengths and coordination numbers, as well as lower O/Al ratios. These findings were attributed to two factors: (1) the quantity of hydroxyls remaining within the material, resulting in lower concentrations of aluminum hydroxide at these higher temperatures, and (2) decreased concentration of surface hydroxyl density that leads to single-site reactions (in which the precursor reacts with one hydroxyl) instead of the generally preferred two-site reaction (precursor reacts with two hydroxyls). Surface hydroxyl density controls growth during the trimethylaluminum half reaction, which requires adsorbed hydroxyl species to react. PDF analysis revealed the structural effect imparted on the materials by temperature conditions during deposition. These findings corroborate previous statements of an ideal temperature range for optimal growth rates due to the desorption of hydroxyl groups at elevated temperatures.[49,50] Similar studies on alternative sample preparation methods would give further insight into the diversity of short-range motifs that exist within Al_2O_3 and beyond.

In a study of amorphous Ta_2O_5 coatings, Bassiri et al. attribute short-range cluster formation to gas-phase reactions during ion-beam sputtering.[51] Broken Ta_2O_2 planar ring fragments form during deposition, creating an atomic arrangement that resembles the crystalline structure. This motif was identified through RMC models produced by ePDF data and supported by the large relative intensities of the relevant Ta-Ta and Ta-O bond peaks.

Relationships between atomic arrangement and the behavior of metal oxide species in physical and chemical processes have been elucidated through several studies. A form of amorphous IrO_x with hollandite-like regions has demonstrated great potential in catalyzing oxygen evolution reactions.[52] The uniquely high catalytic activity of this IrO_x form was determined by

Willinger et al. to stem from high-energy, undercoordinated short-range configurations. An interconnected geometry of corner-sharing results in lower coordination numbers than edge-sharing geometry, so the ratio of corner- and edge-sharing octahedra indicates an important role of the material in the redox reaction and stabilization of oxygen.

In another case, ligand exchange on nanocrystals have attracted attention for their effect on the structure of the inorganic center, such as in the study on ZrO_2 crystals by Schleder et al.[53] During the removal and attachment of ligands on a nanocrystal surface, the briefly undercoordinated surface structure may undergo rearrangement. This process leads to changes in the structural disorder of the nanocrystal surface, with accompanying shifts in the material's chemical and electronic properties. The amount of structural disorder was estimated from the length of structural coherence, which indicates the average distance between defects and is determined by the distance at which the PDF intensity reaches zero (Figure 1.5). The authors attribute the larger length of structural coherence and improved definition of peaks in the ePDF following ligand exchange to increased order and lower defect density in these ZrO_2 nanocrystals.

Relationships between structure and properties such as self-diffusion can be drawn from a combination of ePDF and secondary ion mass spectroscopy.[54] In a study on amorphous Al_2O_3, Ta_2O_5, and Nb_2O_5, ePDF was used to confirm that the structure remained amorphous after the heating of samples to promote diffusion. After heating, the authors measured the distribution of short-range bonds within each material from their respective ePDF profiles. The broader peaks in Ta_2O_5 and NbO_5 indicate wider distributions in bond lengths and corresponded to greater values of the diffusion coefficient compared to Al_2O_3. These results agree with the model that relates diffusion constants to ΔS due to the increased contribution of configurational entropy from more diverse short-range clustering.

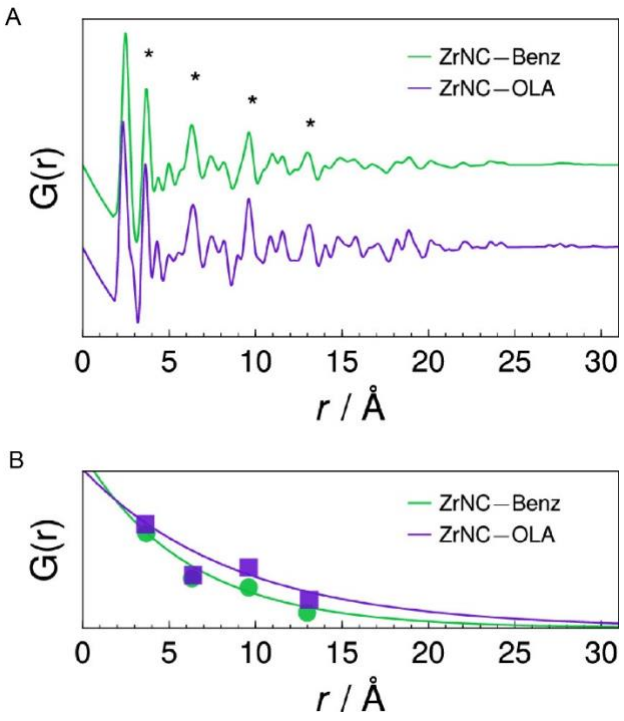


Figure 1.5. (A) PDFs of ZrO_2 nanocrystals with benzoic acid ligands before (green) and after (purple) ligand exchange for an oleic acid. Asterisks indicate peaks of Zr-Zr coordination shells, which are plotted as a function of intensity in (B). Functions of exponential decay were fitted to B to extract lengths of structural coherence. Reproduced from Schleder et al.[53] Copyright 2019 American Chemical Society.

1.3.3 Phase transitions

In the applications explored above, ePDF commonly found use in investigations of local atomic environments in specific forms of a material. However, the examples below suggest that new insight can be collected on phase transitions through *in situ* and comparative studies. Electron PDF has received attention particularly from communities interested in rapid phase change materials, solid-to-liquid transitions, and amorphous-to crystalline transitions.[55–59] The ability to

directly observe bond distances within disordered materials allows one to track the structural changes that occur before, during, and after these transitions.

Early examples of ePDF used to observe phase transitions include the study of a laser-induced solid-to-liquid transition in polycrystalline aluminum.[58] Laser excitation resulted in two significant changes in the eRDF profile: (1) the loss of long-range order, shown by the decay of peaks at high distance and (2) the decrease in coordination number from 12.2 ± 0.3 to 10.0 ± 0.3, determined by the integration of the nearest neighbor peak. This study demonstrated extraordinary spatial and temporal resolutions of the sub-angstrom and sub-picosecond scale, respectively (refer to section 4.4). While performed on a straightforward melting phase transition, this study foretold future investigations into complex phenomena, particularly those of other photoinduced structural transitions.

For slower processes, *in situ* electron irradiation via standard illumination in the TEM may also act as an excitation source to induce transitions, such as in the amorphous-to-crystalline transition of Al_2O_3.[59] The initial amorphous phase is composed largely of building blocks of mostly AlO_4 and AlO_5 clusters, while the stable γ-Al_2O_3 phase is mostly AlO_4 and AlO_6. A comparison of temporally spaced measurements during the irradiation of amorphous Al_2O_3 revealed increasing intensity of the Al-O bond peak during early stages, followed by a late-stage decreasing trend. The initial increase in peak intensity was attributed to the breaking apart and rearrangement of unstable AlO_5 clusters, creating an intermediate excited-state amorphous phase. From this rearrangement, crystallization into the γ-Al_2O_3 phase appeared through the decaying intensity of that same PDF peak, as smaller clusters were replaced by AlO_6 clusters. The emergence of long-range order after prolonged irradiation also suggested that a crystal phase had formed. This example shows the power of this technique in tracking highly localized atomic structures to understand their effects

on bulk material phases and the potential to uncover previously unknown phases and structures during physical processes. A comparison of PDFs over time allowed the authors to identify a new amorphous phase that sheds insight into the mechanism of phase transitions and crystallization.

The mechanism behind the amorphous-to-crystalline transition of $Ge_2Sb_2Te_5$, a material that undergoes rapid phase change and is highly important in optical and information technology, has also been explored by researchers striving to design rapid phase transitions in similar materials.[55–57] Prior to these studies, it was suggested that these materials are built from 4-membered building blocks from diffraction studies and theoretical calculations.[60–62] The distorted configuration of these rings in an amorphous phase may act as an energy storage site to drive the rapid crystallization process. Borisenko et al. proposed that the rotation of rings with respect to each other, which is described like the twisting of a Rubik's cube, as the factor responsible for rapid phase changes in this material.[55] This mechanism was examined by comparing the experimental ePDF to a computational model. The model was fitted from an initial structure of rotated planes of atoms to simulate the rotated rings and small random displacements to imitate diffusion. The final structure maintained the essential ring structure and showed agreement between simulated and experimental RDF profiles, revealing that these rings exist in amorphous phases (Figure 1.6). These findings were later supported by Hirata et al. through the use of the more recently developed angstrom-beam electron diffraction technique for extremely localized diffraction pattern collection.[57]

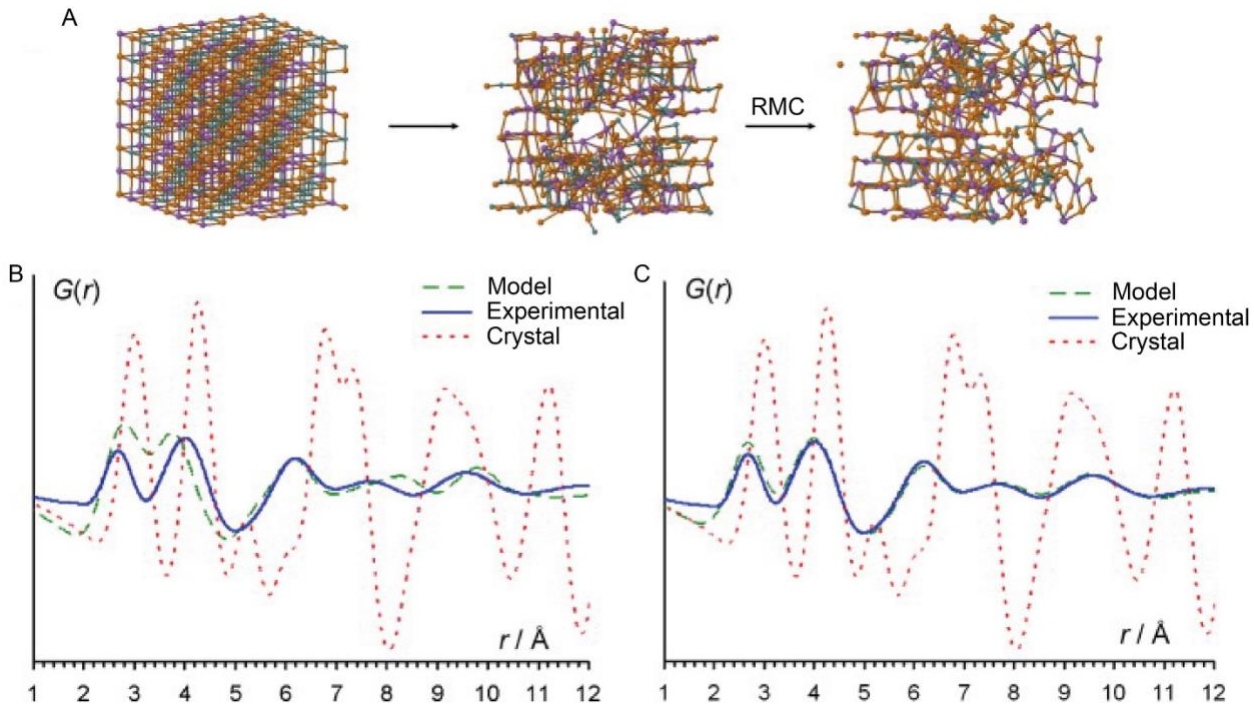


Figure 1.6. (A) The sequential structures of the theoretical model of $Ge_2Sb_2Te_5$, beginning with a crystalline structure and introducing plane rotations and small atomic displacements. The RMC is performed on the disordered initial structure. (B) Radial distribution functions (RDFs) of the disordered structure before RMC overlaid with the crystalline and experimental RDFs, demonstrating reasonable agreement even before a fitting procedure. (C) RDFs of the post-RMC structure with the experimental and crystalline RDFs. Reprinted from Borisenko et al., with permission from Elsevier.[55]

Nitrogen-doped $Ge_2Sb_2Te_2$ was similarly investigated with RDFs and corresponding RMC modeling.[56] This study was motivated by observations that increasing levels of N-doping results in an initial rise in resistance, followed by a drop in resistance as doping reaches higher levels. Similar to the study above, MD and RMC models were fitted to experimental RDFs and then analyzed to extract bond distributions, lengths, and angles. Preferential bonding of N to Ge results

in a GeN nanophase with common N-Ge-Ge-N ring structures, while the remaining $Ge_2Sb_2Te_5$ phase has increased concentrations of other types of ring building blocks. The presence of a well-distributed secondary phase may play a role in the observed changes in conductivity. These studies demonstrate the ability of distribution function analysis on amorphous materials to draw connections between structure and properties. Similar ring structures exist in other hard materials, opening the possibility of tuning these materials for similar rapid phase changes and applications in storage-based technology.

1.3.4 Ultrafast electron diffraction

The spatial resolution of electron diffraction-based distribution functions can be paired with an ultrafast diffraction technique to achieve information on femto- to picosecond time scales. Ultrafast electron diffraction (UED) involves the use of pump-probe optical excitation and subsequent detection using brief irradiation by an electron beam. The combination of this method with PDF is a powerful approach to mechanistic analyses, which have historically faced the challenge of tracking the structural changes during a process in real time. Such capabilities open a door to a multitude of mechanistic studies that would help answer questions surrounding transition states and pathways.

The validity of applying UED data for PDF analysis was determined by Farrow et al.[63] The authors tested the robustness of PDF in comparison to modified RDFs, which are typically used in UED analysis, with 20 Å Au nanoparticles under laser excitation. Similar modified RDF and PDF profiles over an array of data processing methods showed that peak distances are not sensitive to this difference, while peak width exhibits distortions that prevent quantitative analysis. The similar information provided by modified RDF and PDF allows researchers to generally use the two interchangeably.

A current drawback of UED is that it offers relative structural changes, rather than reliable absolute measurements due to the distortions observed in peak width. This drawback does not allow quantitative measurement of coordination spheres, but permits relative measurements of coordination numbers.[63] However, this information alone still offers significant potential in mechanistic studies of solid state processes, as demonstrated by Siwick et al.[58] The authors were able to compare eRDF profiles prior to and during ultrafast melting of Au nanoparticles.[58] During the phase change, long-range order disappeared and short-range order was preserved, which is consistent with the transition from crystalline to a glassy liquid-like structure. The picosecond timescale of the transition signifies that the process occurs through extreme thermal vibrations, due to the inability of atoms to diffuse through the material within the transition period.

Most recently, this technique has been applied to studying the graphite-to-diamond mechanism in twisted bilayer graphene.[64] Under femtosecond excitation, sp^3 bonds emerge between the layers to form a diamond-like structure. Differential PDFs show that newly formed C-C bonds are 1.94 Å, longer than standard distances of 1.54 Å in diamond (Figure 1.7B). This new distance arises due to a diminished interlayer distance and favorable AA and AB' local stacking in moiré patterns. Figure 1.7A shows the changes in peak intensity over the entire PDF, highlighting the bond distances of greater or lesser prevalence when the bilayer is excited (Figure 1.7B). Plots like this demonstrate the power of tracing rapid processes within the TEM and through ePDF. This study presents the exciting possibilities of ePDF in future investigations into photoinduced transitions of layered and 2D materials.

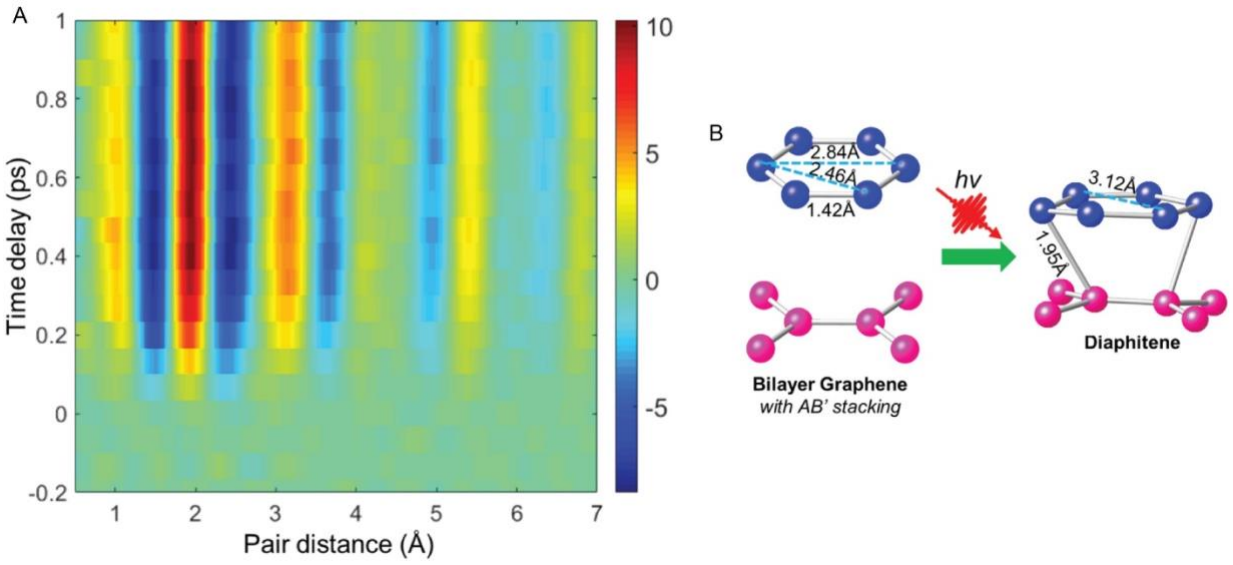


Figure 1.7. (A) Plot of ePDFs of excited twisted bilayer graphene probed with an electron beam over 1 ps. The colors indicate the intensity of signal in the PDF, showing the emergence and disappearance of certain pairwise distances. (B) Structural changes in stacked graphene before (left) an induced transition into diaphitene (right). Bond distances corresponding to hexagonal rings of graphene diminish and a simultaneous rise of a shortened interlayer distance and distorted ring structure are observed. Reprinted with permission from Luo et al.[64] Copyright 2020 by the American Physical Society.

1.3.5 Organic samples

While inorganic materials have largely been the samples of interest for electron diffraction analysis, ePDF offers unique insight into the structural arrangement of organic materials as well. Thus far, ePDF has been used to study pigment compounds and semiconductors.[65,66] This kind of information has significant applications in pharmaceutical development, which is increasingly looking towards amorphous and nanocrystalline components as alternatives to crystalline

compounds.[67] Therefore, ePDF is well suited as a characterization tool in these fields if beam damage can be sufficiently avoided.

Gorelik et al. gave the first demonstration of ePDF on organic and organometallic materials in a study on pigment compounds.[65] By using a series of compounds with varying beam sensitivities, the authors tested methods to minimize beam damage and confirmed the accuracy of ePDF. The nanodiffraction configuration reduces electron dose rates compared to SAED by inserting a small condenser aperture prior to sample exposure, instead of using a selected area aperture below the sample. Scanning-TEM (STEM) with high-angle annular dark-field (HAADF) detectors can also achieve low dose rates. The authors compared TEM, STEM, and x-ray PDFs for beam-stable chlorinated copper phthalocyanine and two less stable pigments, modified variants of copper phthalocyanine and quinacridone. Even in the case of the beam-sensitive samples, ePDF profiles matched x-ray results. This comparison indicates that standard techniques to achieve low dose rate will allow ePDF acquisition from challenging organic materials. The approach should also become increasingly applicable to beam-sensitive materials as technology progresses to allow improved detector sensitivity. Further steps taken to improve sample stability, including cryogenic temperatures, are expected to minimize sample damage as well. Though only able to reach qualitative results at present, this capability alone may play a useful role in pharmaceutical fingerprinting.[67]

A recent study by Mu et al. applies ePDF to the study of short-range order and medium-range order in polymer semiconductor thin films.[66] As discussed in section 5, the atomic structure and nanophase distribution throughout the sample was mapped and imaged using a scanning electron diffraction technique. This approach allows organic materials to be studied without staining. Such capabilities are notable because of frequent challenges in finding suitable stains for

certain materials.[68] Experimental peak positions of the films aligned well with simulated PDFs, providing bond lengths and additional information like bond angles through structural modeling. Beam damage resulted in minor changes to PDF peak intensities, indicating that this technique is unsuited for extracting coordination numbers.

As a whole, these studies on inorganic and organic materials show that ePDF is widely applicable to small specimens of amorphous character. This technique, paired with additional methods to provide additional information, promises unique opportunities for structural analyses among materials.

1.4 Approaches to structural modeling

As informative as ePDFs are, they do not provide the level of insight that is offered by atomistic models of structure. Given this fact, many studies of amorphous structure perform atomistic modeling in addition to ePDF analysis. In these cases, purely computational techniques, such as molecular dynamics (MD) simulations, are popular for generating a model. The computational results are often validated by comparing a theoretical PDF from the final structure to an experimental PDF. Despite the advantages of MD and related approaches, it remains true that the resulting structural model is fully derived from computation. In cases where synthetic method strongly influences structure, such simulations may struggle to differentiate structural characteristics between synthetic approaches. For this reason, several techniques have been developed to calculate experimentally-derived structures from ePDF. In this section, I begin by exploring the existing techniques that have been developed for atomistic modeling with ePDF. This overview is followed by a discussion of open questions and challenges in these modeling strategies, which have motivated my doctoral work presented in chapters four and five.

1.4.1 Existing techniques for ePDF-based modeling

One of the great advantages of the ePDF is that beyond the information that it directly provides, computational modeling can generate an experimentally-based structure of the material. With this added step, the complex profile of numerous atomic pair distances can be deconvoluted and 3-dimensional models of structure can be readily obtained, including bond angles, the type of atomic clusters within a material, and the prevalence of each cluster type.

Reverse Monte Carlo (RMC) modeling, first developed in 1988, is now possibly the most common method.[72] This process involves the evolutionary improvement of an initial structure by calculating its PDF profile, comparing it to the experimental PDF, and altering the structure to make an improved fit. Additional sample data from other measurement types, such as x-ray and neutron scattering, Raman spectroscopy, and even theoretical data may also be included as input to restrict the potential structural models to better represent that sample.[23] Although previously limited by the large amount of computational power required, this method has become practical in the recent decade and widely adopted by researchers.

Despite the recent prevalence of RMC, users must exercise caution when extrapolating information from models. One must note that this method produces a best fit, not a unique solution to the possible structure of the experimental results. Additionally, it is up to the researcher to determine the length scale at which reliable conclusions can be made. RMC can simulate a large volume of materials, but distances over which one can make conclusions of the structure are the same length scales as in the original PDF data. Appropriate constraints are also necessary to limit the possible solutions, including boundary conditions, bond length, and coordination numbers. A lack of constraints is likely to produce a structure that is not consistent with real physical and

chemical characteristics. With proper considerations, RMC can be a powerful tool to collect further insight from ePDF.

Given the limitations of RMC, several successive forms of modeling disordered structures have emerged from the traditional RMC algorithm. Empirical potential structure refinement (EPSR) uses an empirical potential function that it iteratively refined to improvement agreement with experimental structural properties.[73] This refined potential is then applied in a simulation until convergence. While this approach has found some success, the resulting potential is highly specific to the set of experimental conditions that it was refined against and at risk of overfitting. This process also effectively shifts the physics of the potential to fit the data, yielding potentials that may not match reality. Thus, potentials cannot be transferred between simulations and may be computationally costly as a result.

Another successor is RMC-molecular statics (MS), which employs intermittent relaxation steps between periods of standard RMC. By using molecular statics energy minimizations, this approach allows for large simulation cell sizes > 20,000 atoms. When demonstrated on amorphous ZnO, demonstrated lower structural energy than the pure RMC structure while achieving comparable residuals against experimental data.[74] The drawback of this strategy, however, is the long intervals between the RMC and MS steps. By switching between algorithms, much of the structural evolution towards convergence or low energy can be reverted by the other algorithm, resulting in significant inefficiencies.

This concern is removed from Hybrid Reverse Monte Carlo (HRMC), another method born from attempts to mitigate the limitations of traditional RMC.[75] In HRMC, an energy minimization constraint is applied simultaneously with the typical experimental error constraint. Applying both constraints for every step of the simulation prevents the inefficiencies of RMC-MS. Additionally,

the interatomic potential used to calculate the energy term is not changed over the course of the simulation, also avoiding concerns from EPSR. As the simulation progresses, the energy and error constraints are imposed more heavily, resulting in convergence.

1.4.2 Open questions in modeling structures from ePDFs

Despite significant advancements in modeling strategies since the 80's, multiple challenges still limit the applicability of ePDF-based modeling to amorphous systems. One prominent challenge lies in the modeling light atoms. This issue has also been documented in other techniques that rely of scattering data, such as atomic electron tomography (AET).[8] In AET, a series of images are collected over many angles, which are used to reconstruct a 3D structure. This approach is powerful for extracting 3D information from electron microscopy and has led to notable structural insights for disordered materials.[76] However, scattering techniques such as AET are inherently encumbered by poor signal from low-Z elements. Additionally, data acquisition requires large electron fluences, which can degrade the sample. As a result, scientific advances from this approach have largely been produced with highly beam stable materials with large Z contrast. While ePDF acquisition requires much smaller electron fluences and is therefore suitable for far less beam-stable materials, it suffers from the same challenge of being unable to adequately capture structural information of extremely light atoms.

Fortunately, HRMC is highly suited to address this challenge. In each Monte Carlo step, the structural energy is calculated using an interatomic potential. If this potential accurately reflects the forces on the light atoms, it can constrain the positions of the light atoms even when the ePDF cannot. To implement HRMC with energy calculations of light atoms, the modeling software must be designed to allow users to select a suitable potential. Currently, the most popular

implementation of HRMC is limited to a select few material systems, leaving the inclusion of other potentials as an existing capability gap.[77]

HRMC is therefore promising as a strategy, due to both the ability to constrain light atoms and the significant improvements to initial modeling algorithms described above. Both of these factors bias the calculated structures more strongly towards physically realistic configurations. To expand the applicability of HRMC to a broader range of materials, particularly ultrathin materials, an additional issue must be addressed. Because electron total scattering is most useful over x-ray or neutron scattering to characterize the structure of these materials, using electron-based experimental data to fit an HRMC structure is desirable. However, there is currently no software available that allows HRMC modeling with electron total scattering, the data required for an ePDF. To develop a software that can accurately model electron scattering, the correct scattering cross-sections must be calculated and included.

To address these challenges, my doctoral work has focused on developing a HRMC software that implements electron scattering cross-sections and an open-ended selection of potentials. As I describe in the following section, I have included chapters that discuss the implementation and application of this software to an amorphous ultrathin material with extremely light atoms.

1.5 Research Overview

The following chapters of this work advance our capabilities to study the structure of ultrathin amorphous structures. By offering synthetic and characterization methods, I contribute to a necessary workflow to discover synthesis-structure-property relationships that may guide the rational design of disordered and ultrathin materials.

Chapter two describes the methods employed in this work. The chapter begins with by describing the construction of our in-house custom ALD reactor, which provided a synthetic platform for the experimental samples analyzed in this thesis. Details include assembling the instrument, programming automated ALD, and engineering the in-situ capacitively coupled plasma generator. These contents are followed by the methods I used to fabricate and characterize the materials from ALD, as well as our tailored substrate for transferrable ALD materials. Finally, I discuss key Pythonic concepts for the HRMC Python package that I have recently developed.

Chapter three describes a fabrication approach to prepare amorphous ultrathin materials as freestanding structures. This work was motivated by a need for a freestanding structure with which to perform structural characterization without confounding signals from substrates and similar supports. Achieving this material is synthetically challenging, because methods that offer precise control over the uniformity and thickness of the materials often also result in strong interactions between the material and substrate. Here, I demonstrate the preparation of freestanding alumina using ALD. The versatile chemistries allowed by ALD, in combination with our strategy, opens an avenue to the fabrication of a wide range of freestanding amorphous ultrathin materials that offers applications beyond the demonstration of our characterization method.

In chapter four, I introduce pyHRMC, a Python package for HRMC of amorphous ultrathin materials using electron total scattering. Electrons interact with sample atoms more strongly than x-rays or neutrons and can be focused down to Angstrom-scale diameters, offering significant improvements in signal and spatial resolution over other scattering sources. Thus, electron scattering can provide insights into ultrathin and nanoscale structures that are otherwise extremely challenging to characterize. This package uniquely applies an HRMC algorithm with electron

scattering physics, enabling the accurate and experimentally-derived modeling of ultrathin amorphous structures.

Finally, in chapter five, I apply the synthetic ALD technique from chapter three and the HRMC modeling capability from chapter four to investigate the structure amorphous alumina as deposited by atomic ALD deposition. In ALD alumina, temperature-dependent quantities of hydrogen contamination are incorporated into the material during deposition.[78] However, electron scattering measurements cannot produce detectable signals from extremely light atoms such as hydrogen. As a result, previous experimental characterizations of ALD alumina have largely neglected the presence of hydrogen in their analyses. In this chapter, I employ the combined experimental and computational constraints of my HRMC program to solve for the atomistic structure of ALD alumina with hydrogen. This demonstration highlights the influence of light atoms on a material's structure and the distinct value of the HRMC approach.

REFERENCES

(1) Staebler, D. L.; Wronski, C. R. Reversible Conductivity Changes in Discharge-Produced Amorphous Si. *Appl. Phys. Lett* **1977**, *31* (4), 292–294.

(2) Li, Y.; Li, Y.; Pei, A.; Yan, K.; Sun, Y.; Wu, C.-L.; Joubert, L.-M.; Chin, R.; Koh, A. L.; Yu, Y.; Perrino, J.; Butz, B.; Chu, S.; Cui, Y. Atomic Structure of Sensitive Battey Materials and Interfaces Revealed by Cryo-Electron Microscopy. *Science* **2017**, *358* (6362), 506–510.

(3) An, S.; Li, J.; Daniel, C.; Mohanty, D.; Nagpure, S.; Wood, D. L. The State of Understanding of the Lithium-Ion-Battery Graphite Solid Electrolyte Interphase (SEI) and Its Relationship to Formation Cycling, 2016, *105*, 52–76.

(4) Kanan, M. W.; Nocera, D. G. In Situ Formation of an Oxygen-Evolving Catalyst in Neutral Ater Containing Phosphate and Co^{2+}. *Science* **2008**, *321* (5892), 1072–1075.

(5) Chemelewski, W. D.; Lee, H. C.; Lin, J. F.; Bard, A. J.; Mullins, C. B. Amorphous FeOOH Oxygen Evolution Reaction Catalyst for Photoelectrochemical Water Splitting. *J. Am. Chem. Soc* **2014**, *136* (7), 2843–2850.

(6) Frank, M. M.; Wilk, G. D.; Starodub, D.; Gustafsson, T.; Garfunkel, E.; Chabal, Y. J.; Grazul, J.; Muller, D. A. HfO_2 and Al_2O_3 Gate Dielectrics on GaAs Grown by Atomic Layer Deposition. *Appl. Phys. Lett* **2005**, *86*, 152904.

(7) Jae Sang, L.; Seongpil, C.; Sang-Mo, K.; Sang Yeol, L. High-Performance a-IGZO TFT With ZrO_2 Gate Dielectric Fabricated at Room Temperature. *IEEE Electron Device Lett* **2010**, *31* (3), 225–227.

(8) Miao, J.; Ercius, P.; Billinge, S. J. L. Atomic Electron Tomography: 3D Structures without Crystals. *Science* **2016**, *353* (6306), aaf2157. https://doi.org/10.1126/science.aaf2157.

(9) Egami, T.; Billinge, S. J. L. *Underneath the Bragg Peaks: Structural Analysis of Complex Materials*, 2nd edition.; Pergamon materials series; Elsevier: Amsterdam, 2012.

(10) Debye, P. Zerstruung von Röntgenstrahlen. *Ann. Phys* **1915**, *46*, 809–823.

(11) Zernike, V. F.; Prins, J. A. Die Beugung von Röntgenstrahlen in Flüssigkeiten als Effekt der Molekülanordnung. *Z. Phys* **1927**, *41*, 184–194.

(12) Hendus, H. Die struktur des explosiblen antimons und des glasigen selens. *Z. Phys* **1942**, *119*, 265–286.

(13) Kaplow, R.; Rowe, T. A.; Averbach, B. L. Atomic arrangement in vitreous selenium. *Phys. Rev* **1968**, *168* (3), 1068–1079.

(14) Zhang, X.; Drabold, D. A. Direct Molecular Dynamics Simulation of Light-Induced Structural Change in Amorphous Selenium. *Phys. Rev. Lett* **1999**, *83* (24), 5042–5045.

(15) Mark, H.; Wierl, R. Zuschriften. *Naturwissenschaften* **1930**, *18* (18), 205.

(16) Moss, S. C.; Graczyk, J. F. Evidence of Voids within the As-Deposited Structure of Glassy Silicon. *Phys. Rev. Lett* **1969**, *23* (20), 1167–1171.

(17) Cockayne, D. J. H.; McKenzie, D. R. Electron Diffraction Analysis of Polycrystalline and Amorphous Thin Films. *Acta. Cryst* **1988**, *A44*, 870–878.

(18) Petersen, T. C.; McBride, W.; McCulloch, D. G.; Snook, I. K.; Yarovsky, I. Refinements in the Collection of Energy Filtered Diffraction Patterns from Disordered Materials. *Ultramicroscopy* **2005**, *103* (4), 275–283.

(19) Ankele, J.; Mayer, J.; Lamparter, P.; Steeb, S. Quantitative electron diffraction data of amorphous materials. *Z. Naturforsch* **2005**, *60a*, 459–468.

(20) McBride, W. The Structure of Nanovolumes of Amorphous Materials. *J. Non-Cryst. Solids* **2003**, *318* (3), 233–238.

(21) Abeykoon, M.; Malliakas, C. D.; Juhás, P.; Božin, E. S.; Kanatzidis, M. G. Quantitative Nanostructure Characterization Using Atomic Pair Distribution Functions Obtained from Laboratory Electron Microscopes. *Z. Kristallogr* **2012**, *227*, 248–256.

(22) Abeykoon, A. M.; Hu, H.; Wu, L.; Zhu, Y.; Billinge, S. J. L. Calibration and Data Collection Protocols for Reliable Lattice Parameter Values in Electron Pair Distribution Function Studies. *J. Appl. Crystallogr* **2015**, *48* (1), 244–251.

(23) Juhas, P.; Farrow, C. L.; Yang, X.; Knox, K. R.; Billinge, S. J. Complex Modeling: A Strategy and Software Program for Combining Multiple Information Sources to Solve Ill Posed

Structure and Nanostructure Inverse Problems. *Acta Crystallogr. A Found. Adv* **2015**, *71* (Pt 6), 562–568.

(24) Zeng, L.; Tran, D. T.; Tai, C. W.; Svensson, G.; Olsson, E. Atomic Structure and Oxygen Deficiency of the Ultrathin Aluminium Oxide Barrier in Al/AlO_x/Al Josephson Junctions. *Sci. Rep* **2016**, *6*, 29679.

(25) Williams, D. B.; Carter, C. B. *Transmission Electron Microscopy: A Textbook for Materials Science*, 2nd ed.; Springer Science+Business: Media, LLC: New York, NY, 2009.

(26) Fultz, B.; Howe, J. M. *Transmission Electron Microscopy and Diffractometry of Materials*, 4th ed.; Springer-Verlag: Berlin Heidelberg, 2013.

(27) Jablonski, A.; Salvat, F.; Powell, C. J.; Lee, A. Y. NIST Electron Elastic-Scattering Cross-Section Database. In *NIST Standard Reference Database Number 64*; National Institute of Standards and Technology: Gaithersburg, MD, 2016.

(28) Jasim, A. M.; He, X.; Xing, Y.; White, T. A.; Young, M. J. Cryo-ePDF: Overcoming Electron Beam Damage to Study the Local Atomic Structure of Amorphous ALD Aluminum Oxide Thin Films within a TEM. *ACS Omega* **2021**, *6* (13), 8986–9000. https://doi.org/10.1021/acsomega.0c06124.

(29) Toby, B. H.; Dreele, R. B. GSAS-II: The Genesis of a Modern Open-Source All Purpose Crystallography Software Package. *J. Appl. Crystallogr* **2013**, *46* (2), 544–549.

(30) Juhás, P.; Davis, T.; Farrow, C. L.; Billinge, S. J. L. PDFgetX3: A Rapid and Highly Automatable Program for Processing Powder Diffraction Data into Total Scattering Pair Distribution Functions. *J, Appl. Crystallogr* **2013**, *46* (2), 560–566.

(31) Labar, J. L. In "ProcessDiffraction": A Computer Program to Process Electron Diffraction Patterns from Poylcrystalline or Amorphous Samples, Proc. *EUREM* **July 9-14**, *12*, 1379–1380.

(32) Tran, D. T.; Svensson, G.; Tai, C. W. SUePDF: A Program to Obtain Quantitative Pair Distribution Functions from Electron Diffraction Data. *J. Appl. Crystallogr* **2017**, *50* (Pt 1), 304–312.

(33) Shanmugam, J.; Borisenko, K. B.; Chou, Y.-J.; Kirkland, A. I., eRDF Analyser: An Interactive GUI for Electron Reduced Density Function Analysis. *SoftwareX* **2017**, *6*, 185–192.

(34) Shi, H.; Luo, M.; Wang, W. ePDF Tools, a Processing and Analysis Package of the Atomic Pair Distribution Function for Electron Diffraction. *Comput. Phys. Commun* **2019**, *238*, 295–301.

(35) Mitchell, D. R. G.; Petersen, T. C. RDFTools: A Software Tool for Quantifying Short-range Ordering in Amorphous Materials. *Microscopy Res & Technique* **2012**, *75* (2), 153–163. https://doi.org/10.1002/jemt.21038.

(36) Savitzky, B. H.; Zeltmann, S. E.; Hughes, L. A.; Brown, H. G.; Zhao, S.; Pelz, P. M.; Pekin, T. C.; Barnard, E. S.; Donohue, J.; Rangel DaCosta, L.; Kennedy, E.; Xie, Y.; Janish, M. T.; Schneider, M. M.; Herring, P.; Gopal, C.; Anapolsky, A.; Dhall, R.; Bustillo, K. C.; Ercius, P.; Scott, M. C.; Ciston, J.; Minor, A. M.; Ophus, C. py4DSTEM: A Software Package for Four-Dimensional Scanning Transmission Electron Microscopy Data Analysis. *Microsc. Microanal* **2021**, 1–32.

(37) White, C. E.; Provis, J. L.; Proffen, T.; Deventer, J. S. J. v. The Effects of Temperature on the Local Structure of Metakaolin-Based Geopolymer Binder: A Neutron Pair Distribution Function Investigation. *J. Am. Ceram. Soc* **2010**, *93* (10), 3486–3492.

(38) Chen, M. A Brief Overview of Bulk Metallic Glasses. *NPG Asia Materials* **2011**, *3* (9), 82–90.

(39) Wang, W. H.; Dong, C.; Shek, C. H. Bulk metallic glasses. *Mater. Sci. Eng. R: Rep* **2004**, *44* (2–3), 45–89.

(40) Takagi, T.; Ohkubo, T.; Hirotsu, Y.; Murty, B. S.; Hono, K.; Shindo, D. Local Structure of Amorphous $Zr_{70}Pd_{30}$ Alloy Studied by Electron Diffraction. *Appl. Phys. Lett* **2001**, *79* (4), 485–487.

(41) Hirata, A.; Guan, P.; Fujita, T.; Hirotsu, Y.; Inoue, A.; Yavari, A. R.; Sakurai, T.; Chen, M. Direct Observation of Local Atomic Order in a Metallic Glass. *Nat. Mater* **2011**, *10* (1), 28–33.

(42) Yuan, Y.; Kim, D. S.; Zhou, J.; Chang, D. J.; Zhu, F.; Nagaoka, Y.; Yang, Y.; Pham, M.; Osher, S. J.; Chen, O.; Ercius, P.; Schmid, A. K.; Miao, J. Three-Dimensional Atomic Packing in Amorphous Solids with Liquid-like Structure. *Nat Mater* **2021**.

(43) Sergueeva, A. V.; Mara, N. A.; Kuntz, J. D.; Branagan, D. J.; Mukherjee, A. K. Shear Band Formation and Ductility of Metallic Glasses. *Mater. Sci. Eng. A* **2004**, *383* (2), 219–223.

(44) Greer, A. L.; Cheng, Y. Q.; Ma, E. Shear Bands in Metallic Glasses. *Mater. Sci. Eng. R: Rep* **2013**, *74* (4), 71–132.

(45) Chen, Y. M.; Ohkubo, T.; Mukai, T.; Hono, K. Structure of Shear Bands in $Pd_{40}Ni_{40}P_{20}$ Bulk Metallic Glass. *J. Mater. Res* **2009**, *24* (1), 1–9.

(46) Mu, X.; Chen, L.; Mikut, R.; Hahn, H.; Kübel, C. Unveiling Local Atomic Bonding and Packing of Amorphous Nanophases via Independent Component Analysis Facilitated Pair Distribution Function. *Acta Mater* **2021**, 212.

(47) Mu, X.; Chellali, M. R.; Boltynjuk, E.; Gunderov, D.; Valiev, R. Z.; Hahn, H.; Kubel, C.; Ivanisenko, Y.; Velasco, L. Unveiling the Local Atomic Arrangements in the Shear Band Regions of Metallic Glass. *Adv. Mater* **2021**, *33* (12).

(48) Huang, P. Y.; Kurasch, S.; Srivastava, A.; Skakalova, V.; Kotakoski, J.; Krasheninnikov, A. V.; Hovden, R.; Mao, Q.; Meyer, J. C.; Smet, J.; Muller, D. A.; Kaiser, U. Direct Imaging of a Two-Dimensional Silica Glass on Graphene. *Nano Lett* **2012**, *12* (2), 1081–1086.

(49) Aarik, J. A.; A., K.; A.-A., U.; T., S. V. Infuence of Substrate Temperature on Atomic Layer Growth and Propertiesof HfO_2 Thin Flms. *Thin Solid Films* **1999**, 340 110-116.

(50) Dillon, A. C.; Ott, A. W.; Way, J. D.; George, S. M. Surface Chemistry of Al_2O_3 Deposition Using $Al(CH_3)_3$ and H_2O in a Binary Reaction Sequence. *Surf. Sci* **1995**, *322*, 230–242.

(51) Bassiri, R.; Borisenko, K. B.; Cockayne, D. J. H.; Hough, J.; MacLaren, I.; Rowan, S. Probing the Atomic Structure of Amorphous Ta_2O_5 Coatings. *Appl. Phys. Lett* **2011**, *98*, 031904.

(52) Willinger, E.; Massue, C.; Schlogl, R.; Willinger, M. G. Identifying Key Structural Features of IrO_x Water Splitting Catalysts. *J. Am. Chem. Soc* **2017**, *139* (34), 12093–12101.

(53) Schleder, G. R.; Azevedo, G. M.; Nogueira, I. C.; Rebelo, Q. H. F.; Bettini, J.; Fazzio, A.; Leite, E. R. Decreasing Nanocrystal Structural Disorder by Ligand Exchange: An Experimental and Theoretical Analysis. *J. Phys. Chem. Lett* **2019**, *10* (7), 1471–1476.

(54) Nakamura, R.; Toda, T.; Tsukui, S.; Tane, M.; Ishimaru, M.; Suzuki, T.; Nakajima, H. Diffusion of Oxygen in Amorphous Al_2O_3, Ta_2O_5, and Nb_2O_5. *J. Appl. Phys* **2014**, *116*, 033504.

(55) Borisenko, K. B.; Chen, Y.; Song, S. A.; Nguyen-Manh, D.; Cockayne, D. J. H. A Concerted Rational Crystallization/Amorphization Mechanism of $Ge_2Sb_2Te_5$. *J. Non-Cryst. Solids* **2009**, *355* (43–44), 2122–2126.

(56) Borisenko, K. B.; Chen, Y.; Song, S. A.; Cockayne, D. J. H. Nanoscale Phase Separation and Building Blocks of $Ge_2Sb_2Te_5N$ and $Ge_2Sb_2Te_5N_2$ Thin Films. *Chem. Mater* **2009**, *21* (21), 5244–5251.

(57) Hirata, A.; Ichitsubo, T.; Guan, P. F.; Fujita, T.; Chen, M. W. Distortion of Local Atomic Structures in Amorphous Ge-Sb-Te Phase Change Materials. *Phys. Rev. Lett* **2018**, *120* (20).

(58) Siwick, B. J.; Dwyer, J. R.; Jordan, R. E.; Miller, R. J. D. Femtosecond Electron Diffraction Studies of Strongly Driven Structural Phase Transitions. *Chem. Phys* **2004**, *299* (2–3), 285–305.

(59) Nakamura, R.; Ishimaru, M.; Yasuda, H.; Nakajima, H. Atomic rearrangements in amorphous Al_2O_3 under electron-beam irradiation. *J. Appl. Phys* **2013**, *113*, 064312.

(60) Sun, Z.; Zhou, J.; Ahuja, R. Unique Melting Behavior in Phase-Change Materials for Rewritable Data Storage. *Phys. Rev. Lett* **2007**, *98* (5), 055505.

(61) Akola, J.; Jones, R. O. Structural Phase Transitions on the Nanoscale: The Crucial Pattern in the Phase-Change materials $Ge_2Sb_2Te_5$ and GeTe. *Phys. Rev. B* **2007**, *76*, 235201.

(62) Hegedus, J.; Elliott, S. R. Microscopic Origin of the Fast Crystallization Ability of Ge-Sb-Te Phase-Change Memory Materials. *Nat. Mater* **2008**, *7* (5), 399–405.

(63) Farrow, C. L.; Ruan, C.-Y.; Billinge, S. J. L. Quantitative Nanoparticle Structures from Electron Crystallography Data. *Phys. Rev. B* **2010**, *81*, 134104.

(64) Luo, D.; Hui, D.; Wen, B.; Li, R.; Yang, J.; Shen, X.; Reid, A. H.; Weathersby, S.; Kozina, M. E.; Park, S.; Ren, Y.; Loeffler, T. D.; Sankaranarayanan, S. K. R. S.; Chan, M. K. Y.; Wang, X.; Tian, J.; Arslan, I.; Wang, X.; Rajh, T.; Wen, J. Ultrafast Formation of a Transient Two-Dimensional Diamondlike Structure in Twisted Bilayer Graphene. *Phys. Rev. B* **2020**, *102* (15).

(65) Gorelik, T. E.; Schmidt, M. U.; Kolb, U.; Billinge, S. J. Total-Scattering Pair-Distribution Function of Organic Material from Powder Electron Diffraction Data. *Microsc. Microanal* **2015**, *21* (2), 459–471.

(66) Mu, X.; Mazilkin, A.; Spray, C.; Colsmann, A.; Kübel, C. Mapping Structure and Morphology of Amorphous Organic Thin Films by 4D-STEM Pair Distribution Function Analysis. *Microscopy* **2019**, *68* (4), 301–309.

(67) Billinge, S. Atomic Pair Distribution Function: A Revolution in the Charactization of Nanostructured Pharmaceuticals. *Nanomed.* **2015**, *10* (16), 2473–2475.

(68) Chou, T. M.; Prayaoonthong, P.; Aitouchen, A.; Libera, M. Nanoscale Artifacts in RuO_4-Stained Poly(Styrene). *Polymer* **2002**, *43* (7), 2085–2088.

(69) González, M. A. Force fields and molecular dynamics simulations. *École thématique de la Société Française de la Neutronique* **2011**, *12*, 169–200.

(70) Riniker, S. Fixed-Charge Atomistic Force Fields for Molecular Dynamics Simulations in the Condensed Phase: An Overview. *J. Chem. Inf. Model* **2018**, *58* (3), 565–578.

(71) Komanduri, R.; Raff, L. M. A Review on the Molecular Dynamics Simulation of Machining the Atomic Scale. *Proc. Inst. Mech. Eng. C* **2001**, *215* (12), 1639.

(72) McGreevy, R. L.; Pusztai, L. Reverse Monte Carlo Simulation: A New Technique for the Determination of Disordered Structures. *Mol. Simul.* **1988**, *1* (6), 359–367.

(73) Soper, A. K. Empirical Potential Monte Carlo Simulation of Fluid Structure. *Chem. Phys.* **1996**, *202* (2–3), 295–306. https://doi.org/10.1016/0301-0104(95)00357-6.

(74) Gettler, R. C.; Koenig, H. D.; Young, M. J. Iterative Reverse Monte Carlo and Molecular Statics for Improved Atomic Structure Modeling: A Case Study of Zinc Oxide Grown by Atomic Layer Deposition. *Phys. Chem. Chem. Phys.* **2021**, *23* (46), 26417–26427. https://doi.org/10.1039/D1CP03742K.

(75) Opletal, G.; Petersen, T.; O'Malley, B.; Snook, I.; McCulloch, D. G.; Marks, N. A.; Yarovsky, I. Hybrid Approach for Generating Realistic Amorphous Carbon Structure Using Metropolis and Reverse Monte Carlo. *Mol. Simul.* **2002**, *28* (10–11), 927–938. https://doi.org/10.1080/0892702040000025584.

(76) Yang, Y.; Zhou, J.; Zhu, F.; Yuan, Y.; Chang, D. J.; Kim, D. S.; Pham, M.; Rana, A.; Tian, X.; Yao, Y.; Osher, S. J.; Schmid, A. K.; Hu, L.; Ercius, P.; Miao, J. Determining the Three-Dimensional Atomic Structure of an Amorphous Solid. *Nature* **2021**, *592* (7852), 60–64. https://doi.org/10.1038/s41586-021-03354-0.

(77) Opletal, G.; Petersen, T. C.; Russo, S. P. HRMC_2.1: Hybrid Reverse Monte Carlo Method with Silicon, Carbon, Germanium and Silicon Carbide Potentials. *Comput. Phys. Commun* **2014**, *185* (6), 1854–1855. https://doi.org/10.1016/j.cpc.2014.02.025.

(78) Groner, M. D.; Fabreguette, F. H.; Elam, J. W.; George, S. M. Low-Temperature Al_2O_3 Atomic Layer Deposition. *Chem. Mater.* **2004**, *16* (4), 639–645. https://doi.org/10.1021/cm0304546.

CHAPTER 2: METHODS

2.1 Introduction

Progress in materials science is heavily coupled to the advancement of methods, bound closely to their capabilities and their limitations. My work was motivated by the limitations of existing methods, driving my efforts to develop new techniques to extend the capabilities of our scientific community. To do so, I have necessarily employed existing methodologies. This chapter details the methods employed throughout my doctoral work: engineering and synthetic procedures for freestanding ultrathin materials, experimental and computational characterization techniques, and the Python-based approaches used in developing our modeling software. Through the methods described below, my doctoral work has contributed valuable strategies to further our understanding of an underexplored class of amorphous materials.

2.2 Construction of an atomic layer deposition reactor

Vapor-based deposition methods such as atomic layer deposition (ALD) offer a solution to key challenges in the synthesis of freestanding amorphous 2D materials without defects. The advantages of ALD include its self-limiting nature, meaning that no more than a monolayer of material will be deposited per cycle, which grants users a high degree of precision in controlling film thickness. A versatile range of precursors and temperatures may also be used to fabricate layered and multiple-composition materials. Earlier work in our lab revealed ALD to be a suitable technique to produce a freestanding material when cm-scale NaCl slabs were used as substrates.

A detailed investigation of the deposition mechanism on NaCl effect could not be performed with ex situ pretreatment; however, since transfer to the ALD reactor in air could

presumably affect plasma-induced changes in surface composition due to the high-energy nature of the plasma. Therefore, in situ plasma functionality was needed. Additionally, we sought to investigate the generalizability of this method to other compositions and the reaction mechanisms that control important synthesis–structure relationships. For each reaction type, different precursors and deposition temperatures are needed, necessitating an instrument that could accommodate an expanded range of precursors and temperatures. On the basis of these challenges, we determined the need for a custom reactor.

2.2.1 Reactor design

To synthesize freestanding amorphous thin films for characterization, I constructed a custom reactor for ALD (Figure 2.1). The reactor is primarily constructed with 304 and 316 steel to minimize undesirable precursor reactions with the interior walls. Connections between pieces include ¼ in. Swagelok tube fittings, ¼ in. VCR, NW40 O-ring, and 2.75” outer diameter conflat flange attachments. The temperature rating of the system is determined by the Viton O-rings, which have a maximum rating of 220 °C.

The system temperature is controlled by a 6-zone Omega PID CN616A controller. This controller allows users to individually set temperatures for each zone, allowing different sections of the reactor to be heated to separate temperatures—a feature that is useful for precursors that require different holding temperatures. Each zone is connected to a heating tape (HTS Amptek, Duo-Tape 120 V). The heating tape is switched on and off to maintain the target temperature, which is achieved by a solid-state relay that is attached to the heating tape and receives signals from the PID controller. Temperatures are monitored by the PID controller through K-type thermocouples, which are inserted between the reactor and the wrapped heating tape at each zone

of the reactor. To insulate the heated components on the system, these parts were wrapped with woven ceramic tape (Cotronics, Ultra Temp.) and an outer layer of aluminum foil.

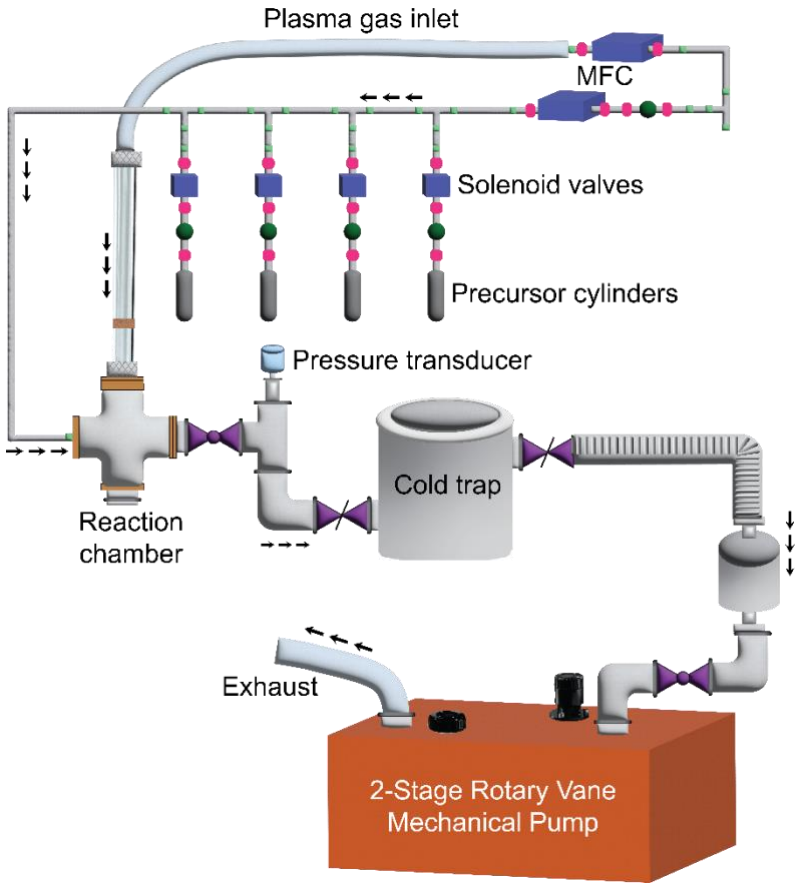


Figure 2.1. Schematic of our custom ALD reactor with an in situ plasma generator. Dark green circles indicate manual valves, pink circles indicate VCR connections, and lime green squares indicate Swagelok connections. Plasma is produced in the glass tubing directly above the reaction chamber. The heating and insulation elements have not been visualized for clarity.

The system pressure is monitored and controlled by several key features of the system. A DUO35 2-phase rotary vane vacuum pump (Pfeiffer Vacuum) was initially attached and used for the experiments in this work, which can achieve an ultimate base pressure of 2.25×10^{-3} Torr with the gas ballast closed. Recently, the pump has been replaced with an Adixen 2033 SD pump, which

can reach similar base pressures. On the opposite end of the stream, the carrier gas inlet is controlled by an MKS mass flow controller. This controller is computer controlled through an ethernet cable and is configured for N_2 gas flow. The system pressure is measured by a vacuum pressure transducer (MKS Instruments) located downstream of the reaction chamber and has a 10 mTorr maximum reading. The pressure readout is transmitted as a voltage, which is converted to a pressure reading through a custom LabVIEW program (Figure 2.2).

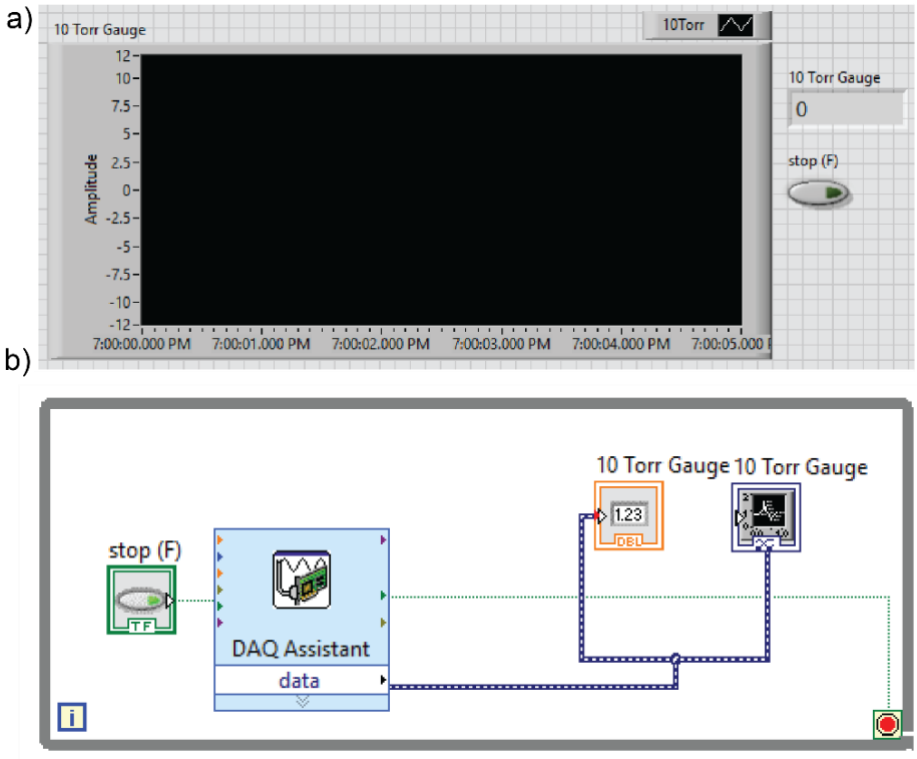


Figure 2.2. (a) Front and (b) back panels of the LabVIEW program to plot the pressure reading from the system pressure gauge. The gauge has a maximum reading of 10 mTorr.

The system can hold up to four precursors at a time, which are each attached to a manual valve and a computer-controlled solenoid pneumatic valve further downstream. This two-valve design allows for easy exchange of precursor cylinders in the system. One drawback of this design is the proximity of individual precursor inlets, which results in frequent material build-up and

occasional clogging of the joints immediately adjacent to the solenoid valves. Users should practice regular cleaning of the interior of these joints by wiping with a kimwipe (1x a month during periods of heavy use).

Downstream of these precursors lie the reaction chamber and direct plasma generator. The reaction chamber is accessed by the O-ring cap that faces the user. The samples should be inserted into the center of the reaction chamber, which lies directly downstream of the precursor inlet and below the plasma generator. Details of the plasma generator can be found in section 2.2.5.

A cold trap was later attached downstream of the reaction chamber to reduce the flow of excess precursor and reaction byproducts to the vacuum pump. Before deposition, the central Dewar of the cold trap should be filled with an isopropanol/dry ice slurry. The slurry was prepared by pouring approximately 1 L of isopropanol in the Dewar and slowly adding dry ice until the slurry reached 3/4th of the Dewar volume. After use, the cold trap should be isolated from the upstream and downstream components by closing the valves attached to either side of the trap. The trap may then be removed from the system by disconnecting one or more of the O-ring joints and be slowly brought up to pressure by gradually opening the valve adjacent to the disconnected joint. Once returned to ambient pressure, the dewar may be removed from the body of the cold trap and set on a nonflammable surface inside a chemical fume hood. Users should exercise caution during this step, particularly after extended use, because unreacted precursors on the exterior walls may ignite when exposed to air. Once removed, the dewar exterior walls may be quenched by air exposure or toluene.

2.2.2 Leak testing

To ensure that the system was properly sealed and under vacuum, leak testing was performed. The bleed-up testing method was selected for this task and involves the following steps.

First, the system was sealed and placed under vacuum until it reached base pressure. The ball valve immediately above the vacuum pump inlet was then closed to isolate the reactor system. The pressure was recorded, and the system was left for ten minutes, after which the pressure was recorded again. The ball valve was then reopened, and the system was allowed to return to base pressure, at which point the valve was closed again, and the process was repeated. This sequence was repeated for a total of 15 cycles. Over each repetition, a rise in pressure was recorded, which can be attributed to two possible factors: outgassing or a leak. Because any system that has been previously under ambient conditions will produce some amount of outgassing, repeating the pressure measurements is necessary to distinguish the cause. If the increase in pressure is mostly due to outgassing, this effect will diminish over repeated cycles such that the pressure increase will be much smaller after several cycles. If the pressure increase is due to a leak, the rise should be constant regardless of the number of cycles performed. The results of this leak test are shown in Figure 2.3. Because the rise in pressure decreases significantly over repeated cycles, the maximum possible leak rate of this system was determined to be < 0.1 mTorr.

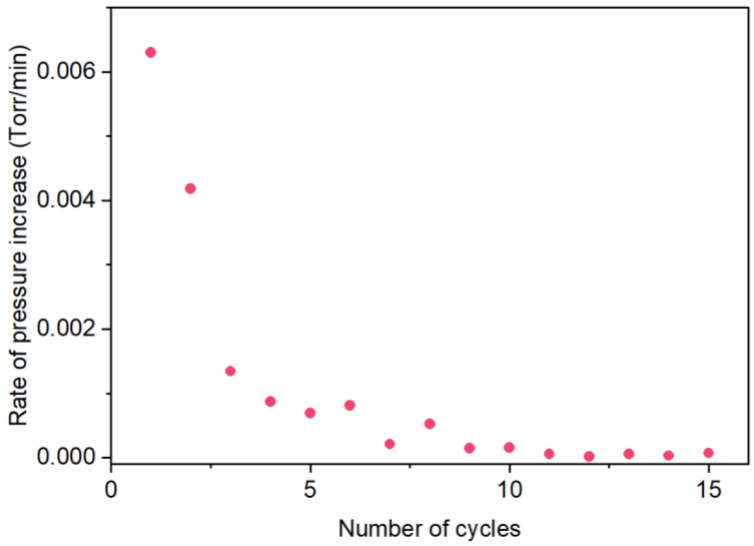


Figure 2.3. Leak testing of the ALD reactor under the bleed-up testing method. In each cycle after reaching base pressure, the system was isolated for 10 min before the pressure was recorded.

2.2.3 LabVIEW Program

ALD with the reactor is automated through a customized LabVIEW program. Much of the code for this program is drawn from Selvaraj et al., with some changes specific to our reactor.[1] This program communicates with the precursor solenoid pneumatic valves to open and close these valves at assigned intervals. This program allows the user to select standard ALD variables such as the number of cycles, wait periods before recipe execution, and the pulse and purge periods of each precursor. A Boolean indicator for each precursor indicates when a pneumatic valve is open. Displays for the total recipe time, time since the start of the recipe, and time remaining in the recipe are also included. The front and back panels of this program are shown in Figures 2.4.

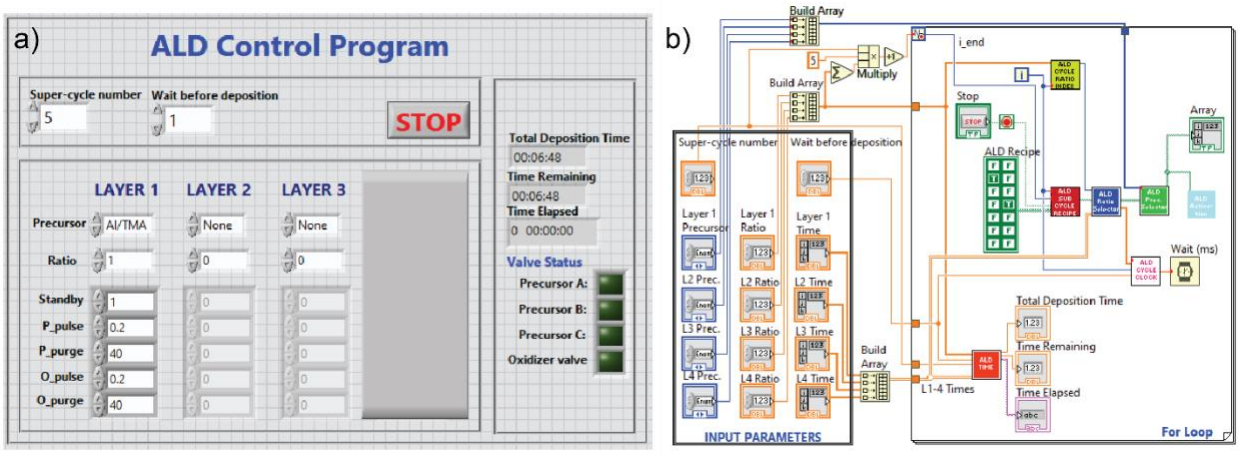


Figure 2.4. (a) Front panel and (b) back panel of the ALD LabVIEW program to control the pneumatic precursor valves for automated ALD.

When the ALD recipes are entered into the LabVIEW program, users should note a technical limitation of the system. The switch rate of the solid-state relays for the valves is limited to a minimum of 200 ms between switches, making this the minimum pulse time. While this time is longer than typical ALD pulse times, this limitation should not affect the ALD conditions of deposition. Purge times are unlikely to be affected by this switching rate since they are usually at least an order of magnitude longer than the minimum switch time.

2.2.4 Validation of ALD conditions

Instrument validation was performed to confirm ALD-type growth within the reactor. Al_2O_3 was selected as a model reaction with a typical growth rate of 1.1 Å/cycle, although reports have shown that rates may vary up to nearly 3 Å/cycle depending on the instrument used.[2] The films were deposited directly onto cleaned Si wafers with a thermal oxide using trimethylaluminum (TMA) and H_2O as precursors. The film thicknesses of all the samples were measured with a spectroscopic ellipsometer (J. A. Woollam V-VASE) at wavelengths between 500 and 900 nm. The measurements were fitted with a Cauchy model. First, cycles of only TMA

pulse/purges were repeated for 25 cycles on a cleaned Si wafer at 150 °C to confirm that atmospheric water was not entering the system. No growth was observed, which is consistent with the leak testing results. Next, the TMA pulse times were tested from 0.2–0.6 s in increments of 0.1 s over 50 cycles and with 0.3 s H_2O pulses. The growth rates were found to be saturated within the range tested, indicating that the saturation point existed below a pulse time of 0.2 s. Due to technical limitations, the solenoid valves possess a lower switching limit of 0.2 s. For this reason, a pulse duration of 0.2 s was adopted for all future depositions. Water, which has a higher vapor pressure than TMA at room temperature, was found to be similarly saturated at the minimum allowed pulse duration, and 0.2 s pulses were also selected. Purge times of 40 s was found to be sufficient to remove the excess precursor and prevent uncontrolled growth.

2.2.5 Capacitively coupled plasma generator

A capacitively coupled plasma system was constructed directly above the main reaction chamber. In this system, two electrodes were attached to a quartz tube: one grounded and the other connected to a commercial 13.56 MHz RF power supply (T&C Power Conversion, AG 0313) and an automatching network (T&C Power Conversion, AIT-600). When a voltage is applied with an RF signal, an electric field is produced between the two electrodes. The electric field accelerates free electrons produced by background radiation such that collisions with neutral atoms generate secondary free electrons. Once the field is sufficiently strong, an electron avalanche occurs, and the ionized gas reaches breakdown to become a plasma with a visible glow discharge. Therefore, stable plasma depends, among other factors, on a power source to create a strong electric field.

Initial attempts to ignite a plasma were unsuccessful because of severely mismatched impedances between the RF source and electrode load. Any mismatch causes the signal to be reflected back to the source, resulting in a dissipated RF and poor transfer. For efficient transfer of

RF power from source to load, the two impedances must be complex conjugates of each other; i.e., the two impedances must have resistances (real impedance) and reactances (imaginary impedance) that are equal in magnitude but opposite in sign. To achieve these values, matching networks between the RF generator and electrode are used to correct for small differences between the source and load impedances. However, early measurements revealed that the electrode impedances have a large reactive impedance with close to no resistance, lying outside of the tuning range of the matching network. A decreased load reactance was required to access this tuning range.

Rather than changing the setup of the electrodes themselves, as is typically required to change impedance, I utilized a strategy that allowed the electrode system to remain unchanged. This new approach was enabled by transmission line effects observed in high-frequency systems. Due to some amount of the incident signal being reflected at the load, a standing wave emerges in the transmission line from the sum of the incident and reflected waves. At λ/4 of this wave, the relationship between the impedance seen by the source (Z_{so}), load impedance (Z_L), and characteristic impedance of the transmission line (Z_0) is expressed as:

$$Z_{so}\left(\frac{\lambda}{4}\right) = \frac{Z_0^2}{Z_L} \quad \text{(2-1)}.$$

The effect is that the load impedance, as seen by the source, is inversely proportional to Z_L. As such, the large magnitude of load reactance could be transformed into a small magnitude by terminating the transmission line at λ/4. For a 13.56 MHz frequency, λ/4 is 5.527 m. An RG214 coaxial cable of 3.7 m was inserted between the matching network and electrode connection, resulting in a transmission line of approximately 4 m. The resulting decrease in the observed load reactance allowed the impedance to reach a value within the tuning range of the matching network that then minimized the remaining impedance mismatches. The success of the approach was

immediately visible with the ignition and glow discharge of a stable plasma between the two electrodes.

2.3 Synthesis methods

In my doctoral work, I have developed a strategy to fabricate freestanding large-area, ultrathin amorphous materials with atomic layer deposition. All substrate plasma treatments and alumina ALD were performed in our custom ALD reactor. The samples were transferred to a Savannah G2 commercial ALD system for titania deposition.

2.3.1 Preparation of ALD materials on NaCl

To synthesize transferable ALD materials at the cm scale, I prepared single-crystal substrates of NaCl. These crystals, which were purchased commercially as 2.5 cm^3 cubes, were mechanically cleaved along the (100) plane because it allows even cleavage to produce an atomically flat surface. To cleave, a razor blade should be placed on top of the crystal, perpendicular to the surface. If the razor blade is correctly positioned, light tapping on the blade by a hammer will slice the crystal along the lattice plane, creating an even surface. The substrates were cleaved immediately before loading into the custom ALD reactor to minimize contamination and degradation of the deposition surface.

After the reaction chamber was pumped to base pressure, the substrates were treated with direct plasma exposure. The capacitively coupled plasma generator is located directly above the reaction chamber in our in-house system, in contrast to remote plasma sources, which are often employed in plasma-enhanced ALD. In direct plasma treatment, the plasma ions are able to directly strike the surface of the substrate and result in harsher treatment conditions. While I did not test remote plasma sources for this work, appropriately low plasma wattages did not significantly alter the surface according to atomic force microscopy (AFM) measurements (see chapter 3). For the

substrate treatments, I used five minutes of N_2 plasma at 100 W for early experiments or 25 W for later experiments. While O_2 plasma treatments provided similar results (as discussed in chapter 3), N_2 plasma was preferable for safety reasons. This plasma step was immediately followed by ALD of either alumina or titania. The ALD recipe implementation was fully automated through LabVIEW, which requires only the initial configuration from the user.

2.3.2 Transfer of ALD materials

Substrate transfer for the ALD materials was performed with the aid of a polymethyl methacrylate (PMMA) sacrificial coating. This coating was applied to the ALD material via spin-coating. Using a glass pipette, I added one drop of our solution of PMMA in anisole to the top surface of the material. Spin coating the PMMA at 2500 rpm for 1 min produced a ~70 nm-thick coating, which was subsequently cured in an oven at 140 °C. The curing step is essential for the next step, which involves placing the material in a water bath to dissolve the NaCl substrate. Due to the hydrophobic nature of PMMA, a fully cured coating will float at the air–water interface. If the PMMA is not fully cured, the coating may be washed away, and the material will not float. In this latter case, it is no longer possible to retrieve the ALD material. Thus, to ensure that the coating was fully cured, I used a curing time of 40 min, which is longer than the recommended times recommended by the manufacturer.

After preparing the PMMA coating, the following step is to transfer the material from NaCl to a substrate of choice. For my materials, I used a Si wafer cleaned with electronic grade acetone and isopropanol. Holding the wafer with tweezers, the material can be scooped out of the water bath, resulting in the material being suspended over a pool of water on the wafer. To remove dissolved Na^+ and Cl^-, I used a kimwipe to absorb the water by touching a corner of the wipe to the water, carefully avoiding contact with the film. The underside of the film was then rinsed by

pipetting ~0.5 mL of DI water beneath the film. This process was repeated ten times to remove residual contamination.

An important detail during the transfer step is choosing the appropriate tools. When using stainless steel tweezers to place the NaCl in the water bath and remove the materials, I observed significant contamination under optical and electron microscopes. This residue was not observed upon switching to plastic and Ti tweezers, suggesting that even cleaned steel tweezers are prone to flaking and leaving residue on the material. For this reason, I have exclusively used Ti tweezers to handle the materials in this work.

NaCl was fully removed after 30 min, and the remaining PMMA-alumina material was picked up with a cleaned Si wafer from below so that the PMMA coating remained on top. The material was rinsed with DI water and dried under ambient conditions. The PMMA was removed by soaking the sample in an acetone (Fisher Chemical, electronic grade) bath for 16 hrs. The final product was rinsed with electronic grade acetone and isopropanol prior to characterization.

2.4 Transmission Electron Microscopy

In my doctoral work, I have developed a characterization method that relies on TEM-based scattering and have thus used TEM extensively to examine my materials. These techniques have provided structural, morphological, and chemical insights into my materials. All TEM and most scanning transmission electron microscopy (STEM) data in this work were collected on a Thermo Fisher F200X Talos instrument at 200 keV. Because my doctoral work focuses on the characterization of amorphous materials, which lack lattice planes, I used a single (α) tilt holder for all samples. While a complete review of the theory behind TEM and its workings is outside the scope of this thesis, I refer the reader to Williams & Carter.[4] For a resource on analyzing and interpreting scattering data, I refer the reader to Egami & Billinge.[5]

2.4.1 Sample preparation

The samples were prepared for TEM analysis with different methods according to their morphology. To prepare samples such as extremely air-sensitive samples like Y_2C and Y_2CF_2, the material was ground to a fine powder in an agate mortar and pestle in an Ar-filled glovebox. This powder was transferred to a scintillation vial and then transferred again to another vial. This repeated transfer leaves a small amount (~1 mg) of fine particles attached to the walls of the vial, which is desirable for preventing excess material from being present on the TEM sample grid. One mL of toluene (Sigma–Aldrich, anhydrous) was added to the scintillation vial with a syringe. After inverting several times to mix the suspension, the solution was set aside for approximately one minute to allow larger particles to settle. Using a micropipette, 3 μL of this suspension was drop-cast onto the top surface of a 300 mesh Cu TEM grid with a lacey carbon support (the blue side of the grid, in contrast to the copper-colored bottom, which does not have the lacey carbon). The grid was dried under vacuum in the glovebox evacuation chamber for approximately one hour and then moved to a grid holder. The samples were transferred to the TEM under Ar in low-density polyethylene bags to mitigate oxidation. These bags were cut open immediately before the samples were loaded into the instrument.

Thin film samples were not air sensitive and were prepared under ambient conditions after ALD on NaCl. The materials were removed from NaCl and transferred to a Si wafer as described in section 2.3.3. During the last rinse of the material, a TEM grid was inserted into the pool of clean DI water to sit beneath the film. By removing the water, this process traps the grid between the wafer and the film. The remaining work-up of the sample was conducted as usual, yielding a TEM grid with a layer of ALD material.

2.4.2 Electron scattering

Electron total scattering can provide structural information on nanoscale regions of a material due to the small diameter of an electron beam. This advantage remains true for amorphous materials, which lack Bragg scattering spots or disks but still yield distinct diffuse scattering patterns. To collect these patterns, I first operate the TEM in imaging mode to identify a suitable sample region for characterization. For an amorphous thin ALD material, ideal regions are uniform without obvious contamination from debris or undissolved polymer. For particles, the region should be thin enough for the beam to transmit through the sample and ideally uniform in structure and composition. In both cases, I chose regions away from the lacey carbon support membrane to avoid contributions to the scattering pattern from the carbon. Because the materials that I characterized were amorphous, considerations of crystalline domain sizes and tilting to find zone axes were not necessary. Once I had identified a region to characterize, I then inserted a 10 mm or 40 mm selected area aperture, the smallest two available on UNC's Talos TEM. The aperture was centered on the beam before switching into diffraction mode.

When converting scattering patterns to pair distribution functions (PDFs), the scattering intensity at high scattering angles (q) is critical to achieve adequate spatial resolution. To acquire this q-range, I used two strategies: 1) short camera lengths and 2) long acquisition times. The camera length is the distance between the sample and the back focal plane where the diffraction pattern is formed, where the camera is placed to record the projection. Shorter distances allow higher scattering angles to fall on the detector. In my experiments, I used a short camera length of 260 mm for diffraction patterns intended for PDF analysis and otherwise used a camera length of 660 mm. Shorter camera lengths for PDFs may be used, but a tradeoff occurs between improved resolution of short distances in real space (from high-angle scattering) and blurring important

features at long distances in real space (from poorly resolved low-angle scattering). The second strategy of a longer acquisition time allows for greater intensities to be recorded, which is most valuable at high scattering angles where intensities are greatly diminished. When selecting an acquisition time, care must be taken to avoid burning the CCD camera from prolonged exposure to high intensities. For the ALD samples, I began with ms-scale times and gradually attempted longer acquisition times, often using 2–4 s for optimized datasets. For particle samples that are thicker than a few nm, I used < 1 s acquisition times. By using these strategies, I reliably acquired scattering data intensities that extended to ranges above 10 $Å^{-1}$.

2.4.3 Imaging

Almost all images in my doctoral work were collected in TEM mode as bright field images. To obtain these images, I inserted a 40–50 mm objective aperture for ultrathin film samples and a 70 mm objective aperture for particulate samples. In cases where dark field images were necessary, I acquired high-annular dark field (HAADF) images in scanning TEM (STEM) mode. In this case, no objective aperture was used.

2.4.4 Pair distribution function analysis

Diffraction patterns acquired via TEM were converted to PDFs using the RDFTools package for Gatan's DigitalMicrograph software (GMS 3).[6] All patterns were stored in the .mrc file format. Prior to analysis, the pixel sizes were calibrated in the DiffTools package with a polycrystalline Au-sputtered sample.[7]

Once imported into DigitalMicrograph, the first step is to obtain the radial intensity profile I(q) from the scattering pattern. RDFTools includes functions to apply pixel size calibrations and set a center on the pattern. The package then uses this center to perform a radial integration and produce the intensity profile. While line integration is also an option, I found that full radial

integration produced profiles with decreased noise. To obtain a PDF, this intensity profile must be converted to real space through a Fourier transform. The theory and details of this conversion to the PDF and its related forms are described in chapter one. RDFTools produces the reduced PDF, G(r):

$$G(r)=4\pi r\rho_0(g(r)-1) \quad (2\text{-}1).$$

The script does so by fitting a structure factor to the reduced interference function φ(q), which is calculated from the difference between the ideal and experimental scattering intensities. The function takes the following form:

$$\varphi(q) = \frac{I(q)+ \alpha - N\langle f(q)\rangle^2}{N\langle f^2(q)\rangle} \quad (2\text{-}3),$$

where N is the number of probed atoms and α is a constant that corrects for background errors in the intensity profile. Here, the user is responsible for fitting the structure factor by adjusting N and an empirical correction factor α. Several envelope functions are also available to dampen increased noise at high scattering angles. For this work, I used the 4-term Blackman–Harris envelope function for all of my PDF analyses.

2.5 Core Pythonic concepts

This section explores three core Pythonic concepts essential to our HRMC modeling package, pyHRMC: object-oriented programming for structured code organization, parallelization for accelerated computation, and interfacing with the Large-scale Atomic/Molecular Massively Parallel Simulator (LAMMPS) molecular dynamics package to integrate fast energy calculations into our program.

2.5.1 Classes and object-oriented programming

Whenever a large volume of code is assembled for a computational task, the organization of the code is always an important consideration. Not only does well-organized code aid readers

in interpreting the role of each line, but cost efficiencies can also be obtained from reducing redundancy. To section code into intuitive and useful blocks, Python, like many other programming languages, supports a programming paradigm called object-oriented programming. This type of organization operates around objects, which contain data and methods used to manipulate and analyze the data. Objects are created as an instance of a class, which is a set of functions that can be accessed once the class has been instantiated with data. Object-oriented programming is useful because all of the relevant data and functions can be manipulated and stored as a single modular unit, which can also interact with other objects and external functions. In fact, this approach is so effective at organizing code that using this strategy has become standard practice in building Python packages. PyHRMC has also been written in an object-oriented format, using classes to group code according to their role, such as calculating energy, structural properties, and scattering cross sections.

Another advantage of using classes is a property called inheritance. In Python, classes can be built off preexisting classes to add or modify methods. The derived class is referred to as the child class, whereas the original class is called the parent class. This feature allows programmers to avoid unnecessarily replicating code whenever minor changes are needed to another class, including those from other packages. Instead, these classes in these preprogrammed packages may be used as parent classes, and the child class may include the necessary changes to suit the target project's needs. The pyHRMC code has benefited greatly from this property of object-oriented programming by using open-source classes from established packages for materials science, pymatgen and matminer.[12,13]

2.5.2 Parallelization

Computational speed matters greatly for the throughput of complex calculations, which still face significant barriers in modeling large systems. While Python has the advantages of good user readability and convenient built-in functions, a significant drawback of the language is its slower execution speed relative to languages such as Fortran, Julia, or C/C++.[14,15] As a result, programs written in Python typically take more time to execute, which can cause a snowballing effect when code is repeated millions of times and cause drastically longer runtimes. Several approaches may be taken to mitigate this issue, one of which is to simply employ faster languages wherever possible in the code. This approach is taken in pyHRMC, which uses the NumPy package, which is largely written in C, to manage the positions of structure atoms. Another strategy is parallelization, which runs sections of the code in parallel (i.e., simultaneously). As I discuss in this section, pyHRMC also incorporates this strategy through a user-adjusted parallel architecture for key rate-limiting steps in the algorithm.

Parallelization in pyHRMC is achieved with the multiprocessing package. This package is built into Python 3 and therefore does not require additional installation. This package allows the system to use multiple processors to run tasks, in contrast to the multithreading package, which uses multiple threads on a single processor. Multithreading is fast to set up and requires fewer resources. However, the key consequence of their difference in architecture is that multiprocessing is performed in parallel and multithreading is performed concurrently. Concurrency is not the same as parallelism; due to Python's global interpreter lock, separate threads cannot access the same data simultaneously and, instead, access it in sequence. This feature means that when requests for the same data tend to overlap between threads, the speedups from multithreading are limited. As a result, multithreading is preferable to tasks where the input/output is rate limiting, whereas

multiprocessing is better suited for tasks that are rate limited by intensive computations. Because the majority of the execution time in pyHRMC is spent computationally rather than handling inputs/outputs, multiprocessing was selected for the program.

Multiprocessing offers straightforward methods that use a designated block of code as an argument (i.e., input) to be parallelized. These code blocks must be organized as a function so that each processor returns the output of the function as a variable. These variables can be collected in aggregate back on a single processor for subsequent use. In pyHRMC, generating "good" candidate atom perturbations is the rate-limiting step. Because of the stochastic nature of the generated candidates, the acceptance rate of these structures decreases greatly as a calculation progresses. This issue of low acceptance rates has led other programs to seek methods for improving the rate at which new Monte Carlo steps are accepted, including the adoption of machine-learned models to guide new steps.[16] PyHRMC handles this issue by generating a pool of candidates for each step, from which the algorithm accepts all moves that meet the constraint requirements.

For this task, pyHRMC uses the *starmap()* multiprocessing function. This function is able to take multiple iterables (e.g., lists, tuples, etc.) to use as arguments for the parallelized function. The starmap() function then returns an iterable variable that contains the result from each processor. In pyHRMC, the parallelized code is collected into the *make_candidate_structure()* function (Figure 2.5). The function generates a new candidate structure, checks the validity of this candidate against preset physical constraints, and if it passes these tests, it is checked against experimental and potential energy constraints. If successful, the function returns the candidate structure.

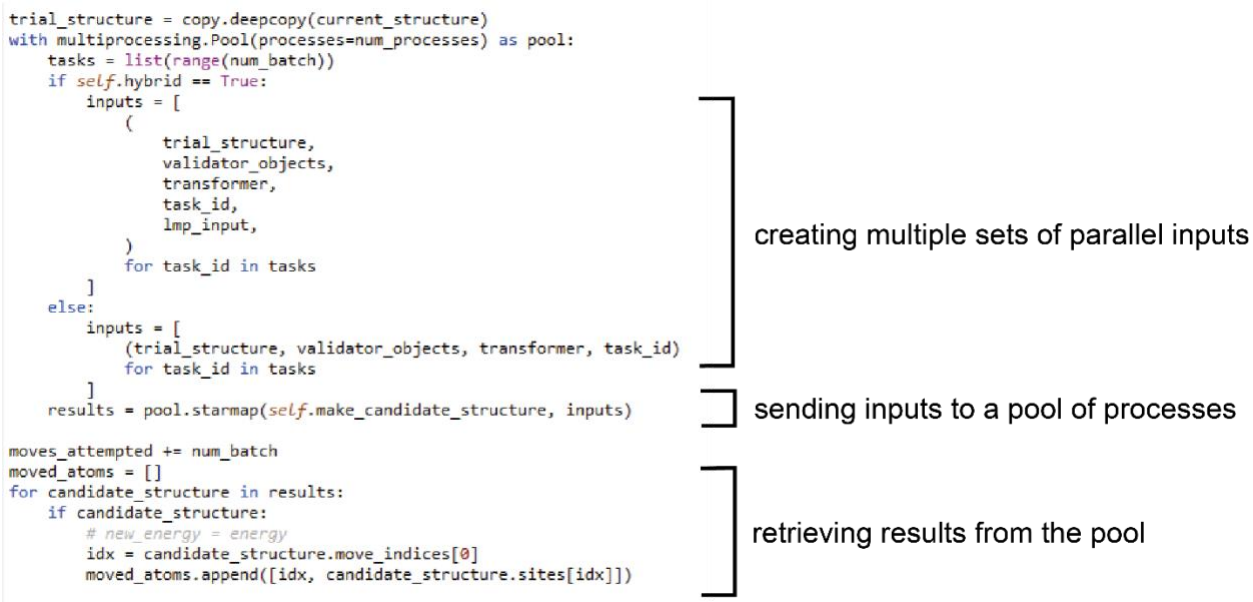


Figure 2.5. Code block for parallelizing the process of generating and checking individual steps. Here, the multiprocessing.Pool.starmap() method is used to parallelize the make_candidate_structure() function.

2.5.3 LAMMPS interfacing in Python

The potential energy of a structure plays an important role in HRMC to constrain unrealistic atomic configurations that might otherwise match the experimental ePDF. A key feature of HRMC is that the energy is computed every step alongside the ePDF fit. Thus, energy calculations must be performed quickly to maintain reasonable throughput. This "need for speed" has motivated the decision to use a molecular dynamics (MD) framework in our HRMC software, which circumvents the computationally expensive quantum mechanical calculations of density functional theory and related methods. For this task, we use the Large-scale Atomic/Molecular Massively Parallel Simulator (LAMMPS) software package because of its mature documentation and widespread use.[17] Implementing LAMMPS also allows any potential that is compatible with LAMMPS to also

work with pyHRMC, instantly accessing a wide library of potentials that may be employed for HRMC.

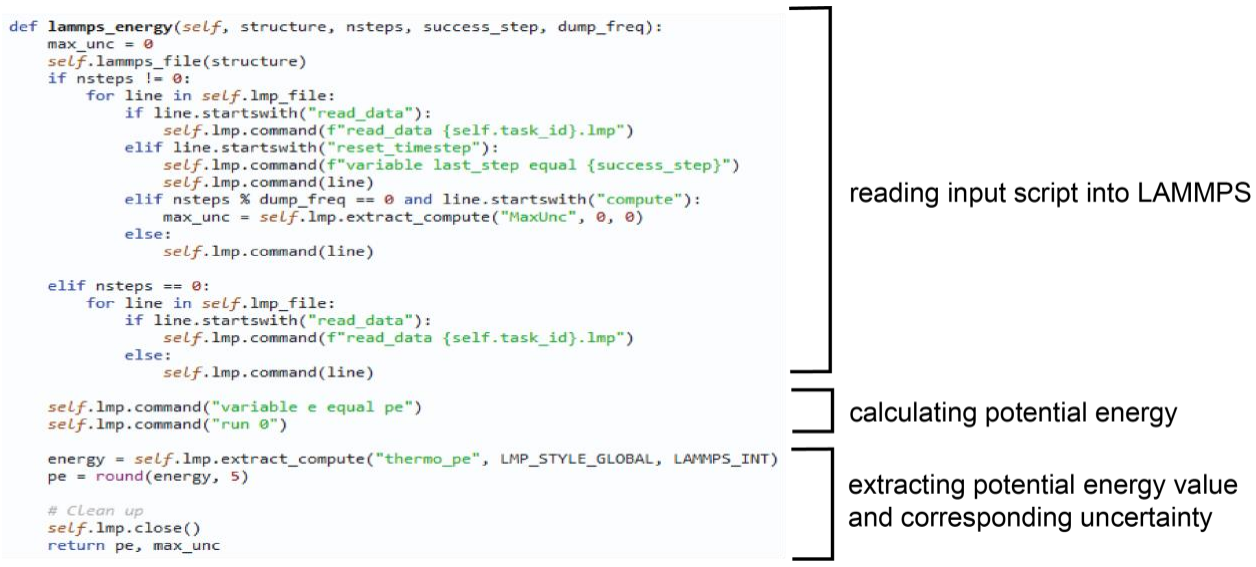


Figure 2.6. Code block responsible for interfacing with LAMMPS. A prewritten input script is read into the LAMMPS instance line by line and ends by extracting the computed potential energy (and maximum Gaussian uncertainty, if applicable).

To obtain potential energy values, pyHRMC interfaces with LAMMPS through the lammps Python module. This module allows a Python script to supply strings as line-by-line commands into LAMMPS to run an MD simulation (Figure 2.6). By using a command to run zero steps of MD, LAMMPS initializes and calculates the potential energy of the current structure without performing any actual molecular dynamics. Thus, this process is used exclusively for calculating energy and does not move atoms in any way. If a machine-learned FLARE potential is used, the maximum Gaussian uncertainty may also be returned to provide the user with an understanding of how well the potential's training data reflects the local configurations in the structure.

However, this strategy of interfacing with LAMMPS faces a minor drawback when parallelizing through pyHRMC. The default LAMMPS build is parallelized through OpenMP, whereas pyHRMC uses multiprocessing. Because the LAMMPS build must be compatible with Python parallelization, LAMMPS must be installed on the user's device as a serial executable. This allows pyHRMC to call multiple instances of LAMMPS in its parallel structure without conflicting resource allocation. Although this requirement will likely call for a new LAMMPS build when first installing the software, the setup should be a one-time process and is described thoroughly in the LAMMPS documentation.[18]

REFERENCES

(1) Selvaraj, S. K.; Takoudis, C. G. Scalable Control Program for Multiprecursor Flow-Type Atomic Layer Deposition System. *J. Vac. Sci. Technol. A: Vac. Surf. Films* **2015**, *33* (1), 013201. https://doi.org/10.1116/1.4893774.

(2) Sønsteby, H. H.; Yanguas-Gil, A.; Elam, J. W. Consistency and Reproducibility in Atomic Layer Deposition. *J. Vac. Sci. Technol. A: Vac. Surf. Films* **2020**, *38* (2), 020804. https://doi.org/10.1116/1.5140603.

(3) Abendroth, B.; Moebus, T.; Rentrop, S.; Strohmeyer, R.; Vinnichenko, M.; Weling, T.; Stöcker, H.; Meyer, D. C. Atomic Layer Deposition of TiO_2 from Tetrakis(Dimethylamino)Titanium and H_2O. *Thin Solid Films* **2013**, *545*, 176–182. https://doi.org/10.1016/j.tsf.2013.07.076.

(4) Williams, D. B.; Carter, C. B. *Transmission Electron Microscopy*; Springer US: Boston, MA, 2009. https://doi.org/10.1007/978-0-387-76501-3.

(5) Egami, T. *Underneath the Bragg Peaks: Structural Analysis of Complex Materials*, 2nd ed.; Pergamon Materials Ser; Volume 16; Elsevier Science & Technology: London, 2012.

(6) Mitchell, D. R. G.; Petersen, T. C. RDFTools: A Software Tool for Quantifying Short-range Ordering in Amorphous Materials. *Microsc Res. Tech.* **2012**, *75* (2), 153–163. https://doi.org/10.1002/jemt.21038.

(7) Mitchell, D. R. G. DiffTools: Electron Diffraction Software Tools for DigitalMicrograph™. *Microsc Res. Tech* **2008**, *71* (8), 588–593. https://doi.org/10.1002/jemt.20591.

(8) Kresse, G.; Furthmüller, J. Efficient Iterative Schemes for *Ab Initio* Total-Energy Calculations Using a Plane-Wave Basis Set. *Phys. Rev. B* **1996**, *54* (16), 11169–11186. https://doi.org/10.1103/PhysRevB.54.11169.

(9) Perdew, J. P.; Burke, K.; Ernzerhof, M. Generalized Gradient Approximation Made Simple. *Phys. Rev. Lett.* **1996**, *77* (18), 3865–3868. https://doi.org/10.1103/PhysRevLett.77.3865.

(10) Moellmann, J.; Grimme, S. DFT-D3 Study of Some Molecular Crystals. *J. Phys. Chem. C* **2014**, *118* (14), 7615–7621. https://doi.org/10.1021/jp501237c.

(11) Grimme, S.; Ehrlich, S.; Goerigk, L. Effect of the Damping Function in Dispersion Corrected Density Functional Theory. *J. Comput. Chem.* **2011**, *32* (7), 1456–1465. https://doi.org/10.1002/jcc.21759.

(12) Ong, S. P.; Richards, W. D.; Jain, A.; Hautier, G.; Kocher, M.; Cholia, S.; Gunter, D.; Chevrier, V. L.; Persson, K. A.; Ceder, G. Python Materials Genomics (Pymatgen): A Robust, Open-Source Python Library for Materials Analysis. C*omput. Mater. Sci.* **2013**, *68*, 314–319. https://doi.org/10.1016/j.commatsci.2012.10.028.

(13) Ward, L.; Dunn, A.; Faghaninia, A.; Zimmermann, N. E. R.; Bajaj, S.; Wang, Q.; Montoya, J.; Chen, J.; Bystrom, K.; Dylla, M.; Chard, K.; Asta, M.; Persson, K. A.; Snyder, G. J.; Foster, I.; Jain, A. Matminer: An Open Source Toolkit for Materials Data Mining. C*omput. Mater. Sci.* **2018**, *152*, 60–69. https://doi.org/10.1016/j.commatsci.2018.05.018.

(14) Jeffrey M. Perkel. Julia: Come for the Syntax, Stay for the Speed. *Nature* **2019**, pp 141–142.

(15) Arboleda, Francisco Javier Moreno, Mateo Rincón Arias, and Jesús Antonio Hernández Riveros. Performance of Parallelism in Python and C++. *IAENG Int. J. Comput. Sci.* **2023**, *50* (2), 1–13.

(16) Aoun, B. Fullrmc, a Rigid Body Reverse Monte Carlo Modeling Package Enabled with Machine Learning and Artificial Intelligence. *J. Comput. Chem.* **2016**, *37* (12), 1102–1111. https://doi.org/10.1002/jcc.24304.

(17) Thompson, A. P.; Aktulga, H. M.; Berger, R.; Bolintineanu, D. S.; Brown, W. M.; Crozier, P. S.; In 'T Veld, P. J.; Kohlmeyer, A.; Moore, S. G.; Nguyen, T. D.; Shan, R.; Stevens, M. J.; Tranchida, J.; Trott, C.; Plimpton, S. J. LAMMPS - a Flexible Simulation Tool for Particle-Based Materials Modeling at the Atomic, Meso, and Continuum Scales. *Comput. Phys. Commun.* **2022**, *271*, 108171. https://doi.org/10.1016/j.cpc.2021.108171.

(18) Plimpton, S. J.; Kohlmeyer, A.; Thompson, A. P.; Moore, S. G.; Berger, R. LAMMPS: Large-Scale Atomic/Molecular Massively Parallel Simulator, 2023. https://doi.org/10.5281/ZENODO.3726416.

CHAPTER 3: FREESTANDING 2D GLASSES BY ATOMIC LAYER DEPOSITION

3.1 Introduction

Amorphous ultrathin materials are an increasingly important class of materials in nanoscale devices and technologies because of their distinct properties compared to bulk or crystalline materials. For example, the high optical transmission of some 2D materials lends themselves to optoelectronic devices[1–3] or protective pellicles in photolithography[4–7]. Researchers have also found utility in the extremely high permeation rates that stem from the large free volumes and short percolation pathways of 2D glasses, resulting in applications for energy storage[8–11] and water purification membranes[12–15]. Compared to bulk analogues, two-dimensional materials also possess high flexibility and mechanical durability[16], which are essential characteristics for flexible electronics[17–19] and thin film solar cells[20–22]. To fabricate 2D materials, chemical (CVD) and physical vapor deposition have gained popularity as synthetic methods. A closely related technique is atomic layer deposition (ALD), which has been widely adopted in thin film fabrication because of its ability to produce highly conformal coatings while offering a high degree of control over composition, thickness, and in some cases, crystallinity. Despite these advantages of ALD, there is currently no process for producing a freestanding amorphous 2D material with cm-scale dimensions from an ALD growth process. Given the valuable physical properties of 2D glasses, designing these materials with the precision offered by ALD and large lateral dimensions of other techniques would be useful. With this synthetic control, interesting materials could be realized in freestanding large-area, ultrathin materials, such as mixed-metal compositions and controlled heterostructures and interfaces.

The challenge of fabricating freestanding large-area materials with ALD lies in designing a substrate that supports uniform growth while also gently released from the material. Generally, ALD is performed on a reactive and homogenous substrate that forms covalent bonds with precursors. When designing an ALD substrate that is suitable for processing into freestanding materials, three key challenges emerge. First, ALD requires that the precursor form bonds with the substrate, but the presence of these bonds makes it difficult to later remove the substrate. Methods to transfer 2D materials exist but have largely been applied to materials with weaker sample-substrate interactions[23,24] or employ harsh etching steps that may damage the target material[25–27]. Second, continuous ALD films require a high density of nucleation sites, but each of these points is typically a location where bonds form to the substrate. Third, ALD chemistries require a range of growth temperatures, often with higher temperatures yielding higher purity,[28,29] but substrates with high thermal stability are typically difficult to remove, e.g. by dissolution.[30] While previous reports have demonstrated the fabrication of up to mm-scale freestanding ALD materials from polymer substrates, the low thermal stability of such substrates prevents their application to high-temperature syntheses.[31–33] Collectively, these conflicts make freestanding ALD materials a difficult synthetic target.

Substrate design is necessary to overcome the issues associated with removable ALD materials. Recently, NaCl has been demonstrated as a sacrificial substrate for growing MoS_2 and dewetted Au nanoparticles via CVD, as well as 2D metal oxides in solution-based synthesis.[34,35] After film growth, the underlying NaCl is removed by dissolution in a water bath and can be transferred to arbitrary substrates. When performed with these materials that possess weak sample-substrate interactions, substrate removal results in the clean transfer of the fabricated materials.[34] NaCl is promising as a general ALD sacrificial substrate because it has good thermal stability but

can easily dissolve in water. However, NaCl substrates are typically cleaved along the (100) lattice plane, which produces an atomically flat surface that lacks reactive sites to promote nucleation. These reactive sites for ALD are $-OH^-$ surface species, yet NaCl has a surface $-OH^-$ density of 0.07% at ambient pressure and presumably a lower density under ALD vacuum conditions.[36,37] This low value is indicative of the chemical inertness that leads to limited dissociation of H_2O at these flat surfaces. Therefore, if the NaCl surface can be activated for ALD growth, the material could be used as a straightforward ALD substrate that addresses the three challenges listed above.

To this end, we introduce a method to synthesize materials that are freestanding, amorphous, and centimeter-scale despite their strong surface interactions with substrates. We overcome the issue of contrasting requirements for deposition and transfer steps by exploiting a heterogeneous NaCl substrate that possesses a mixture of sites for weaker, physisorbing sites and covalent, chemisorbing sites. To introduce chemisorbing sites to a pristine NaCl surface, we exposed the surface to N_2 plasma. This plasma replaces Cl^- with bare electrons (F-centers) that subsequently react with H_2O to yield surface hydroxyl groups. The highly reducing nature of F-centers favors a dissociation reaction with atmospheric H_2O to form hydroxyls that fill the F-center sites. These reactive sites behave as nucleating sites to initiate ALD growth yet, depending on their surface density, result in a material that is only sparsely anchored to the substrate (Figure 3.1a). We propose a model for ALD growth and substrate removal in which the heterogeneous surface structure of the substrate can create a sufficient density of nucleation sites for coalesced growth while also preventing epitaxial growth. Because this heterogeneous structure allows the ALD materials to chemisorb to NaCl, the substrate can be removed under mild conditions (Figure 3.1b). This strategy yields high-quality ultrathin films that can be freestanding and large area due to the gentle removal of a heterogeneous growth substrate.

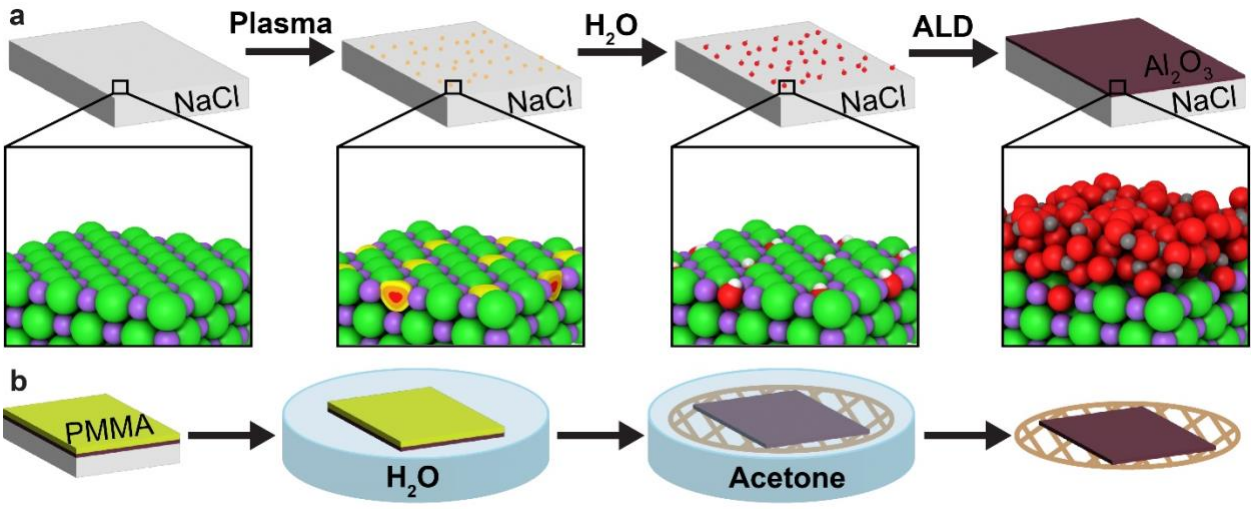


Figure 3.1. Scheme of the film fabrication and transfer process to yield a uniform, amorphous material that is freestanding. (a) Plasma irradiation of an atomically flat NaCl surface produces F-centers, which are replaced by surface embedded hydroxyls upon the reaction of these F-centers with H_2O. This activated substrate yields coalesced growth by ALD. (b) Transfer of ALD materials is performed with a PMMA support scaffold and the NaCl substrate is removed by dissolution in H_2O. Following transfer to an arbitrary substrate, the PMMA scaffold is removed by an acetone bath.

3.2 Results and discussion

3.2.1 Film-type growth on NaCl substrates with plasma pretreatment

Plasma irradiation and ALD of alumina were performed in a custom ALD reactor with a direct capacitively coupled N_2 plasma source. Alumina deposition was selected for the experiments because of its well-behaved, self-limited ALD reaction and widely understood growth characteristics and mechanisms. According to previous experiments, this deposition should yield a material with a composition of approximately $Al_2O_{3.2}H_{0.4}$, which is approximately a 2:1 mixture

of Al_2O_3 and AlOOH.[38] Following ALD of amorphous alumina, the material was removed from the NaCl by spin coating a PMMA film on top, washing the NaCl away via flotation at an air-water interface, and scooping the alumina/PMMA film off the air-water interface with a substrate such as a holey TEM grid. Afterwards, the PMMA was removed via washing with organic solvents, resulting in a crack-free, centimeter-scale film. The complete fabrication process from substrate design to film transfer is illustrated in Figure 3.1 and detailed in the Methods section. Using this strategy, alumina growth was compared between the as-cleaved NaCl substrates and the plasma-activated substrates.

Materials deposited without plasma activation did not grow uniformly and exhibited incomplete coalescence. Ribbon-like pieces of alumina were observed via bright field (BF) optical microscopy, possibly due to film nucleation along surface steps of the NaCl wafer (Figure 3.2a). Indeed, the morphology of the alumina wires closely resembles that of the NaCl surface steps (Figure 3.6a). Incomplete coalescence was confirmed via transmission electron microscopy (TEM) imaging, which revealed small islands of alumina that joined to form thin, parallel wires (Figure 3.2b).

In contrast, when the NaCl surface was first activated via an N_2 plasma, a film-type growth mode was observed via BF optical microscopy and TEM imaging (Figure 3.2c and 3.2d). The images indicate that the deposited film, which was synthesized at the cm-scale, achieved complete coalescence. This improved uniformity presumably emerges from an increased density of available nucleation sites in addition to the naturally occurring surface steps. Such deposition is desirable for ultrathin amorphous film growth, such that materials are synthesized without gaps and pinholes yet remain structurally amorphous.

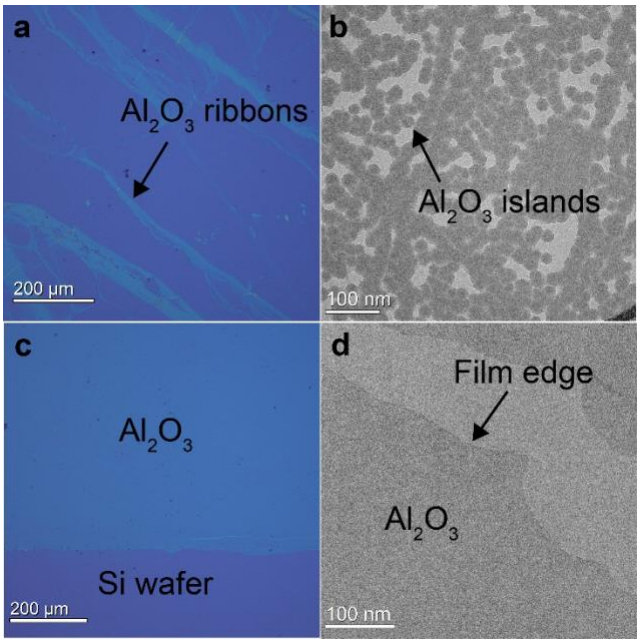


Figure 3.2. Growth of alumina on NaCl by atomic layer deposition. (a,b) An alumina material deposited without plasma pre-treatment and transferred from NaCl to Si/SiO_2 wafers, imaged under (a) bright-field (BF) optical microscopy and (b) transmission electron microscopy (TEM). (c,d) A ~5 nm-thick alumina material deposited with a plasma irradiation step, imaged under (c) BF optical microscopy and (d) TEM.

To examine the structure of these materials, we collected electron diffraction patterns from a sample that had been transferred to a TEM grid. The absence of discernable diffraction spots or rings indicates that the materials are fully amorphous. These diffraction patterns were processed to obtain electron pair distribution functions (ePDF), which reveal the bonding and coordination characteristics of the material (Figure 3.3a).[39] We attribute the first peak at 1.80 Å to a first coordination shell of Al-O interatomic distances, which is notably shorter than the average 1.93 Å Al-O bond distance in α-Al_2O_3 (the most thermodynamically stable crystalline phase of Al_2O_3). Similarly short Al-O bond distances have been observed in the ePDF of an amorphous alumina

structure.[40] The second coordination shell occurs at 3.01 Å, which is also consistent with previous reports and is assigned to overlapping peaks from the O-O and Al-Al interatomic distances.[40,41] The peaks decrease in intensity at larger distances (Figure 3.3a), as expected for an amorphous material. This TEM-based characterization demonstrated that ultrathin glassy alumina was successfully prepared with our tailored NaCl substrates.

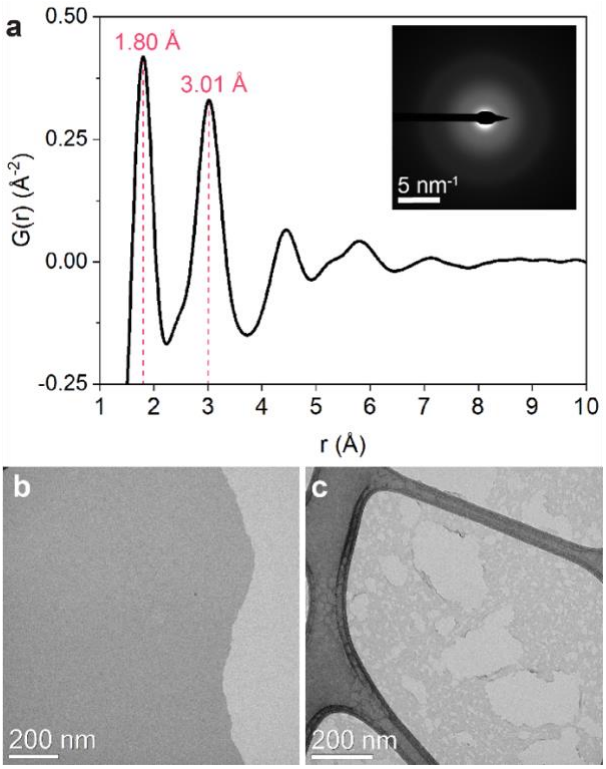


Figure 3.3. (a) Electron pair distribution function of 5 nm alumina material prepared by the fabrication process illustrated in Figure 3.1. (b,c) TEM images of alumina materials prepared with (b) 10 cycles (1.5 nm thickness) or (c) 7 cycles of ALD. Contrast differences between images arise from the lacey carbon that is imaged in (c).

In addition to uniform deposition, a second challenge in the preparation of freestanding 2D materials lies in transferring the materials without significant contamination. In graphene transfer, contamination from undissolved polymer residue or the degraded substrate has been noted to limit

the performance of materials. To investigate the cleanliness of our 2D glasses, we performed spectroscopic measurements on our materials. X-ray photoelectron spectroscopy (XPS) of alumina after transfer to a Si wafer revealed trace quantities of Na and Cl (Figure 3.4, Table 3.1). These small quantities suggest that while most NaCl was removed, some ions remained underneath the alumina and were trapped by the wafer. We hypothesize that complete NaCl removal should be possible for a freestanding material, where the trapping of NaCl cannot occur. A small amount of F was also observed from the peaks at 830 and 680 eV, which we attribute to contamination in the ALD reactor.

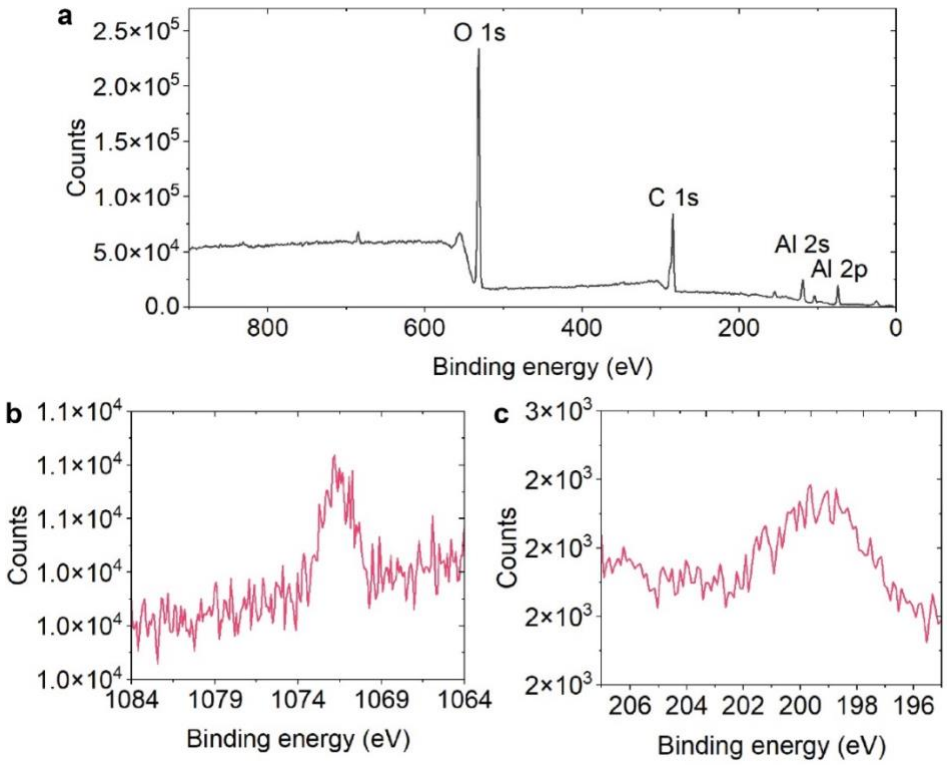


Figure 3.4. (a) XPS spectrum of nominally 5 nm-thick alumina after transfer to a Si/SiO_2 wafer. High-resolution spectra of (b) Na 1s and (c) Cl 2p shows trace amounts remaining in the material.

Table 3.1. Quantified elemental composition from XPS survey scan of nominally 5 nm ALD-alumina on a Si/SiO_2 wafer.

Peak ID	Atomic conc. (%)	Error (%)
Cl 2p	0.1	0.01
Si 2p	4.1	0.03
O 1s	43.0	0.08
Na 1s	0.2	0.02
Al 2p	15.6	0.07
C 1s	37.0	0.09

PMMA removal from the top surface of the alumina film could not be clearly assessed by XPS because the carbon signals from PMMA are similar to those from adventitious carbon. Instead, surfaces were examined with AFM-based infrared spectroscopy (AFM-IR). Figure 3.5a shows the topography scan of the sampled region, which shows a textured surface that we attribute to trapped water from the transfer process. Figure 3.5b shows the IR intensity at 1600 cm^{-1} of the same region. The nano-IR spectra showed that this peak was not well defined and overlapped with other peaks, and so we partially attribute this signal to a H-O-H scissors mode from water.[42] In contrast, Figure 3.5c does not show a strong signal at 1730 cm^{-1}. Because this wavenumber corresponds to the C=O stretch of PMMA, this result is consistent with the removal of PMMA.[43] Overall, these results show that the gentle transfer process offered by the heterogeneous substrate yields materials with minimal contamination and damage.

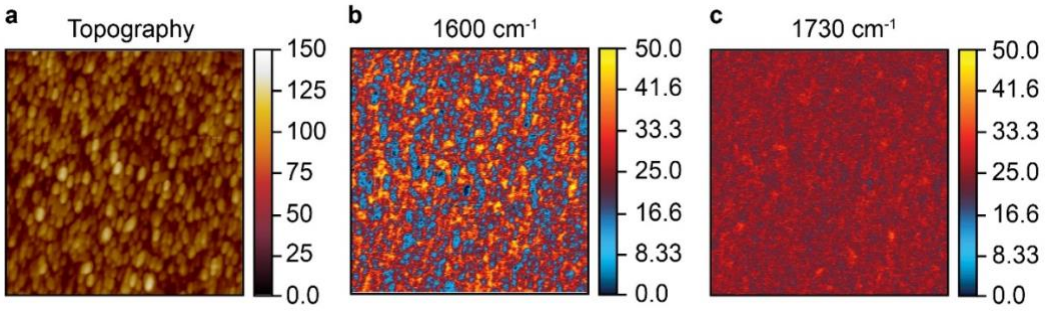


Figure 3.5. AFM-IR of nominally 5 nm-thick alumina that was transferred to a Si/SiO_2 wafer. The same scan shows the (a) topography and IR intensity at (b) 1600 cm^{-1} and (c) 1730 cm^{-1}.

Given the success of nucleating ALD and transferring materials, we sought to determine how thin these materials can be while achieving full coalescence. For the materials prepared in our ALD system, ellipsometry was used to determine an average growth rate of 1.54 Å/cycle over 50 ALD cycles, which is slightly greater than the literature growth rates for thermal ALD (1.1 Å/cycle at 150 °C) but comparable to that of remote plasma-enhanced ALD (1.7-1.0 Å/cycle between 25-300 °C).[44,45] To find the lower bound of thickness for a uniform alumina material, materials were deposited with 7 and 10 cycles of ALD. After 10 cycles, the material was measured to be 1.5 nm thick by ellipsometry and appears coalesced without exhibiting pinholes or island-like growth, as shown by the TEM images in Figure 3.3b. After 7 cycles, these defects are present and conformal deposition was not achieved (Figure 3.3c). Thus, we find that the use of a plasma-irradiated NaCl substrate allows the growth of coalesced alumina down to a thickness of 1.5 nm.

3.2.2 Mechanism of NaCl surface activation

To understand how plasma treatment led to uniform ALD growth, we investigated the role of plasma power in NaCl surface roughening. We hypothesized that the plasma would produce defects on the NaCl surface that could nucleate ALD growth. At a plasma power of 100 W, atomic force microscopy (AFM) measurements showed that the surface had indeed roughened in

comparison with the untreated surface and now had pits 2-3 nm in depth (Figure 3.6a and c), possibly due to ion bombardment from the plasma.[46] At a lower plasma power (25 W), AFM revealed no surface roughening (Figure 3.6b). Surprisingly, a continuous alumina film grew on the NaCl after plasma irradiation of either 100 or 25 W. We therefore concluded that the roughening of the NaCl surface was not essential for nucleating uniform ALD growth.

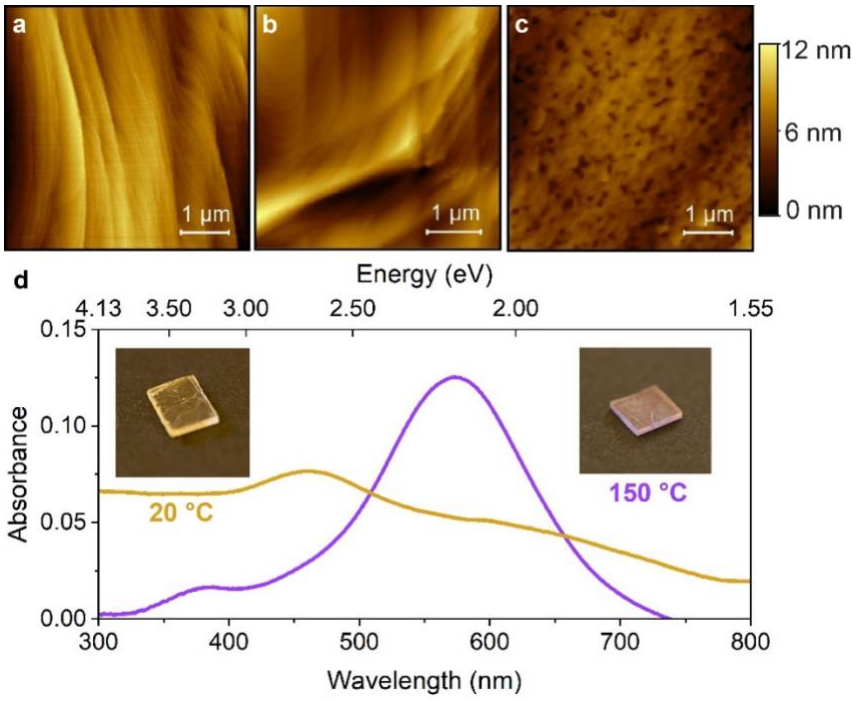


Figure 3.6. AFM surface topology scans of mechanically cleaved single crystal NaCl slabs after (a) no plasma treatment, (b) 5 min of 25 W N_2 plasma irradiation, and (c) 5 min of 100 W N_2 plasma irradiation. (d) UV-visible spectra of NaCl with 15 min of 100 W N_2 plasma irradiation at ambient temperature (20 °C, yellow line) and ALD growth temperature (150 °C, purple line). Insets in (d) are photographs of the NaCl crystals (7 mm x 5 mm x 1 mm) after plasma irradiation at 20 °C (left inset) and 150 °C (right inset).

Previous experiments showed that irradiation of NaCl with either electrons or ions led to the loss of Cl and the trapping of a bare electron in Cl vacancies, called F-centers.[45,47,48] We

therefore suspected that irradiation with plasma, which has free electrons and ions, could also produce F-centers. In fact, after plasma irradiation, the NaCl adopted either a yellow color (irradiation at 25 °C) or a purple color (irradiation at 150 °C). To interpret these observations more quantitatively, we performed UV-vis transmission spectroscopy on the NaCl crystals (Figure 3.6d). The yellow crystal's absorbance had a peak centered at 462 nm, which is close to the literature value (460 nm) of F-centers in NaCl.[48,49] The purple crystal had large and small peaks in absorbance at 574 nm and 388 nm, which was inconsistent with F-centers. Previous studies have suggested self-trapped holes or excitons as possible explanations for the 388 nm peak.[49,50] However, these explanations have been opposed due to the high transience of these phenomena.[49]

We hypothesized that this peak may also be explained by the Na colloids that form upon plasma irradiation at elevated temperatures. To investigate this hypothesis, we used Mie theory to model the absorption of colloids over a range of diameters (Figure 3.7). In these modeled spectra, a high-energy feature emerges with increasing colloid diameter. This peak is a quadrupole plasmon mode of the colloid, which grows in intensity as the colloid becomes increasingly capable of housing plasmon resonances above the dipole mode. These modeled peaks were compared to our experimental result, which displays excellent qualitative agreement, but a blue-shift in the wavelength of the quadruple mode. We suggest that this difference could be due to local changes in the refractive index of the strained and distorted NaCl medium surrounding the colloids, which is not accounted for in the modeled data.

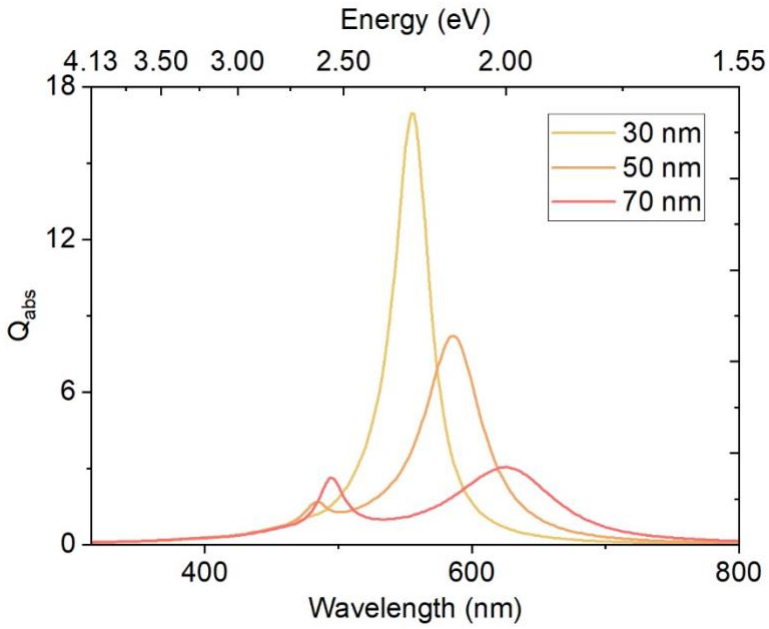


Figure 3.7. Modeled absorption coefficients of Na colloids at 30, 50, and 70 nm diameters. The modeling was performed with an implementation of Mie theory originally written by Bohren and Huffman.[51,52] Refractive indices were obtained from Inagaki et al.[53]

To examine if the 388 nm peak is indeed due to a quadrupole mode of Na colloids, this feature was further analyzed. According to Mie theory, the FWHM of the UV-vis absorption peak is indicative of colloid size when colloid diameters are below the electron mean free path in a bulk material. Electrons in bulk Na have a mean free path of 35 nm, corresponding to a predicted linewidth of 0.02 eV.[54] This linewidth is significantly narrower than the 0.49 eV linewidth of the experimental 574 nm peak in Figure 3-6, which suggests a lower limit of 30 nm in diameter.[48,54] We estimated an upper limit of colloid sizes by comparing the relative intensities of the quadrupole and dipole peaks to predicted absorption coefficients of colloids over a range of diameters. The relative intensity of the quadrupole peak to the dipole peak showed qualitative agreement with a predicted spectrum of 50 nm colloids (Figure 3.7). For this reason, we expect that colloids formed

within the plasma-irradiated NaCl are approximately 30-50 nm in diameter. Colloids could not be observed under polarized light microscopy (Figure 3.8), supporting the conclusion of extremely small colloid diameters that could give rise to the observed absorption peaks. Therefore, we tentatively assign the two features to the different order plasmon resonances from Na colloids. Ultimately, our UV-vis measurements provided direct evidence of F-centers in the low-temperature sample and indirect evidence of F-centers in the high-temperature sample.

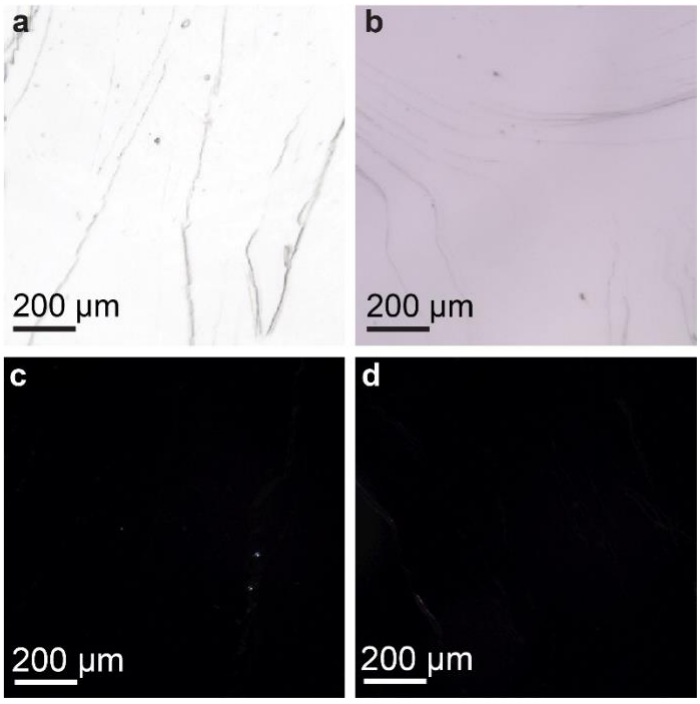


Figure 3.8. Bright field optical microscopy of NaCl (a) prior to N_2 plasma irradiation and (b) following 15 min of 100 W capacitively coupled N_2 plasma irradiation at 150 °C. Corresponding images under polarized light microscopy are shown (c) before and (d) after plasma irradiation, demonstrating the absence of colloids with large scattering cross sections.

For insight into the surface structure of irradiated NaCl, we also sought to determine the distribution of F-centers from the UV-vis measurements. Direct interpretation of F-centers in the high-temperature sample was difficult, however, because the formation of Na colloids from F-

centers reduced its spectral intensity. During plasma irradiation, however, a steady state concentration of F-centers should exist at the surface, where they form, before diffusing into the interior of the NaCl. In fact, in the low-temperature sample, we calculated the area density of F-centers as 1.9×10^{15} per cm^2 using Smakula's equation (see section 3.3.5). Notably, this area density is ten times higher than the number of Cl surface sites on NaCl.[55] To achieve such a high area density of F-centers implies that the F-centers must have diffused into the interior of the NaCl crystal.

ALD growth of alumina was commenced immediately after plasma irradiation ceased in both the low- and high-temperature samples. We therefore hypothesized that F-centers at the NaCl surface were crucial for nucleating film growth. The high reactivity of such surface F-centers made direct experimental measurements challenging, however. Instead, we performed DFT calculations to determine whether F-centers in NaCl are more stable at the surface or interior of crystals (Table 3.2). Our calculations on NaCl slabs revealed that F-centers are 164 meV more stable at the surface ("first layer") than in the crystal interior, whereas they are 38 meV more stable at the sub-surface ("second layer") than in the crystal interior. The insight into F-center stability at surfaces, combined with the fact that F-centers are created at the NaCl surface, suggest that the F-center concentration will be highest at the NaCl surface under our experimental conditions. Therefore, even if ALD is performed at a high temperature at which F-centers are increasingly mobile, a surface population of F-centers is available to nucleate ALD growth.

These findings suggest that F-centers were formed with the 25 W and 100 W plasma treatments, whereas the pits formed only at 100 W. Because the continuous alumina films nucleated and grew with either plasma treatment, we conclude that F-center defects play a primary role in facilitating ALD growth.

Table 3.2. DFT-calculated energetic cost of an F-center at different depths within NaCl

Sample	Energy/site (eV)
Pristine	0
1st layer (surface)	4.66
2nd layer	4.78
3rd layer	4.82
4th layer	4.82

3.2.3 Hydroxylation of surface-activated NaCl

To understand how ALD nucleation occurs following plasma irradiation, we further characterized the NaCl surface. Our ALD process used water as a precursor, which is known to react with F-centers to form surface hydroxyls.[56,57] We therefore measured the surface composition of the pristine and plasma-treated samples via XPS (Figure 3.9a). For the pristine NaCl crystal, we measured an average Cl:O (at.%:at.%) ratio of 98:2. To interpret this ratio, we apply a model in which the oxygen is located only in the first layer of the NaCl crystal. This model is justified by our DFT calculations, which show that a surface hydroxyl group is 91 meV more stable at the surface than in the interior (Table 3.2). In XPS, the signal intensity of the sample decays exponentially from the surface, leading to measurements that reflect ~10 nm in sample depth.[58] As a result, the atomic ratios of Cl:O include Cl intensity that partially originated from beneath the surface layer in which the adsorbed hydroxyl groups are present. To determine the Cl present at the NaCl surface, we therefore needed to re-scale the XPS-measured atomic ratios.

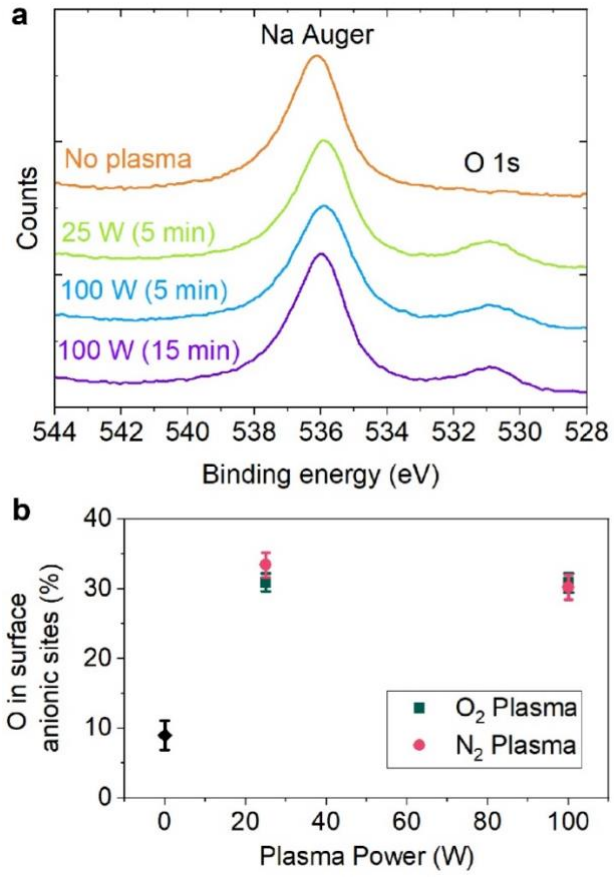


Figure 3.9. (a) High-resolution O 1s XPS spectra of NaCl after varying plasma pre-treatments. (b) Calculated occupancy of oxygen in surface anionic lattice sites from quantified XPS. The values were calculated using a correction factor for the measured chlorine content of 0.246 to account for the signal measured from sub-surface chlorine.

This correction was performed by applying an approximate correction factor, which was determined as follows. The surface sensitivity of XPS decays exponentially in accordance with Beer's Law:

$$I = I_0 e^{-d/\lambda} \quad (3\text{-}1),$$

where I is the intensity attributable to the sample below depth d, I_0 is the total intensity, and λ is the attenuation length.[58] Because λ is closely related to the inelastic mean free path (IMFP) of the

electron, λ was approximated with the IMFP of an emitted Cl 2p electron traveling through NaCl (λ = 10.6 Å).[59] To find the fraction of the signal intensity that arises from below the surface layer of NaCl, *d* was selected as the depth of an NaCl layer (d = 2.79 Å). Thus, the remaining fraction of the total intensity arises from electrons emitted from the surface. This approximation yields a scaling factor of 0.246, which was applied to the Cl atomic % obtained from quantified XPS to obtain the concentration of Cl at the NaCl surface.

Using this scaling factor, we re-scaled the Cl:O ratios to estimate the ratio in the top atomic layer of NaCl. Thus, the measured 98:2 ratio of pristine NaCl is 91:9. The oxygen measured on this un-treated NaCl surface is partially attributable to the characteristic peaks of adventitious carbon observed at 284.6 and 288-289 eV, which indicates that the adventitious carbon contained oxygen.[60] In addition, small quantities of surface-adsorbed H_2O or OH^- are also known to exist on NaCl under ambient conditions.[36] In comparison, samples treated with 25 and 100 W N_2 plasma had approximately 33% and 30% O, respectively (Figure 3.9b). The similar surface oxygen concentrations between the treated samples suggest that the same oxidation mechanism occurs on both samples—i.e., oxidation occurs via the formation of F-centers rather than surface roughening. Repeating these experiments with O_2 plasma revealed similar surface O concentrations (Figure 3.9b).

Since our ALD process uses water, the reaction in eqn. 3-2 is likely operational:

$$NaCl_{1-x}[e^-]_x + x\ H_2O \rightarrow NaCl_{1-x}[OH^-]_x + \tfrac{1}{2} x\ H_2 \quad (3\text{-}2).$$

We estimate the surface hydroxyl concentration by attributing the approximately 20% increase in oxygen content to the inserted hydroxyl groups, which indicates that approximately one-fifth of the Cl^- sites at the surface have been replaced with a hydroxyl. We note that samples were exposed to air during transfer to the XPS instrument, providing an oxygen source for all

samples. While XPS analysis yielded consistent results when performed on the same day, some variability was observed among the experiments performed on different days, suggesting a possible role of atmospheric humidity in the total oxygen content of samples transferred through air to the XPS instrument. When the substrate is kept under vacuum for subsequent ALD, H_2O was present as a precursor and could therefore also serve as an oxygen source.

Because a higher hydroxyl concentration should offer more nucleation sites for ALD, we aimed to understand whether the surface hydroxyl concentration could be increased. We varied the plasma pre-treatment time, using 5 or 15 minutes, but found that both resulted in similar oxygen concentrations (Figure 3.9a). Combined with our observation that increasing the plasma power does not increase the oxygen content, we conclude that we reached the upper limit for the oxygen content on NaCl surfaces. Such an upper bound must arise from a concentration limit of F-centers or hydroxyls at the NaCl surface, which contrasts with our aforementioned spectral data and previous literature indicating that F-centers prefer to aggregate and form colloids.[61–63] However, thermodynamic or kinetic effects at the surface may be responsible for imposing a concentration limit that does not exist in the crystal's interior. The thermodynamic factors for a concentration limit may include lattice strain from the significant size mismatch upon replacing Cl^- with an electron or electrostatic repulsion between F-centers due to decreased screening at the surface. In particular, increased repulsion between F-centers has been observed in CaF_2.[64] Ultimately, the concentration limit observed from XPS suggests that the energetic cost of adding an F-center to the surface increases as the surface F-center concentration increases.

In addition to concentration, another important factor that controls ALD nucleation is the reactivity of hydroxyls. When water dissociates in the presence of an F-center, previous studies have shown that the hydroxyl sits inside the Cl^- vacancy and is strongly adsorbed due to

interactions with the surrounding Na^+.[65] As a result, we expected this reactivity to differ from that of hydroxyls that are fully exposed above the surface. To compare the reactivity of hydroxyls for ALD in different environments, we performed DFT calculations for the reaction in eqn. 3-3 on surface slabs of NaCl and sapphire:

$$[OH^-] + Al(CH_3)_3 \rightarrow [O]\text{-}Al(CH_3)_2 + CH_4 \quad (3\text{-}3).$$

The sapphire system, in which TMA reacts with an OH^- dangling bond on Al_2O_3, is a strongly favorable reaction with a reaction enthalpy of -1.82 eV. When the hydroxyl group was embedded in the surface layer of NaCl, the reaction enthalpy was -1.59 eV. The difference between these two systems may be explained by the greater steric constraints for the hydroxyl that is embedded in NaCl. Nevertheless, these calculations reveal that nucleation on an embedded hydroxyl is still a highly exothermic reaction and is consistent with the successful nucleation of ALD growth in Fig. 3.2.

3.2.4 Fabrication of freestanding titania

To investigate the generalizability of our method, we prepared ALD titania as a freestanding and large-area material. For ALD of titania, the substrate had to be transferred to an alternative instrument following plasma treatment. Due to the high reactivity of surface F-centers in air, 3 cycles of alumina ALD were performed before transferring the substrate. As observed in Figure 3.3c, these few cycles produce a sub-monolayer of alumina on the surface. By doing so, F-centers nucleate alumina, which serves as reactive sites for the ALD of titania. For titania growth, 106 cycles of a standard tetrakis(dimethylamido)titanium/H_2O recipe was used at 150 °C, which is expected to produce a film 5 nm thick of amorphous titania based on a standard growth rate of 0.5 Å/cycle.[66]

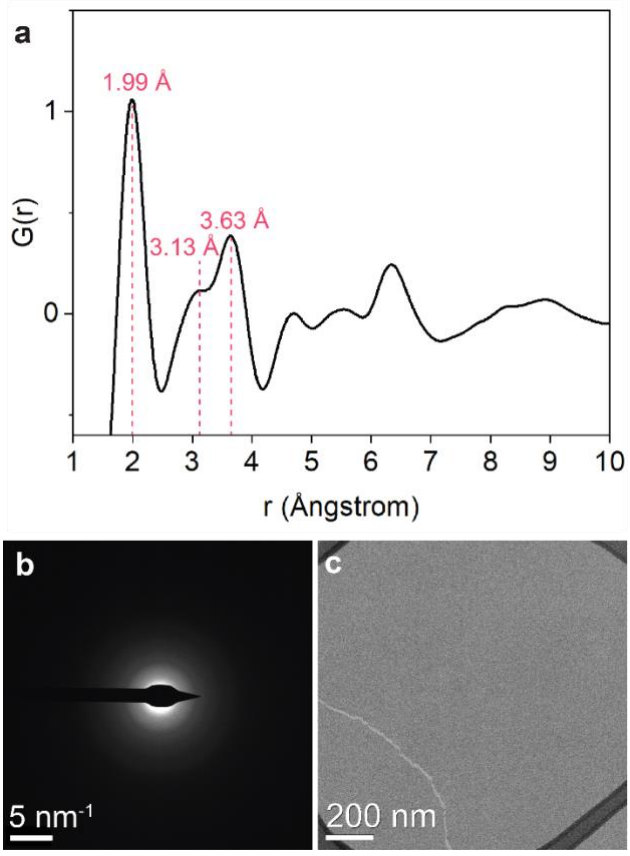


Figure 3.10. (a) Electron pair distribution function and (b) corresponding electron diffraction pattern of nominally 5 nm titania on top of 3 cycles of alumina. (c) TEM image of titania over a lacey carbon grid. A crack in the material has been included to provide contrast.

Following removal from the NaCl substrate, the material was characterized to examine its structure. Electron diffraction and the corresponding pair distribution function revealed a fully amorphous structure (Figure 3.10a,b). The first peak of the pair distribution function (1.99 Å) agrees well with previous characterizations of the amorphous Ti-O interatomic distance at 1.96 Å.[67] The second and third peaks at 3.13 and 3.63 Å are consistent with the range of Ti-Ti distances that have been identified by additional studies.[68,69] These studies also found the O-O peak overlaps

heavily with the first Ti-Ti peak, making this peak difficult to distinguish.[69] In addition to structural features, TEM imaging showed high uniformity and cleanliness of the material (Figure 3.10c).

To investigate the composition of the material, a film was also transferred to a Si/SiO_2 wafer for XPS. Figure 3.11a shows the wide scan spectrum, which indicates the presence of Ti and O on the surface. We expect that the trace amounts of Zn (1021.7 eV) and Ca (346.7 eV) in this scan arise from contamination from previous depositions in the same ALD instrument. High-resolution spectrum of the Ti 2p region shows peaks at 463.8 eV and 458.1 eV, which are consistent with the 2p 1/2 and 2p 3/2 peaks of TiO_2 (Figure 3.11b).[70] The high-resolution scan of the O 1s region shows a peak at 529.5 eV, which agrees with the binding energy in TiO_2,[70] while we assign the additional peaks centered around ~532 eV to organic species from adventitious carbon (Figure 3.11c). Due to this adventitious carbon, an exact stoichiometry could not be determined, although quantification of the wide spectrum showed significant quantities of Ti and O (Table 3.3). These analyses demonstrate the successful deposition of freestanding large-area titania as an ultrathin ALD material.

Table 3.3. Quantified elemental composition from XPS survey scan of nominally 5 nm ALD-titania on a Si/SiO_2 wafer.

Peak ID	Atomic conc. (%)	Error (%)
Zn 2p 3/2	0.3	0.06
N 1s	0.5	0.18
Ca 2p	0.5	0.08
Ti 2p	13.0	0.05
O 1s	44.8	0.14
Si 2p	3.1	0.07
C 1s	37.7	0.13

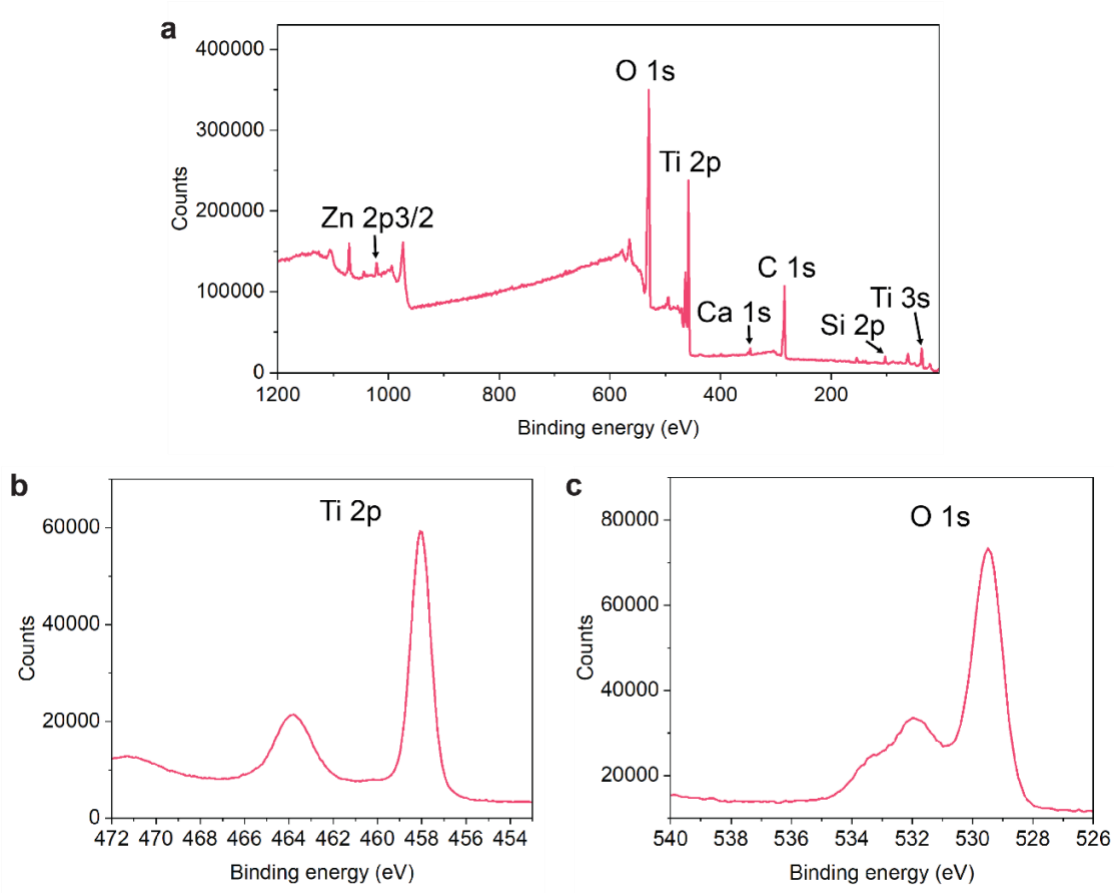


Figure 3.11. (a) XPS survey spectrum of nominally 5 nm-thick titania after transfer to a Si wafer with a SiO_2 thermal oxide. High-resolution spectra of (b) Ti 2p and (c) O 1s.

From these results, we expect that our method may be further generalized to other ALD compositions, with slight adjustments to the ALD recipe. When doing so, an important consideration is the possible change in -OH^- surface density depending on the recipe temperature. The increased mobility of F-centers at higher temperatures may lead to relatively increased rates of defect recombination or colloidal formation compared with surface -OH^- formation, thereby resulting in delayed film coalescence. Additionally, extremely high temperatures may cause the desorption of -OH^-, and the initial cycles may need to be performed at slightly lower temperatures to induce nucleation. After nucleation, desorption is less likely, and deposition should be possible at higher temperatures. A similar strategy may also be used to promote the monolayer formation

of materials with less favorable interactions between the precursor and embedded hydroxyl. By initially performing several cycles of alumina ALD, as we have demonstrated with our preparation of titania, accessible nucleation sites are introduced to the surface. With such modifications, the generalization to a wide variety of freestanding 2D amorphous materials should be readily possible.

3.3 Methods

3.3.1 Preparation of alumina on NaCl

Single crystal NaCl (SPI-Chem; NaCl 25 mm cubes) was mechanically cleaved along the (100) plane to reveal a newly exposed atomically flat surface. Crystals were immediately loaded into a custom ALD reactor with a capacitively coupled plasma generator directly above the main reactor chamber. Substrate surfaces were treated with 5 minutes of N_2 plasma at 100 W and an RF frequency of 13.56 MHz. ALD of alumina was performed at 150 °C for 30 cycles with trimethylaluminum (TMA; Strem, min. 98% purity) and H_2O (Sigma-Aldrich, HPLC Plus) as precursors with the following steps: 1) 0.2 s TMA pulse, 2) 40 s N_2 purge, 3) 0.2 s H_2O pulse, 4) 40 s N_2 purge. The flow rate of the N_2 carrier gas was 20 sccm.

3.3.2 Preparation of titania on NaCl

NaCl substrates were cleaved according to the same procedure as alumina samples. The substrates were treated with 5 min of N_2 plasma at 25 W and an RF frequency of 13.56 MHz. Following plasma treatment, 3 cycles of alumina ALD were performed using the same recipe as the alumina deposition described above. ALD of titania was then performed for 106 cycles with tetrakis(dimethylamido)titanium (TDMA-Ti; Strem, 99% purity) and H_2O (Thermo Fisher, HPLC grade). The flow rate of the N_2 carrier gas was 90 sccm. The reaction chamber was maintained at 150 °C, while the TDMA-Ti was heated to 75 °C and the H_2O was kept at room temperature. Each

cycle of ALD consisted of the following steps: 1) 0.1 s TDMA-Ti pulse, 2) 10 s N_2 purge, 3) 0.015 s H_2O pulse, 4) 5 s N_2 purge. Given the expected growth rate of 0.5 Å /cycle, this process produced a film with a nominally 5 nm thickness.[66]

3.3.3 NaCl removal and PMMA-assisted transfer

Materials were spin-coated with polymethyl methacrylate (PMMA) in anisole (KemLabs, 1000 Harp eB 0.1) at 2500 rpm for 1 min. This process left an approximately 70 nm-thick layer on top of the alumina, according to publicly available spin curves by the manufacturer. The PMMA coating was cured in a vacuum oven at 140 °C for 40 min. The cured materials were transferred to a water bath at room temperature, where they were gently placed on the surface of the water so that the sample floated at the air-water interface while the underlying NaCl dissolved in water. NaCl was fully removed after 30 minutes and the remaining PMMA-alumina material was picked up with a cleaned Si wafer from below, so that the PMMA coating remained on top. The material was rinsed with DI water and dried under ambient conditions. The PMMA was removed by soaking the sample in an acetone (Fisher Chemical, electronic grade) bath for 16 hrs. The final product was rinsed with electronic grade acetone and isopropanol prior to characterization.

3.3.4 Materials characterization

Spectroscopic ellipsometry was used to obtain thickness measurements of the fabricated materials on Si wafers with a thermal oxide. A J.A. Woollam VASE ellipsometer was operated at wavelengths between 500-900 nm at a fixed angle of 70°. A Cauchy model was used to fit Δ and ψ for thickness measurements, using a refractive index of a = 1.63 and b = 0.02.

AFM was performed with an Asylum Research MFP3D instrument and processing using Gwyddion software. A silicon cantilever was used in tapping mode with a scan rate of 0.5 Hz and 512x512 pixel resolution. AFM-IR measurements were performed with a Bruker Anasys nanoIR3

and measured in tapping mode. Each AFM scan provides a topography and phase map of the specified area, and by varying the wavenumber of the incident IR laser, an IR intensity map was collected concurrently. By repeating scans at different wavenumbers, a set of IR maps was obtained of the same area. Each AFM scan was taken at a 1 x 1 μm scan size and a 512 x 512 resolution. Individual spectra were also taken at 4 different locations in this scanned area.

TEM was performed with a Thermo Fisher Talos F200X and was operated at 200 kV in bright field and nano-beam diffraction mode. Samples were prepared on a Cu mesh grid with lacey carbon support. Film coalescence was inspected with a Nikon Eclipse E600 optical microscope under bright field illumination. Bright field and polarization light microscopy on NaCl were performed with an Olympus BX61 microscope.

XPS data was collected on a Kratos Axis Ultra Delay-Line Detector (DLD) system with a monochromatic Kα x-ray source (1486.6 eV) operated at 150W. A charge neutralizer was used to prevent sample charging, and often charge neutralizer conditions (filament current, charge balance, and filament bias) had to be adjusted to obtain spectra with the narrowest FWHM and highest peak intensities. All spectra were corrected to the C 1s peak at 284.6 eV. Survey and high-resolution scans were acquired at pass energies of 80 eV and 20 eV, respectively, and the analyzed spot size was 300 x 700 μm.

3.3.5 Quantification of F-centers

The FWHM of a peak in a UV-vis spectrum can be used to quantify the number of F-centers with Smakula's equation:[55]

$$Nf = \frac{mc}{\pi e^2 h}\left(\frac{3}{n^2+2}\right)^2 n \frac{1}{2}\pi k_m W_{1/2} \quad (3\text{-}4).$$

Here, N is the number of F centers per cm^{-3}, f is the oscillator strength, n is the refractive index of the NaCl, k_m is the maximum absorption coefficient in cm^{-1}, and $W_{1/2}$ is the FWHM in eV. The following values have been used for the constants above, in accordance with previous

evaluations:[48] f= 0.86, n = 1.54, e = 4.8×10^{-10} esu, h = 4.14×10^{-15} eV s, c = 2.998×10^{10} cm s^{-1}, and m = 9.11×10^{-28} g. To determine k_m from the absorbance measured in the UV-visible spectra, the following relationship was used:[71]

$$k_m = 2.303 \frac{A_{max}}{t} \quad (3\text{-}5).$$

where A_{max} is the maximum absorbance and t is the sample thickness.

3.3.6 DFT Calculations

Spin-polarized DFT calculations were performed with VASP using the PBE functional.[72,73] An energy cut-off of 570 eV, Gaussian smearing (50 meV), DFT-D3 with Becke-Johnson damping, convergence of 10^{-6} eV/atom and a KSPACING of 0.3 were utilized.[74,75] For both bulk and surface slabs, convergence testing of supercell size was performed. For bulk, calculations were performed from 2×2×2 to 5×5×5 supercells with good convergence achieved with a 3×3×3 supercell. For surface slabs, calculations were performed from 2×2×2 to 5×5×5, with good convergence achieved for a 4×4×2 surface slab.

3.4 Conclusions

ALD materials, which typically have strong sample-substrate interactions, make conventional methods of lift-off or film transfer unsuitable. In this work, we have designed a heterogeneous NaCl substrate that facilitates the growth of a thin, free-standing ("2D") amorphous material. The ability to produce free-standing materials or transfer them to arbitrary substrates allows the investigation of novel structure-property relationships. For these future studies, integrating ALD-specific advantages such as precise compositional control can yield layered or heterogeneous structures as freestanding ultrathin materials. Additionally, our method, which relies on a tailored substrate, may also be combined with other growth methods such as area-selective ALD to allow for templated ultrathin materials with nanoscale designs.[76]

We also expect that the substrate design principles explored in this work are applicable to substrates beyond NaCl. For the selection of suitable substrates for the described plasma treatment, we suggest two main criteria. First, substrates should be removable via gentle methods such as dissolution. This criterion is necessary for large-area materials, which may undergo damage from strain or corrosion by etching chemicals. Second, substrates should form F-centers upon plasma irradiation. This requirement is necessary if surfaces do not already have sufficient nucleating sites for ALD growth. F-centers are known to form in various material types, including alkali halides (such as NaCl) and metal oxides.[77] However, the removal of metal oxides typically requires harsh etchants that are likely to dissolve the ALD material, making these substrates less preferable. Thus, we suggest candidates such KCl and similar alkali halides are potential alternative substrates for the successful preparation of large-area freestanding materials.

REFERENCES

(1) Nomura, K.; Ohta, H.; Ueda, K.; Kamiya, T.; Hirano, M.; Hosono, H. Thin-Film Transistor Fabricated in Single-Crystalline Transparent Oxide Semiconductor. *Science* **2003**, *300* (5623), 1269–1272. DOI: 10.1126/science.1083212.

(2) Nomura, K.; Ohta, H.; Takagi, A.; Kamiya, T.; Hirano, M.; Hosono, H. Room-Temperature Fabrication of Transparent Flexible Thin-Film Transistors Using Amorphous Oxide Semiconductors. *Nature* **2004**, *432* (7016), 488–492. DOI: 10.1038/nature03090.

(3) Grundmann, M.; Frenzel, H.; Lajn, A.; Lorenz, M.; Schein, F.; von Wenckstern, H. Transparent Semiconducting Oxides: Materials and Devices. *Phys. Stat. Sol. A* **2010**, 207 (6), 1437–1449. DOI: 10.1002/pssa.200983771.

(4) Nasalevich, M.; van Zwol, P. J.; Abegg, E.; Voorthuijzen, P.; Vles, D.; Péter, M.; van der Zande, W.; Vermeulen, H. Researching New EUV Pellicle Films for Source Powers beyond 250 Watts. In *32nd European Mask and Lithography Conference*; Behringer, U. F. W., Finders, J., Eds.; SPIE Proceedings; *SPIE*, **2016**; Vol. 10032, p 100320L. DOI: 10.1117/12.2255040.

(5) Hong, J.; Park, C.; Lee, C.; Nam, K.; Jang, Y.; Wi, S. J.; Ahn, J. Development of Full-Size EUV Pellicle with Thermal Emission Layer Coating. In *International Conference on Extreme Ultraviolet Lithography 2018*; Ronse, K. G., Gargini, P. A., Hendrickx, E., Naulleau, P. P., Itani, T., Eds.; *SPIE*, **2018**; p 25. DOI: 10.1117/12.2501772.

(6) Yeo, J.-H.; Nam, K.-B.; Kang, G.-S.; Hu, Q.; Jeong, C.-Y.; Park, Y.-S.; Lee, S. J.; Jung, J.; Lee, S. H.; Cho, D. H.; Kim, M.-J.; Yoo, J.-B. Development of Nanometer-Thick Graphite Film Extreme Ultraviolet Pellicle with Hydrogen-Resistant TiN Capping Layer. *Mater. Res. Express* **2022**, *9* (6), 066403. DOI: 10.1088/2053-1591/ac7850.

(7) Brouns, D. Development and Performance of EUV Pellicles. *Adv. Opt. Technol* **2017**, *6* (3–4). DOI: 10.1515/aot-2017-0023.

(8) Balaish, M.; Gonzalez-Rosillo, J. C.; Kim, K. J.; Zhu, Y.; Hood, Z. D.; Rupp, J. L. M. Processing Thin but Robust Electrolytes for Solid-State Batteries. *Nat. Energy* **2021**. DOI: 10.1038/s41560-020-00759-5.

(9) Zhu, X.; Schülli, T. U.; Yang, X.; Lin, T.; Hu, Y.; Cheng, N.; Fujii, H.; Ozawa, K.; Cowie, B.; Gu, Q.; Zhou, S.; Cheng, Z.; Du, Y.; Wang, L. Epitaxial Growth of an Atom-Thin Layer on a $LiNi_{0.5}Mn_{1.5}O_4$ Cathode for Stable Li-Ion Battery Cycling. *Nat. Commun.* **2022**, *13* (1), 1565. DOI: 10.1038/s41467-022-28963-9.

(10) Guo, S.; Kou, W.; Wu, W.; Lv, R.; Yang, Z.; Wang, J. Thin Laminar Inorganic Solid Electrolyte with High Ionic Conductance towards High-Performance All-Solid-State Lithium Battery. *Chem. Eng. J.* **2022**, *427*, 131948. DOI: 10.1016/j.cej.2021.131948.

(11) Donders, M. E.; Arnoldbik, W. M.; Knoops, H. C. M.; Kessels, W. M. M.; Notten, P. H. L. Atomic Layer Deposition of $LiCoO_2$ Thin-Film Electrodes for All-Solid-State Li-Ion Micro-Batteries. *J. Electrochem. Soc.* **2013**, *160* (5), A3066–A3071. DOI: 10.1149/2.011305jes.

(12) O'Hern, S. C.; Stewart, C. A.; Boutilier, M. S. H.; Idrobo, J.-C.; Bhaviripudi, S.; Das, S. K.; Kong, J.; Laoui, T.; Atieh, M.; Karnik, R. Selective Molecular Transport through Intrinsic Defects in a Single Layer of CVD Graphene. *ACS Nano* **2012**, *6* (11), 10130–10138. DOI: 10.1021/nn303869m.

(13) Surwade, S. P.; Smirnov, S. N.; Vlassiouk, I. V.; Unocic, R. R.; Veith, G. M.; Dai, S.; Mahurin, S. M. Water Desalination Using Nanoporous Single-Layer Graphene. *Nat. Nanotechnol.* **2015**, *10* (5), 459–464. DOI: 10.1038/nnano.2015.37.

(14) Cao, Z.; Liu, V.; Barati Farimani, A. Water Desalination with Two-Dimensional Metal-Organic Framework Membranes. *Nano Lett.* **2019**, *19* (12), 8638–8643. DOI: 10.1021/acs.nanolett.9b03225.

(15) Safaei, J.; Xiong, P.; Wang, G. Progress and Prospects of Two-Dimensional Materials for Membrane-Based Water Desalination. *Mater. Today Adv.* **2020**, *8*, 100108. DOI: 10.1016/j.mtadv.2020.100108.

(16) Nix, W. D. Mechanical Properties of Thin Films. *Metall. Trans. A* **1989**, *20*(11), 2217–2245. DOI: 10.1007/BF02666659.

(17) Song, K.; Noh, J.; Jun, T.; Jung, Y.; Kang, H.-Y.; Moon, J. Fully Flexible Solution-Deposited ZnO Thin-Film Transistors. *Adv. Mater.* **2010**, *22* (38), 4308–4312. DOI: 10.1002/adma.201002163.

(18) Petti, L.; Münzenrieder, N.; Vogt, C.; Faber, H.; Büthe, L.; Cantarella, G.; Bottacchi, F.; Anthopoulos, T. D.; Tröster, G. Metal Oxide Semiconductor Thin-Film Transistors for Flexible Electronics. *Appl. Phys. Rev.* **2016**, *3* (2), 021303. DOI: 10.1063/1.4953034.

(19) Liu, W.; Wang, H. Flexible Oxide Epitaxial Thin Films for Wearable Electronics: Fabrication, Physical Properties, and Applications. *J. Materiomics* **2020**, *6* (2), 385–396. DOI: 10.1016/j.jmat.2019.12.006.

(20) Chopra, K. L.; Paulson, P. D.; Dutta, V. Thin-Film Solar Cells: An Overview. *Prog. Photovolt: Res. Appl.* **2004**, *12* (23), 69–92. DOI: 10.1002/pip.541.

(21) Lee, C. H.; Kim, D. R.; Zheng, X. Transfer Printing Methods for Flexible Thin Film Solar Cells: Basic Concepts and Working Principles. *ACS Nano* **2014**, *8* (9), 8746–8756. DOI: 10.1021/nn5037587.

(22) Kayes, B. M.; Zhang, L.; Twist, R.; Ding, I.-K.; Higashi, G. S. Flexible Thin-Film Tandem Solar Cells With >30% Efficiency. *IEEE J. Photovoltaics* **2014**, *4* (2), 729–733. DOI: 10.1109/JPHOTOV.2014.2299395.

(23) Kang, K.; Lee, K.-H.; Han, Y.; Gao, H.; Xie, S.; Muller, D. A.; Park, J. Layer-by-Layer Assembly of Two-Dimensional Materials into Wafer-Scale Heterostructures. *Nature* **2017**, *550* (7675), 229–233. DOI: 10.1038/nature23905.

(24) Wang, Y.; Zheng, Y.; Xu, X.; Dubuisson, E.; Bao, Q.; Lu, J.; Loh, K. P. Electrochemical Delamination of CVD-Grown Graphene Film: Toward the Recyclable Use of Copper Catalyst. *ACS Nano* **2011**, *5* (12), 9927–9933. DOI: 10.1021/nn203700w.

(25) Song, J.-G.; Park, J.; Lee, W.; Choi, T.; Jung, H.; Lee, C. W.; Hwang, S.-H.; Myoung, J. M.; Jung, J.-H.; Kim, S.-H.; Lansalot-Matras, C.; Kim, H. Layer-Controlled, Wafer-Scale, and Conformal Synthesis of Tungsten Disulfide Nanosheets Using Atomic Layer Deposition. *ACS Nano* **2013**, *7* (12), 11333–11340. DOI: 10.1021/nn405194e.

(26) Berdova, M.; Ylitalo, T.; Kassamakov, I.; Heino, J.; Törmä, P. T.; Kilpi, L.; Ronkainen, H.; Koskinen, J.; Hæggström, E.; Franssila, S. Mechanical Assessment of Suspended ALD Thin Films by Bulge and Shaft-Loading Techniques. *Acta Mater.* **2014**, *66*, 370–377. DOI: 10.1016/j.actamat.2013.11.024.

(27) Lee, S.; Jeon, Y.; Oh, S. J.; Lee, S.-W.; Choi, K. C.; Kim, T.-S.; Kwon, J. H. Study of Mechanical Degradation of Freestanding ALD Al_2O_3 by a Hygrothermal Environment and a Facile Protective Method for Environmentally Stable Al_2O_3: Toward Highly Reliable Wearable OLEDs. *Mater. Horiz.* **2023**, *10* (10), 4488–4500. DOI: 10.1039/d3mh00669g.

(28) Kukli, K.; Ritala, M.; Aarik, J.; Uustare, T.; Leskelä, M. Influence of Growth Temperature on Properties of Zirconium Dioxide Films Grown by Atomic Layer Deposition. *J. Appl. Phys.* **2002**, *92* (4), 1833–1840. DOI: 10.1063/1.1493657.

(29) Groner, M. D.; Fabreguette, F. H.; Elam, J. W.; George, S. M. Low-Temperature Al_2O_3 Atomic Layer Deposition. *Chem. Mater.* **2004**, *16* (4), 639–645. DOI: 10.1021/cm0304546.

(30) Kim, K. S.; Zhao, Y.; Jang, H.; Lee, S. Y.; Kim, J. M.; Kim, K. S.; Ahn, J.-H.; Kim, P.; Choi, J.-Y.; Hong, B. H. Large-Scale Pattern Growth of Graphene Films for Stretchable Transparent Electrodes. *Nature* **2009**, *457* (7230), 706–710. DOI: 10.1038/nature07719.

(31) Lee, K.; Losego, M. D.; Kim, D. H.; Parsons, G. N. High Performance Photocatalytic Metal Oxide Synthetic Bi-Component Nanosheets Formed by Atomic Layer Deposition. *Mater. Horiz.* **2014**, *1* (4), 419. DOI: 10.1039/c4mh00012a.

(32) Lee, K.; Kim, D. H.; Parsons, G. N. Free-Floating Synthetic Nanosheets by Atomic Layer Deposition. *ACS Appl. Mater. Interfaces* **2014**, *6* (14), 10981–10985. DOI: 10.1021/am502850p.

(33) Edy, R.; Zhao, Y.; Huang, G. S.; Shi, J. J.; Zhang, J.; Solovev, A. A.; Mei, Y. TiO_2 Nanosheets Synthesized by Atomic Layer Deposition for Photocatalysis. *Prog. Nat. Sci.: Mater. Int.* **2016**, *26* (5), 493–497. DOI: 10.1016/j.pnsc.2016.08.010.

(34) Graham, C.; Frances, M. M. M.; Maniyara, R. A.; Wen, Y.; Mazumder, P.; Pruneri, V. NaCl Substrates for High Temperature Processing and Transfer of Ultrathin Materials. *Sci. Rep.* **2020**, *10* (1), 7253. DOI: 10.1038/s41598-020-64313-9.

(35) Xiao, X.; Song, H.; Lin, S.; Zhou, Y.; Zhan, X.; Hu, Z.; Zhang, Q.; Sun, J.; Yang, B.; Li, T.; Jiao, L.; Zhou, J.; Tang, J.; Gogotsi, Y. Scalable Salt-Templated Synthesis of Two-Dimensional Transition Metal Oxides. *Nat. Commun.* **2016**, *7*, 11296. DOI: 10.1038/ncomms11296.

(36) Dai, D. J.; Peters, S. J.; Ewing, G. E. Water Adsorption and Dissociation on NaCl Surfaces. *J. Phys. Chem.* **1995**, *99* (25), 10299–10304. DOI: 10.1021/j100025a035.

(37) Dai, Q.; Hu, J.; Salmeron, M. Adsorption of Water on NaCl (100) Surfaces: Role of Atomic Steps. *J. Phys. Chem. B* **1997**, *101* (11), 1994–1998. DOI: 10.1021/jp9625772.

(38) Dingemans, G.; van de Sanden, M. C. M.; Kessels, W. M. M. Influence of the Deposition Temperature on the C-Si Surface Passivation by Al_2O_3 Films Synthesized by ALD and PECVD. *Electrochem. Solid-State Lett.* **2010**, *13* (3), H76. DOI: 10.1149/1.3276040.

(39) Ehrhardt, K. M.; Radomsky, R. C.; Warren, S. C. Quantifying the Local Structure of Nanocrystals, Glasses, and Interfaces Using TEM-Based Diffraction. *Chem. Mater.* **2021**. DOI: 10.1021/acs.chemmater.1c03017.

(40) Young, M. J.; Bedford, N. M.; Yanguas-Gil, A.; Letourneau, S.; Coile, M.; Mandia, D. J.; Aoun, B.; Cavanagh, A. S.; George, S. M.; Elam, J. W. Probing the Atomic-Scale Structure of Amorphous Aluminum Oxide Grown by Atomic Layer Deposition. *ACS Appl. Mater. Interfaces* **2020**, *12* (20), 22804–22814. DOI: 10.1021/acsami.0c01905.

(41) Gutiérrez, G.; Johansson, B. Molecular Dynamics Study of Structural Properties of Amorphous. *Phys. Rev. B* **2002**, *65* (10), 104202. DOI: 10.1103/PhysRevB.65.104202.

(42) Ferguson, J. D.; Weimer, A. W.; George, S. M. Atomic Layer Deposition of Al_2O_3 Films on Polyethylene Particles. *Chem. Mater.* **2004**, *16* (26), 5602–5609. DOI: 10.1021/cm040008y.

(43) Gong, B.; Parsons, G. N. Quantitative in Situ Infrared Analysis of Reactions between Trimethylaluminum and Polymers during Al_2O_3 Atomic Layer Deposition. *J. Mater. Chem* **2012**, *22* (31), 15672. DOI: 10.1039/c2jm32343e.

(44) Kim, S.; Lee, S.-H.; Jo, I. H.; Seo, J.; Yoo, Y.-E.; Kim, J. H. Influence of Growth Temperature on Dielectric Strength of Al_2O_3 Thin Films Prepared via Atomic Layer Deposition at Low Temperature. *Sci. Rep.* **2022**, *12* (1), 5124. DOI: 10.1038/s41598-022-09054-7.

(45) van Hemmen, J. L.; Heil, S. B. S.; Klootwijk, J. H.; Roozeboom, F.; Hodson, C. J.; van de Sanden, M. C. M.; Kessels, W. M. M. Plasma and Thermal ALD of a Al_2O_3 in a Commercial 200 Mm ALD Reactor. *J. Electrochem. Soc.* **2007**, *154* (7), G165. DOI: 10.1149/1.2737629.

(46) Bruce, R. L.; Weilnboeck, F.; Lin, T.; Phaneuf, R. J.; Oehrlein, G. S.; Long, B. K.; Willson, C. G.; Vegh, J. J.; Nest, D.; Graves, D. B. Relationship between Nanoscale Roughness and Ion-Damaged Layer in Argon Plasma Exposed Polystyrene Films. *J. Appl. Phys.* **2010**, *107* (8). DOI: 10.1063/1.3373587.

(47) Enculescu, M.; Schwartz, K.; Trautmann, C.; Toulemonde, M. Heavy Ion Induced Damage in NaCl and KCl Crystals. *Nucl. Instrum. Methods Phys. Res., B* **2005**, *229* (3–4), 397–405. DOI: 10.1016/j.nimb.2004.12.131.

(48) Seinen, J.; Groote, J. C.; Weerkamp, J. R.; den Hartog HW. Radiation Damage in NaCl. II. The Early Stage of F-Center Aggregation. *Phys. Rev. B* **1994**, *50* (14), 9787–9792. DOI: 10.1103/physrevb.50.9787.

(49) Poston, M. J.; Carlson, R. W.; Hand, K. P. Spectral Behavior of Irradiated Sodium Chloride Crystals under Europa-like Conditions. *J. Geophys. Res. Planets* **2017**, *122* (12), 2644–2654. DOI: 10.1002/2017JE005429.

(50) Fuller, R. G.; Williams, R. T.; Kabler, M. N. Transient Optical Absorption by Self-Trapped Excitons in Alkali Halide Crystals. *Phys. Rev. Lett.* **1970**, *25* (7), 446–449. DOI: 10.1103/PhysRevLett.25.446.

(51) *Absorption and Scattering of Light by Small Particles*; Bohren, C. F., Huffman, D. R., Eds.; Wiley-VCH Verlag GmbH: Weinheim, Germany, 1998. DOI: 10.1002/9783527618156.

(52) Mie, G. Beiträge Zur Optik Trüber Medien, Speziell Kolloidaler Metallösungen. *Ann. Phys.* **1908**, *330* (3), 377–445. DOI: 10.1002/andp.19083300302.

(53) Inagaki, T.; Emerson, L. C.; Arakawa, E. T.; Williams, M. W. Optical Properties of Solid Na and Li between 0.6 and 3.8 EV. *Phys. Rev. B* **1976**, *13* (6), 2305–2313. DOI: 10.1103/PhysRevB.13.2305.

(54) Doyle, W. T. Absorption of Light by Colloids in Alkali Halide Crystals. *Phys. Rev.* **1958**, *111* (4), 1067–1072. DOI: 10.1103/PhysRev.111.1067.

(55) Smakula, A. Über Erregung und Entfärbung lichtelektrisch leitender Alkalihalogenide. Z. Physik 1930, 59, 603–614. DOI: 10.1007/BF01344801.

(56) Fölsch, S.; Henzler, M. Water Adsorption on the NaCl Surface. *Surf. Sci.* **1991**, *247* (2–3), 269–273. DOI: 10.1016/0039-6028(91)90136-G.

(57) Malaske, U.; Pfnür, H.; Bässler, M.; Weiss, M.; Umbach, E. Adsorption Geometry of OH Adsorbed at F Centers on a NaCl(100) Surface. *Phys. Rev. B* **1996**, *53* (19), 13115–13120. DOI: 10.1103/physrevb.53.13115.

(58) Stevie, F. A.; Donley, C. L. Introduction to X-Ray Photoelectron Spectroscopy. *J. Vac. Sci. Technol. A* **2020**, *38* (6), 063204. DOI: 10.1116/6.0000412.

(59) Powell, C. J. *NIST Electron Inelastic-Mean-Free-Path-Database*, Version 1.2.; Jablonski, A., Translator; National Institute of Standards and Technology: Gaithersburg, MD, 2010.

(60) Grey, L. H.; Nie, H.-Y.; Biesinger, M. C. Defining the Nature of Adventitious Carbon and Improving Its Merit as a Charge Correction Reference for XPS. *Appl. Surf. Sci.* **2024**, *653*, 159319. DOI: 10.1016/j.apsusc.2024.159319.

(61) Jain, U.; Lidiard, A. B. The Growth of Colloidal Centres in Irradiated Alkali Halides. *Phil. Mag.* **1977**, *35* (1), 245–259. DOI: 10.1080/14786437708235986.

(62) Levy, P. W.; Loman, J. M.; Swyler, K. J.; Dougherty, D. R. Recent Studies on Radiation Induced F-Center and Colloid Particle Formation in Synthetic NaCl and Natural Rock Salt. *Radiat. Eff.* **1983**, *72* (1–4), 303–308. DOI: 10.1080/00337578308218658.

(63) Ekmanis, Yu. A.; Pirogov, F. V.; Shvarts, K. K. The Process of Colloidal Centre Formation in Alkali Halide Crystals during Irradiation. *Radiat. Eff.* **1983**, *74* (1–4), 199–208. DOI: 10.1080/00337578308218413.

(64) Shi, H.; Chang, L.; Jia, R.; Eglitis, R. I. Ab Initio Calculations of the Transfer and Aggregation of *F* Centers in CaF_2. *J. Phys. Chem. C* **2012**, *116* (7), 4832–4839. DOI: 10.1021/jp208845w.

(65) Allouche, A. Water Dissociation on Defective Sites on the NaCl(100) Surface. A Quantum Ab Initio Study. *J. Phys. Chem. B* **1998**, *102* (50), 10223–10228. DOI: 10.1021/jp9814496.

(66) Abendroth, B.; Moebus, T.; Rentrop, S.; Strohmeyer, R.; Vinnichenko, M.; Weling, T.; Stöcker, H.; Meyer, D. C. Atomic Layer Deposition of TiO_2 from Tetrakis(Dimethylamino)Titanium and H_2O. *Thin Solid Films* **2013**, *545*, 176–182. DOI: 10.1016/j.tsf.2013.07.076.

(67) Petkov, V.; Holzhüter, G.; Tröge, U.; Gerber, T.; Himmel, B. Atomic-Scale Structure of Amorphous TiO_2 by Electron, X-Ray Diffraction and Reverse Monte Carlo Simulations. *J. Non-Cryst. Solids* **1998**, *231* (1–2), 17–30. DOI: 10.1016/S0022-3093(98)00418-9.

(68) Prasai, B.; Cai, B.; Underwood, M. K.; Lewis, J. P.; Drabold, D. A. Properties of Amorphous and Crystalline Titanium Dioxide from First Principles. *J. Mater. Sci.* **2012**, *47* (21), 7515–7521. DOI: 10.1007/s10853-012-6439-6.

(69) Yang, K.; Kachmar, A.; Wang, B.; Krishnan, N. M. A.; Balonis, M.; Sant, G.; Bauchy, M. New Insights into the Atomic Structure of Amorphous TiO_2 Using Tight-Binding Molecular Dynamics. *J. Chem. Phys.* **2018**, *149* (9), 094501. DOI: 10.1063/1.5042783.

(70) Diebold, U.; Madey, T. E. TiO_2 by XPS. *Surf. Sci. Spectra* **1996**, *4* (3), 227–231. DOI: 10.1116/1.1247794.

(71) Macleod, H. A. *Thin-Film Optical Filters*, 5th ed.; CRC Press: Boca Raton, 2017; p 696. DOI: 10.1201/b21960.

(72) Kresse, G.; Furthmüller, J. Efficient Iterative Schemes for *Ab Initio* Total-Energy Calculations Using a Plane-Wave Basis Set. *Phys. Rev. B* **1996**, *54* (16), 11169–11186. DOI: 10.1103/PhysRevB.54.11169.

(73) Perdew, J. P.; Burke, K.; Ernzerhof, M. Generalized Gradient Approximation Made Simple. *Phys. Rev. Lett.* **1996**, *77* (18), 3865–3868. DOI: 10.1103/PhysRevLett.77.3865.

(74) Moellmann, J.; Grimme, S. DFT-D3 Study of Some Molecular Crystals. *J. Phys. Chem. C* **2014**, *118* (14), 7615–7621. DOI: 10.1021/jp501237c.

(75) Grimme, S.; Ehrlich, S.; Goerigk, L. Effect of the Damping Function in Dispersion Corrected Density Functional Theory. *J. Comput. Chem.* **2011**, *32* (7), 1456–1465. DOI: 10.1002/jcc.21759.

(76) Parsons, G. N.; Clark, R. D. Area-Selective Deposition: Fundamentals, Applications, and Future Outlook. *Chem. Mater.* **2020**, *32* (12), 4920–4953. DOI: 10.1021/acs.chemmater.0c00722.

(77) Popov, A. I.; Kotomin, E. A.; Maier, J. Basic Properties of the F-Type Centers in Halides, Oxides and Perovskites. *Nucl. Instrum. Methods in Phys. Res., B* **2010**, *268* (19), 3084–3089. DOI: 10.1016/j.nimb.2010.05.053.

CHAPTER 4: PYHRMC: HYBRID REVERSE MONTE CARLO FOR ELECTRON TOTAL SCATTERING

4.1 Introduction

Knowledge of a material's structure is critical to understanding and predicting properties across applications. In crystalline materials, many insights about structure can be obtained by using Bragg diffraction to solve the exact structure of a periodic lattice. In contrast, amorphous materials lack the long-range order to produce Bragg diffraction. Other techniques, such as solid-state nuclear magnetic resonance or x-ray photoelectron spectroscopy, offer chemical insight into the local coordination environment around an atom but cannot provide information on the medium-range order (5 to 20 Å) of these coordination spheres. For this reason, structural characterization has proven to be a challenge for amorphous materials and they remain poorly understood relative to their crystalline counterparts.[1] This barrier to understanding amorphous and disordered structures poses limitations on the rational design of these materials for applications. Amorphous materials have already demonstrated superior properties in catalysis, ion transport, and flexibility.[2–4] Therefore, strategies for accurately characterizing amorphous structures are necessary for the discovery of structure-property relationships that can guide the development of next-generation amorphous materials for technologies.

Most commonly, amorphous structures are characterized by the pair distribution function (PDF). The PDF is a Fourier transform derived from the total scattering pattern of x-rays, neutrons, or electrons and provides insight into the prevalence and distributions of interatomic distances within the structure.[5,6] Due to their lack of long-range order, the PDF of amorphous materials lacks

peaks at large interatomic distances, but exhibits peaks at short distances that are distinctive to the first few coordination spheres surrounding an atom. Integration of the radial distribution function, a closely related form of the PDF, yields average coordination number. While informative, PDFs are still limited in the information that they can convey on the interconnectivity of these local environments.

To obtain an improved understanding of the atomistic structure, Reverse Monte Carlo (RMC) was first introduced in 1988 as an approach to solving a disordered structure from experimental scattering information.[7] The RMC method uses a Metropolis Markov chain Monte Carlo algorithm to stochastically perturb a structure while minimizing the difference between experimental and modeled PDFs.[8,9] This approach has been widely adopted to yield experimentally-derived atomistic models of disordered materials, which can be subsequently analyzed for further structural insights.[10,11] Additionally, because of its low computational cost, RMC is able to model systems on the order of thousands of atoms and produce distributions of coordination environments that are statistically robust.

However, RMC has also received criticism because there are typically a very large number of structures that produce the same PDF, resulting in an under-constrained problem that does not produce a unique solution.[12] To limit the unphysical configurations that it may produce as a solution, users typically impose additional structural constraints, such as minimum interatomic distances, bond angles, and coordination number.[13–15] While these constraints have demonstrated success, such constraints rely on the user's chemical intuition and prior understanding of the material to define the expected structural characteristics, biasing structures toward user-expected outcomes. Furthermore, the need for prior knowledge of the material's structure poses a challenge to modeling novel materials.

These limitations led to the development of Hybrid RMC (HRMC) by Opletal et al. in 2002.[16] In HRMC, an additional energy term is included in the cost function that is minimized over the simulation. This added term results in the simulation accepting steps that reduce the difference between experimental and modeled PDFs and that also lower the material's energy. This approach was demonstrated to be successful in mitigating the formation of unphysical three-membered rings that otherwise form in traditional RMC of disordered carbon.[16,17] Because structural energy is calculated from an interatomic potential, the need for prior understanding of the structure is also reduced.

Given increasing interest in nano-scale materials, applying these characterization techniques to extremely small and thin samples is also desirable. However, examining such small sample regions or quantities is difficult, particularly in 2D materials and thin films, because the experimental x-ray and neutron total scattering approaches that are conventionally used with HRMC software cannot sufficiently probe these samples. To characterize such materials, stronger interactions between the scattering source and atoms are necessary to obtain suitable signal-to-noise ratios. Electron scattering includes a Coulombic interaction that results in larger scattering cross sections than x-rays or neutrons, offering a solution to this challenge.[6] Highly focused scattering probes are also desirable for analyzing small spatial regions of the sample, which are accessible in standard TEMs and difficult to obtain for x-rays and neutrons outside of synchrotron sources. Thus, electron total scattering measurements can be used to acquire experimental information on a material's structure when other scattering sources are unsuitable.

Despite the advantages of electron total scattering and HRMC, existing software for such calculations face limitations. The original HRMC program includes only a small set of empirical potentials for energy calculations, making its applications limited to a select few systems.[18,19]

Additionally, it does not include electron scattering as an experimental constraint and is designed strictly for bulk materials, since sample/vacuum interfaces cannot be specified. Another popular program, RMCProfile, has recently adopted HRMC capabilities that allow users to supply empirical or machine-learned potentials and can model non-bulk structures but also does not support total electron scattering as a constraint.[20,21] In contrast, programs with electron total scattering analysis currently perform RMC but do not support HRMC calculations.[22,23] Many of these programs are also not open-source, reducing flexibility for the user. Therefore, a generalizable HRMC software for modeling amorphous thin materials with electron total scattering is necessary.

To address this need, we introduce pyHRMC. This package allows users to perform HRMC simulations of bulk and 2D/thin film systems with electron scattering as an experimentally-derived constraint. Like RMCProfile, pyHRMC interfaces with the Large-scale Atomic/Molecular Massively Parallel Simulator (LAMMPS) package to calculate structural energy, allowing the use of any LAMMPS-compatible interatomic potentials, including machine-learned potentials.[24,25] The integration of machine-learned (ML) potentials allows pyHRMC to model novel materials without existing empirical potentials and is the first package to do so in combination with using electron total scattering as a constraint. The code is written primarily in Python for user readability and heavily utilizes NumPy modules in C for speed-ups. Further speed-ups can be gained from the parallelizable architecture of the package, which allows users to sample candidate Monte Carlo moves in parallel to reduce computational time. Lastly, pyHRMC is open-source and available to the public.

4.2 Methods

4.2.1 The HRMC algorithm

Conceptually, the HRMC algorithm sits between RMC and standard Monte Carlo in its approach and is summarized in Figure 4.1. A Metropolis Markov chain Monte Carlo algorithm is used to perturb individual atoms and stochastically sample atomistic configurations. An initial structure is provided by the user at the beginning of the simulation, from which the simulation randomly chooses an atom from the structure and translates the atom along a random vector (typically, this vector length is on the Ångstrom scale). The new structure is then evaluated according to a cost function, which takes the following general form:

$$\chi^2_{\text{total}} = \chi^2_{\text{PDF}} + \chi^2_{\text{energy}} \quad (4\text{-}1).$$

Here, the total cost χ^2_{total} is the sum of costs from two constraints, the PDF residual χ^2_{PDF} and structural energy χ^2_{energy}.

In pyHRMC, χ^2_{PDF} is calculated as the squared difference between the calculated and the target PDFs, weighted by a term that affects the probability of accepting a step that worsens the cost function value. Following convention, pyHRMC compares PDFs by representing them as reduced pair distribution functions G(r):[20,22]

$$\chi^2_{\text{PDF}} = \sum_{i=1}^{n_{\text{bin}}} \frac{\left(G(r_i)_{\text{target}} - G(r_i)_{\text{calc}}\right)^2}{\sigma} \quad (4\text{-}2).$$

In this case, the squared difference between the experimental PDF $G(r)_{\text{target}}$ and calculated PDF $G(r)_{\text{calc}}$ is scaled by the experimental error σ and is summed over n_{bins}, the number of bins in $G(r)_{\text{target}}$. Because pyHRMC is designed for use with electron scattering data, the G(r) is assumed to be the electron PDF (ePDF) and defaults to using electron scattering cross sections.

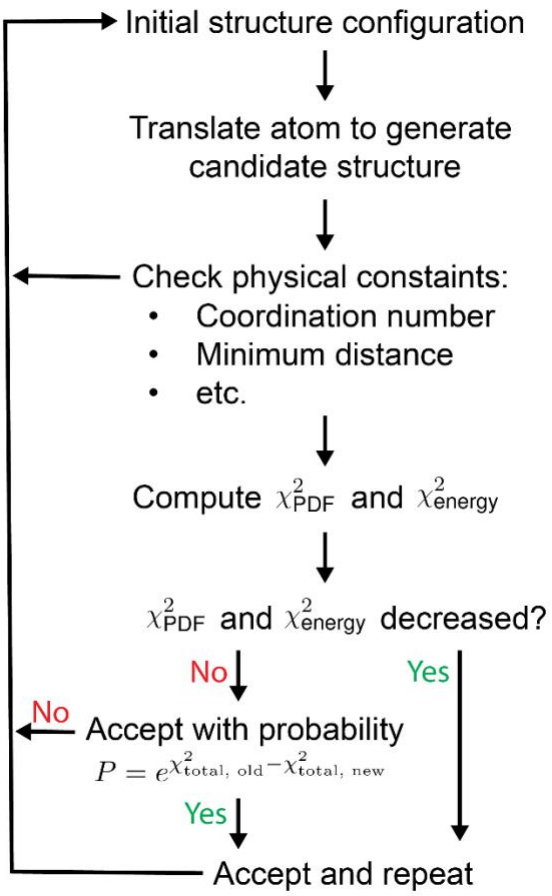


Figure 4.1 The HRMC algorithm.

The second term in the total cost function, χ^2_{energy}, deviates from the form in eqn. 4-2. Instead, it reflects a Boltzmann-type probability distribution that is scaled by temperature T:

$$\chi^2_{energy} = \frac{\Delta E}{k_B T} \quad (4\text{-}3),$$

where k_B is the Boltzmann constant and ΔE is the change in energy between the structure before and after the proposed step.

Using the total cost function, the algorithm automatically accepts the proposed Monte Carlo step if the sum of the new residual and energy cost values is less than the summed cost value

of the structure before the proposed step. Otherwise, the probability P of accepting the step is the following:

$$P = e^{\chi^2_{old} - \chi^2_{new}} \quad (4\text{-}4).$$

This process is then repeated by the algorithm by selecting a new atom, performing a translation, and evaluating the step. By iterating this loop, the algorithm preferentially accepts steps that decrease the PDF residual and structural energy, eventually converging at a structure that minimizes these cost functions.

One issue that can arise from this process is trapping a structure at a local minimum in the PDF residual or energy landscapes. To avoid this trapping, it was previously demonstrated that applying a quenching scheme to the weight terms σ and T allows greater freedom to explore the structural space and escape local minima while gradually decreasing the probability of accepting "worse" steps to ensure convergence at the end-stage of the simulation.[26] The following quenching scheme has been implemented in pyHRMC, as suggested by Opletal et al.:[18]

$$T_{n+1} = T_n \cdot q_T^n \quad (4\text{-}5),$$

$$\sigma_{n+1} = \sigma_n \cdot q_\sigma^n \quad (4\text{-}6).$$

Here, n is the number of steps (in millions) and q is a quenching parameter between zero and one. Because HRMC is performed over many steps and gradual quenching is necessary for proper convergence, q is typically a value just below 1, as demonstrated in the example in section 4.3.

4.2.2 Implementation

4.2.2.1 Organization of pyHRMC

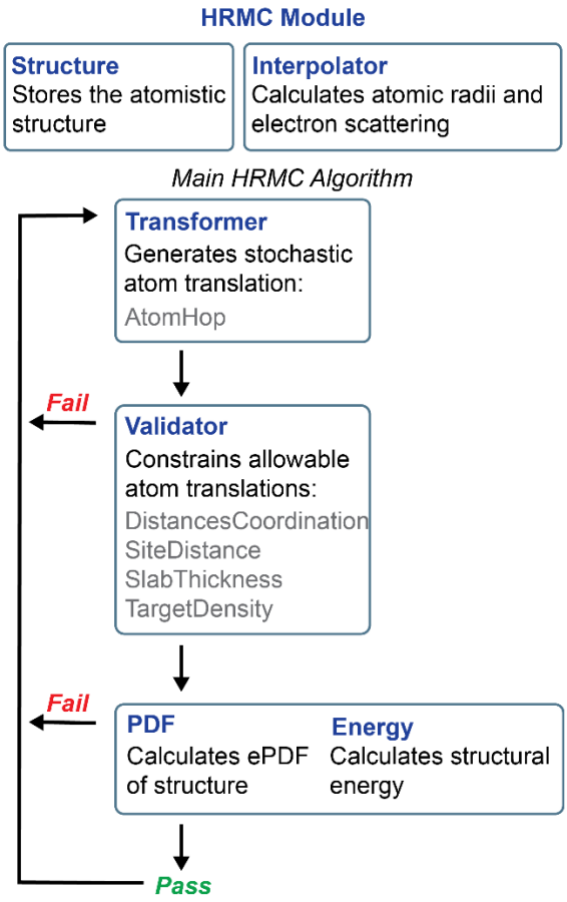


Figure 4.2 The organization of modules available in pyHRMC. The HRMC module is responsible for executing the algorithm by handling and calling other modules. The Structure and Interpolator modules are responsible for calculating and storing information about the structure, while the remaining modules are used to execute the HRMC algorithm.

The pyHRMC package consists of several key modules that house functions for different parts of the HRMC algorithm, which are managed and called by the central HRMC module. The organization of how pyHRMC utilizes the various modules is shown in Figure 4.2. Information about the structure is stored as a Structure object, which is shared with and transformed by other

modules. To enable modeling of the ultrathin and 2D materials that are commonly investigated with electron scattering, pyHRMC is compatible with bulk cells or slabs that include vacuum spaces above and below the structure. The Interpolator module provides an automated method of calculating ionic radii and scattering cross sections partially charged species, which we plan to fully integrate in the future for highly accurate scattering calculations. During the HRMC loop, the Transformer module takes in a structure, performs a Monte Carlo step, and returns this new structure with a translated atom. This proposed structure is checked against the physical constraints in the Validator module, experimental constraint in the PDF module, and the energy constraint in the Energy module. In this section, the implementation of these constraint modules is discussed in greater detail.

4.2.2.2 Experimental ePDF constraint

In pyHRMC, the PDF is assumed to be calculated from electron scattering, i.e., the electron pair distribution function (ePDF). This distinction is critical because the scattering cross-sections depend on the radiation source (electrons, x-rays, or neutrons). Although the use of electron scattering cross-sections is the default choice for pyHRMC, the user can manually override this option to use the software for x-rays or neutrons.

Because the language surrounding the PDF and its relatives has not been unified, we define the ePDF as the reduced pair distribution function G(r), represented as following:

$$G(r) = 4\pi r\rho_0(g(r) - 1) \quad (4\text{-}7).$$

In this equation, r is the radius, $\rho_0$is the number density, and g(r) is the pair distribution function, also expressed as:

$$g(r) = \frac{\rho(r)}{\rho_0} \quad (4\text{-}8),$$

where $\rho(r)$ is another function called the atom-number density function. For a full discussion of the PDF and all of its related forms, we refer the reader to more comprehensive resources.[5]

The total scattering cross sections (TCS) are used to calculate the electron scattering intensity from each type of atom in the structure. Small improvements in accuracy can be gained from accounting for partial charges. The scattering cross sections of charged atoms changes greatly at extremely small scattering angles, most of which are often blocked by a Faraday cup or beam blocker.[27,28] If some of these small angles are included in the scattering data, however, the scattering cross sections will be different between neutral and charged species. The Interpolator module in pyHRMC automatically calculates the ionic radius and TCS of a partially charged species by interpolating from parameterized oxidation states.[27] Generalizable, fast, and accurate methods of determining the partial charges for a material are currently limited. Although methods of charge partitioning, like Bader analysis, are fast, obtaining charge densities of the 1000s of atoms used in HRMC calculations is prohibitively expensive.[29] Therefore, pyHRMC defaults to parameterized forms of neutral atom TCS.[30] If desired charges are known, the user may employ the Interpolator module by listing the appropriate charges and minimum scattering angle.

An additional correction is needed for the geometry of the sample. TEM samples are necessarily thin to permit electron transmission, and the presence of sample/vacuum boundaries will alter the PDF for atoms near the sample's surface. pyHRMC allows the user to specify whether the sample should be treated as a slab or bulk geometry. When the structure is a slab, the calculated ePDF is modified to include a geometrical correction. We employ density and inter-sheet correlation correction terms introduced by Zhang et al.[31]

$$G(r) = 4\pi r \rho_0 \left(\frac{\rho_0^{RMC}}{\rho_0} g(r) + U(r) - 1 \right) \quad (4\text{-}9).$$

In the modified ePDF equation above, the density is corrected by the $\frac{\rho_0^{RMC}}{\rho_0}$ pre-factor. The inter-sheet correlation correction U(r) takes the form for nanosheets as follows:

$$U(r) = \begin{cases} \frac{r}{2d} & (0 < r < d) \\ 1 - \frac{d}{2r} & (r \geq d) \end{cases} \quad (4\text{-}10).$$

where d is the thickness of the slab.

The final consideration for the experimental ePDF constraint is the cell size. To compare the PDF of a candidate structure to an experimental ePDF, the interatomic distances within the candidate structure must be measured. For an accurate comparison, a full count of the interatomic distances must be made out to the largest radius used in the experimental ePDF. In the trial structure, double-counting of atoms due to periodic boundaries should be avoided and can be achieved by using a structure cell that is at least twice the maximum PDF radius. If a slab structure is being used, a vacuum length of twice the radius will prevent accidental counting between the top and bottom surfaces.

4.2.2.3 Structural energy constraint

The structural energy constraint minimizes energy to reduce the formation of unphysical atomic configurations. To allow flexibility in the potentials that a user may employ, pyHRMC interfaces with LAMMPS and can calculate energies from any potential that is compatible with LAMMPS.[24] In section 4.3, we demonstrate a key advantage of this flexibility: machine-learned interatomic potentials (MLIPs) may be used to provide DFT-like accuracy with high throughput. This interfacing approach has been previously employed by RMCProfile to add an HRMC functionality, but pyHRMC remains the first package to integrate MLIP flexibility with electron total scattering fitting.[21]

A simple and standard LAMMPS input script is used to set up the energy constraint, which pyHRMC feeds to LAMMPS through a call to the Energy module. The script should contain information on the structure cell and potential but does not require commands to perform molecular dynamics because the module is only used to perform static energy calculations. Therefore, minimal knowledge of LAMMPS scripting is required to configure the energy constraint.

4.2.2.4 Physical constraints

Despite the advantages of using an energy constraint to limit unphysical configurations, previous attempts have found that physical constraints still provide useful improvements to modeling accuracy.[32] To allow further control over the permissible movements in a simulation, physical constraints have been implemented in the Validator module and are described here.

Certain constraints are most useful for traditional RMC simulations, which require a greater set of physical constraints and can be performed in pyHRMC by electing to not use the energy constraint. The TargetDensity constraint compares the structure density to a user-defined value to avoid density drops in structure cells with vacuum. Any vacuum region above or below the structure is excluded in the density calculation. The SlabThickness constraint performs a similar function by enforcing a maximum thickness, such that a proposed Monte Carlo step that translates an atom beyond this maximum thickness is automatically rejected.

Other constraints may still aid HRMC simulations. The DistancesCoordination validator includes two useful constraints that are enforced in sequence: 1) minimum pairwise interatomic distances between species and 2) the allowed range of coordination numbers for each pairwise combination of species. The coordination number ranges are separated into bulk and surface atom constraints, to allow atoms at the surface to exist in coordination environments that may differ

from the bulk. If a single minimum interatomic distance across all pairwise distances is appropriate and coordination number does not need to be constrained, users may elect to use the SiteDistance constraint for faster computation.

One limitation of the DistancesCoordination validator lies in the computational cost of determining neighbor sites. To avoid large costs, pyHRMC checks the coordination of atoms within a set radius of the moved atom, meaning that near neighbors are not affected by this limitation. However, atoms outside of this radius may experience small changes in neighbor weighting, leading to changed coordination numbers according to the CrystalNN algorithm that we employ to determine coordination.[33]

4.2.2.5 Parallelization

A major rate-limiting part of the HRMC algorithm is generating accepted steps. As a calculation progresses, the acceptance rate of candidate atomic translations drops drastically and the time between accepted steps increases. To reduce this effect and speed up the calculation time, pyHRMC features a heavily parallelized architecture. This parallelization is performed with the multiprocessing package in Python, which uses multiple processors to simultaneously perform tasks. If multiple processors are available, users are encouraged to use this feature for significant speed-ups. However, to avoid compatibility issues with MPI parallelization in LAMMPS, LAMMPS must be built as a serial executable.

When permitted, the code will parallelize the entire task of generating a step, checking against validator constraints, and determining the acceptance probability of the step. Each parallel task will return a new Structure object if the step is accepted. In pyHRMC, each iteration of the HRMC loop produces a batch of accepted singular steps. Each batch will contain up to as many steps as there are utilized processors, although the number of accepted steps is typically below this

upper limit and decreases as the calculation continues. Once a batch is generated, an additional check is performed to ensure that the composite structure of these individual steps still meets the constraints.

4.2.3 Usage

To perform an HRMC simulation, pyHRMC is used entirely through a single Python script, which calls upon several supplementary files that include an initial structure POSCAR file, an experimental data file, and any additional interatomic potential files. The Python script should be tailored with all of the user-defined parameters for a simulation and requires two commands. First, the user must create an HRMC class object with the initial values of σ and T and their quenching rates q_σ and q_T. Next, the remaining configurational details are defined by calling the *run_rmc()* method, which starts a simulation. An example of a script for HRMC on amorphous alumina is included in the documentation.

4.3 Demonstration with amorphous Al_2O_3

To demonstrate the validity of our implementation and illustrate the insights that our method allows, we use an amorphous thin film of Al_2O_3 as an example. Amorphous alumina has an array of technological applications, including in Josephson junctions, batteries, and catalysis.[34–36] Such freestanding thin films have recently been prepared experimentally with atomic layer deposition,[37] but characterizing their structure remains challenging with current methods. Thus, this example represents a class of materials that stands to benefit greatly from our software.

4.3.1 MLIP training and molecular dynamics

To train a MLIP, we utilized the FLARE package.[25] Training data was generated using ab-initio molecular dynamics with the Vienna ab-initio simulation package (VASP).[38] For this training, a slab structure of Al_2O_3 containing 160 atoms was utilized. The slab had a thickness of 20 Å and

in-plane dimensions of 11 and 9 Å. An additional 13 Å was used as vacuum. Spin-polarized DFT calculations were performed in VASP with the r^{2}SCAN functional using an energy cutoff of 480 eV and a 1×1×1 *k*-point grid.[39] To improve electronic convergence, we used the ALL algorithm, which simultaneously updates bands and orbitals. Convergence was achieved for an energy change below 10^{-4} eV. The MLIP was built in FLARE using a Chebyshev basis, quadratic cut-off function, and 5.0 Å radius. The B2 descriptor with 8 radial basis harmonics and 4 angular momentum harmonics was selected. The normalized dot product kernel with sigma variance prefactor of 2.0 and power of 2.0 was employed. New training data was acquired when the maximum uncertainty in atomic force was above 0.02 eV/Å.

With the trained model, molecular dynamics (MD) was then performed with the LAMMPS package to create a target "ground truth" structure.[24] An initial α-Al_2O_3 slab cell of 1920 atoms (768 Al atoms and 1152 O atoms) was prepared for MD. The cell was expanded to have a density of 2.9 g/cm^3, which is comparable to the experimental densities of amorphous alumina.[40] Periodic boundary conditions were used and vacuum space was inserted above and below the cell to obtain a thin film configuration. The NVT ensemble with a 5 fs timestep was used. The cell was initially heated to 2000 K and equilibrated for 5 ns to remove memory effects. The cell was subsequently cooled to 300 K over 7 ns (a cooling rate of 0.24 K/ps). Energy minimization was then performed on the structure and the final configuration was used.

4.3.2 Comparing Al_2O_3 models from RMC and HRMC

To determine the accuracy of HRMC in comparison to RMC, we modeled Al_2O_3 to fit a known amorphous structure. This known atomistic structure, henceforth referred to as the ground-truth, was prepared via MD with our MLIP (see section 4.3.1). The MD produced a 5.4 nm-thick slab of amorphous Al_2O_3, from which an ePDF was extracted. The initial peak of the ground-truth

ePDF is at 1.79 Å, consistent with the Al-O interatomic distance in amorphous alumina, while the two overlapping peaks that make up the second coordination shell (3.05 Å and 3.30 Å) are consistent with O-O and Al-Al interatomic distances, respectively.[41,42] Additionally, the distribution of Al coordination number agrees closely with solid-state NMR of amorphous alumina thin films.[43] Based on these similarities to previously reported amorphous Al_2O_3, we determined that the structure was appropriately realistic for validating our Python package. Thus, the ePDF of this ground-truth structure was used as the target data to which the RMC and HRMC calculations were fit.

Both calculations were performed using pyHRMC. As a starting structure configuration, we used the same structure of expanded α-Al_2O_3 that was used to initiate the MD in section 4.3.1. By using the same initial configuration, we eliminate differences in the final structures that may arise from the starting arrangement of atoms. To perform RMC, we used pyHRMC without an energy constraint, resulting in a single cost function that is determined solely by the ePDF. Because RMC typically maintains a constant experimental error σ parameter throughout the calculation, a set value of $\sigma = 0.01$ was applied. Although we attempted simulations with greater values of σ, these values did not sufficiently constrain the calculation to converge at a low ePDF residual. For HRMC, slow quenching was employed. The calculation was performed with initially large values of T (2000 K) and σ (0.5), resulting in low weighting of the structural energy and ePDF residual constraints. Following the quenching schemes in eqns. 4-5 and 4-6, both parameters were reduced until T reached room temperature (T = 300 K, quench rate = 0.9995), at which point T and σ were held constant until convergence.

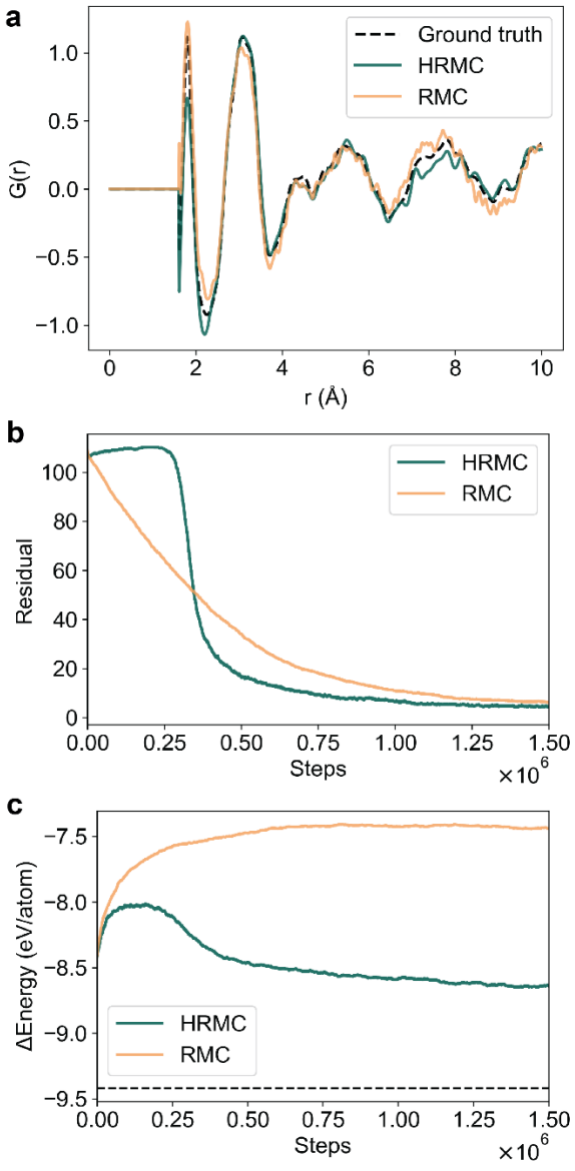


Figure 4.3 (a) Pair distribution function (PDF) of the ground-truth MD structure (black, dotted line) compared against the HRMC (green) and RMC (orange) structure PDFs. (b) The PDF residual between the ground-truth and fitted structures over the course of the calculations. (c) The change in potential energy per atom during the calculation for HRMC and RMC methods. The dashed black line indicates the energy of the ground-truth structure.

The evolution of the ePDF residual and structural energies of these calculations are shown in Figure 4.3. After 1.5 million steps each, the RMC and HRMC calculations successfully minimized the ePDF residual to 6.22 and 4.24, respectively. These residuals are consistent with typical values of a converged HRMC calculation, which are generally ≤ 10.0, indicating that our calculations produced ePDFs that closely fit the ground-truth (Figure 4.3a).[17,44] Interestingly, in the HRMC calculation, the residual remained approximately constant until ~250k steps, at which point the rate of improvement fell significantly above the RMC calculation (Figure 4.3b). The energy curves followed a similar pattern, increasing rapidly at the beginning but quickly plateauing until ~250k steps, when the energy began decreasing. This initial behavior was not observed in the RMC calculations, which showed a constantly decreasing residual and correspondingly increasing energy throughout the calculation. We suggest that this difference emerges from the early regime of HRMC's exponential quenching scheme, during which constraints are applied with a low weight as the parameters are gradually decreased. During this early stage of the calculation, the structure should be able to more effectively explore transition states and escape initial coordination environments, while also being constrained enough such that the atomic movements are not fully stochastic and prevent disarrangement into highly unrealistic configurations.

Additionally, following the different convergence patterns of the calculations, the final structures yield a significant difference in the structural energy between modeling methods. HRMC yielded a structure with 1.17 eV/atom less than RMC, despite comparable PDF residuals (Figure 4.3c). These energies indicate a marked improvement to the stability of the calculated structures compared to RMC, while also demonstrating the key critique of RMC algorithms: a similar PDF may be produced from an infinite number of structures, meaning that results are non-unique. Therefore, constraints are necessary to limit the possible results to physically realistic

representations of the experimental data, highlighting the importance of including the energy term in HRMC. However, we note that the structural energy of the HRMC structure remains 0.75 eV/atom above the ground-truth. We attribute this difference in energy to remaining differences in between the structures, which are illustrated in Figure 4.4. Thus, while the energy term is useful for improving the calculation, the amorphous model retains some amount of unstable local configurations that yield overall high energies and should therefore not be used to determine the energy of the target structure. Despite this limitation, these results show that the HRMC approach, as implemented in pyHRMC, is able to increase the productivity of the Monte Carlo fitting process by minimizing forays into local minima of the energy and PDF residual landscape, producing better outcomes along these metrics.

To further understand the structural differences that give rise to the large energy difference, we examined the distributions of coordination numbers in the structures. In the ground-truth bulk, most Al atoms were four-coordinate (^{4}Al) or five-coordinate (^{5}Al) (47.7% and 48.9%, respectively), with a small amount of six-coordinate Al (^{6}Al) (3.4%). Both calculated structures roughly followed this trend, consisting mostly of ^{4}Al and ^{5}Al with some ^{6}Al (Figure 4.4a). However, the fraction of each coordination number in the HRMC structure more closely resembles the ground-truth than the RMC results. This relation holds true for the bulk O atoms as well, with the HRMC coordination number distributions more similar to the ground-truth distribution of ^{2}O (2.0%), ^{3}O (91.0%), and ^{4}O (7.0%). The greatest absolute error in bulk coordination fraction for both structures is the fraction of ^{3}O, which is 8.3% lower in HRMC and 25% lower in RMC (Figure 4.4b). These values indicate that in bulk, HRMC offers a clear improvement over RMC even in areas of greatest error.

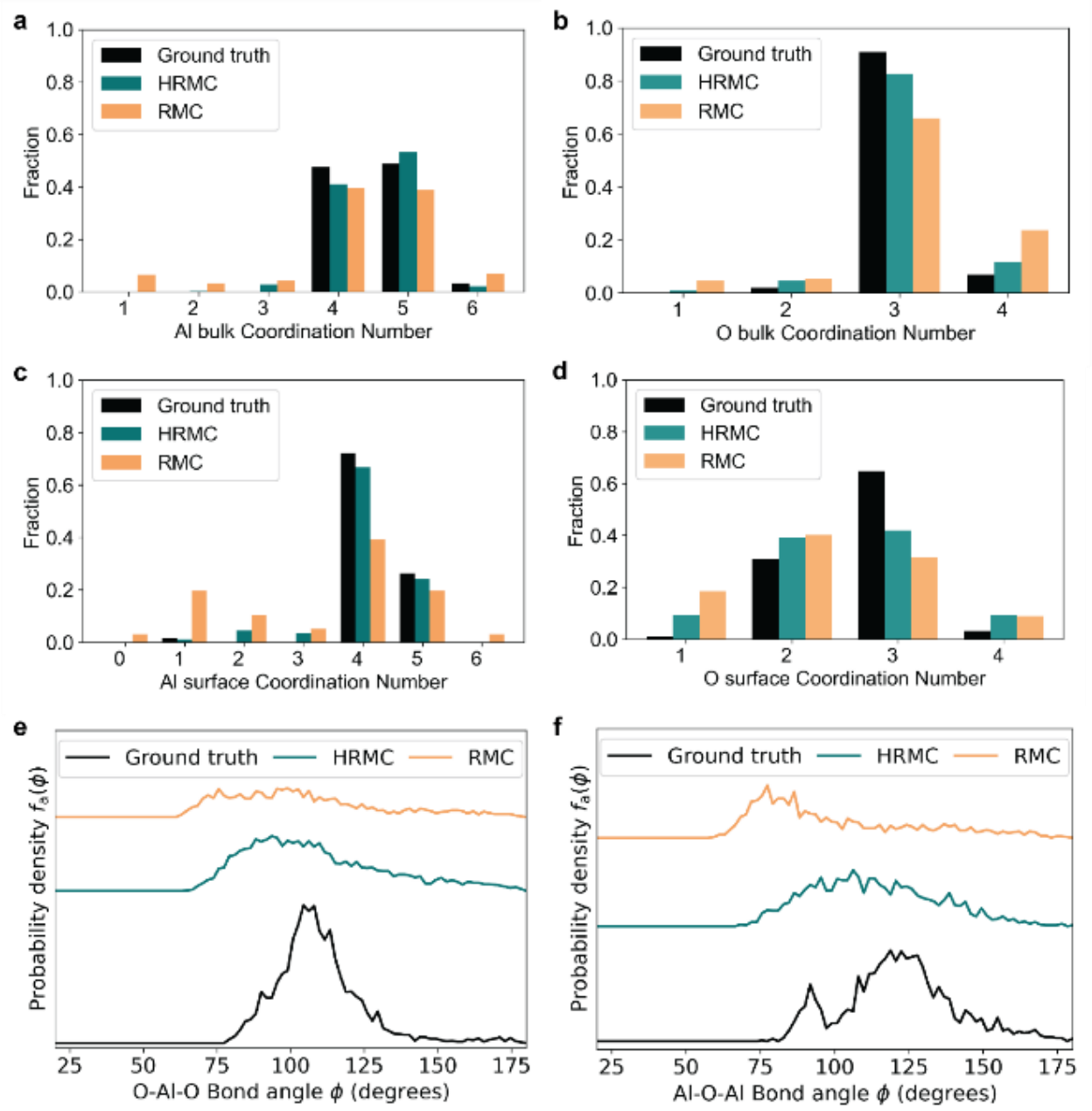


Figure 4.4 (a-d) The coordination number distributions of (a) Al and (b) O in bulk and (c) Al and (d) O at the surface (≤ 3 Å from the top and bottom of the structure slab). (e-f) The bond-angle ADFs of (e) O-Al-O and (f) Al-O-Al. Bonds were assigned with TopoTools in VMD and the ADF was calculated by OVITO.[45–47]

Another important difference between the HRMC and RMC structures is the fraction of atoms with a coordination number outside of the range observed in the ground-truth structure. To some extent, both structures produced coordination numbers beyond the ground-truth range. These undesirable coordination fractions are especially noticeable at the surface, where the calculated structures err towards lower coordination numbers than the ground-truth (Figure 4.4c,d). This error is challenging to eliminate entirely, even with the appropriate coordination constraints, as discussed in section 4.2.2.4. Despite this difficulty, the results in Figure 4.4 show that HRMC produced significantly fewer sites outside the target coordination range than RMC, including surface sites. These results suggest that the energy term is valuable for limiting the formation of unrealistic coordination numbers, not just the ring size discussed in previous reports.[16,17] Furthermore, sites of unrealistic coordination are likely high in energy. The prevalence of such sites in the RMC structure, particularly at the surface, may explain the observed energy difference between the calculated structures. These findings provide additional support for the improved accuracy of HRMC and confirms the validity of the pyHRMC implementation with electron scattering.

The coordination environments in each structure are further examined in the bond angle distribution functions (ADF) (Figure 4.4e,f). In the O-Al-O ADF, the calculated structures have wider distributions than the ground-truth, consistent with the wider range of Al coordination numbers observed in Figure 4.4a-d. However, the distribution from HRMC is narrower than the distribution from RMC, forming a taller peak at approximately 100°. This effect is also pronounced in the Al-O-Al ADF. The ground-truth structure features two peaks around 90° and 120°, but the ADF of the HRMC structure shows a single broad peak over these angles. While these results suggest that distinguishing close individual peaks in an ADF is difficult through HRMC modeling,

the range of observed bond angles in both ADFs agree closely with the ground-truth. The same cannot be said for RMC, which produces notably smaller bond angles in the Al-O-Al ADF. These bond angles are consistent with the over-coordination of bulk O observed in the RMC coordination number distributions, since a greater number of atoms surrounding an O atom should result in smaller bond angles. These data are again consistent with the advantages of HRMC and successful modeling through pyHRMC.

In summary, HRMC successfully fit a structure to the ground-truth ePDF while producing a significantly lower structural energy than RMC. The structural differences that cause this difference in energy has been characterized by the coordination distribution and ADFs, which corroborate that HRMC more closely resembles the ground-truth local atomistic structure. Here, an MD-simulated structure was used as the target structure. However, similarly thin amorphous Al_2O_3, a historically challenging material to characterize, may be experimentally measured with scattering and modeled in pyHRMC to obtain an experimentally-derived structure. This analysis is accomplished by using total electron scattering, in contrast to x-ray or neutron scattering. These results indicate the advantages offered by using pyHRMC for solving the 3D structure of amorphous nanomaterials from electron scattering data.

4.4 Conclusions

Here, we have described pyHRMC, a new Python package for the HRMC modeling of amorphous structures from total electron scattering. By allowing the use of total electron scattering, pyHRMC offers an avenue to obtain experimentally-derived structures from ultrathin and nanoscale materials that have historically been challenging targets of characterization. The package provides a high degree of flexibility for the user, including structure geometry, interatomic potentials, and constraints that the user may apply to their calculation. The advantages of HRMC

over a traditional RMC approach have been demonstrated with an amorphous Al_2O_3 example. In our demonstration, HRMC more closely followed the coordination number and bond angle distributions of the ground-truth structure while also having a lower structural energy by 1.17 eV/atom. These results illustrate the value of modeling amorphous materials via pyHRMC.

This new capability is particularly promising for materials with extremely light elements. Because electron scattering cross-sections scale roughly with Z^2, light atoms such as H and Li cannot be adequately detected with electron scattering.[6] Although this limitation is true across techniques that rely on electron scattering, including recent advanced techniques such as atomic electron tomography (AET), HRMC is uniquely well-suited to address this issue.[48] Similar to AET, the experimental scattering data for HRMC has only a small contribution from light atoms. However, an accurate forcefield allows the method to constrain the positions of light atoms. Thus, the combination of experimental and computational methods yields statistically realistic structural models. For this reason, we expect that pyHRMC will be useful in providing insights into the structural features of challenging amorphous targets.

REFERENCES

(1) Kang, J.; Yang, X.; Hu, Q.; Cai, Z.; Liu, L.-M.; Guo, L. Recent Progress of Amorphous Nanomaterials. *Chem. Rev.* **2023**, *123* (13), 8859–8941. https://doi.org/10.1021/acs.chemrev.3c00229.

(2) Goldsmith, B. R.; Peters, B.; Johnson, J. K.; Gates, B. C.; Scott, S. L. Beyond Ordered Materials: Understanding Catalytic Sites on Amorphous Solids. *ACS Catal.* **2017**, *7* (11), 7543–7557. https://doi.org/10.1021/acscatal.7b01767.

(3) Bates, J. B.; Dudney, N. J.; Gruzalski, G. R.; Zuhr, R. A.; Choudhury, A.; Luck, C. F.; Robertson, J. D. Fabrication and Characterization of Amorphous Lithium Electrolyte Thin Films and Rechargeable Thin-Film Batteries. *J. Power Sources* **1993**, *43* (1–3), 103–110. https://doi.org/10.1016/0378-7753(93)80106-Y.

(4) Kang, J.; Yang, X.; Hu, Q.; Cai, Z.; Liu, L.-M.; Guo, L. Recent Progress of Amorphous Nanomaterials. *Chem. Rev.* **2023**, *123* (13), 8859–8941. https://doi.org/10.1021/acs.chemrev.3c00229.

(5) Egami, T.; Billinge, S. J. L. *Underneath the Bragg Peaks: Structural Analysis of Complex Materials*, 2nd edition.; Pergamon materials series; Elsevier: Amsterdam, 2012.

(6) Ehrhardt, K. M.; Radomsky, R. C.; Warren, S. C. Quantifying the Local Structure of Nanocrystals, Glasses, and Interfaces Using TEM-Based Diffraction. *Chem. Mater.* **2021**, *33* (23), 8990–9011. https://doi.org/10.1021/acs.chemmater.1c03017.

(7) McGreevy, R. L. Reverse Monte Carlo Modelling. *J. Phys.: Condens. Matter* **2001**, *13* (46), R877–R913. https://doi.org/10.1088/0953-8984/13/46/201.

(8) Metropolis, N.; Rosenbluth, A. W.; Rosenbluth, M. N.; Teller, A. H.; Teller, E. Equation of State Calculations by Fast Computing Machines. *J. Chem. Phys.* **1953**, *21* (6), 1087–1092. https://doi.org/10.1063/1.1699114.

(9) McGreevy, R. L. Reverse Monte Carlo Modelling. *J. Phys.: Condens. Matter* **2001**, *13* (46), R877–R913. https://doi.org/10.1088/0953-8984/13/46/201.

(10) Paranamana, N. C.; Gettler, R.; Koenig, H.; Montgomery-Smith, S.; He, X.; Young, M. J. Measuring Local Atomic Structure Variations through the Depth of Ultrathin (<20 nm) ALD Aluminum Oxide: Implications for Lithium-Ion Batteries. *ACS Appl. Nano Mater.* **2022**, *5* (9), 12582–12591. https://doi.org/10.1021/acsanm.2c02312.

(11) Hibble, S. J.; Wood, G. B. Modeling the Structure of Amorphous MoS_3: A Neutron Diffraction and Reverse Monte Carlo Study. *J. Am. Chem. Soc.* **2004**, *126* (3), 959–965. https://doi.org/10.1021/ja037666o.

(12) McGreevy, R. L. RMC: Progress, Problems and Prospects. *Nucl. Instrum. Methods Phys. Res. Sect. A* **1995**, *354* (1), 1–16. https://doi.org/10.1016/0168-9002(94)00926-0.

(13) Keen, D. A.; McGreevy, R. L. Structural Modelling of Glasses Using Reverse Monte Carlo Simulation. *Nature* **1990**, *344* (6265), 423–425. https://doi.org/10.1038/344423a0.

(14) Chen, Z.; Zimmerli, N. K.; Zubair, M.; Yakimov, A. V.; Björgvinsdóttir, S.; Alaniva, N.; Willinger, E.; Barnes, A. B.; Bedford, N. M.; Copéret, C.; Florian, P.; Abdala, P. M.; Fedorov, A.; Müller, C. R. Nature of GaO_x Shells Grown on Silica by Atomic Layer Deposition. *Chem. Mater.* **2023**, *35* (18), 7475–7490. https://doi.org/10.1021/acs.chemmater.3c00923.

(15) Biswas, P.; Atta-Fynn, R.; Drabold, D. A. Reverse Monte Carlo Modeling of Amorphous Silicon. *Phys. Rev. B* **2004**, *69* (19), 195207. https://doi.org/10.1103/PhysRevB.69.195207.

(16) Opletal, G.; Petersen, T.; O'Malley, B.; Snook, I.; McCulloch, D. G.; Marks, N. A.; Yarovsky, I. Hybrid Approach for Generating Realistic Amorphous Carbon Structure Using Metropolis and Reverse Monte Carlo. *Mol. Simul.* **2002**, *28* (10–11), 927–938. https://doi.org/10.1080/089270204000002584.

(17) Jain, S. K.; Pellenq, R. J.-M.; Pikunic, J. P.; Gubbins, K. E. Molecular Modeling of Porous Carbons Using the Hybrid Reverse Monte Carlo Method. *Langmuir* **2006**, *22* (24), 9942–9948. https://doi.org/10.1021/la053402z.

(18) Opletal, G.; Petersen, T. C.; O'Malley, B.; Snook, I. K.; McCulloch, D. G.; Yarovsky, I. HRMC: Hybrid Reverse Monte Carlo Method with Silicon and Carbon Potentials. *Comput. Phys. Commun.* **2008**, *178* (10), 777–787. https://doi.org/10.1016/j.cpc.2007.12.007.

(19) Opletal, G.; Petersen, T. C.; Russo, S. P. HRMC_2.1: Hybrid Reverse Monte Carlo Method with Silicon, Carbon, Germanium and Silicon Carbide Potentials. *Comput. Phys. Commun.* **2014**, *185* (6), 1854–1855. https://doi.org/10.1016/j.cpc.2014.02.025.

(20) Sławiński, W. A.; Kerr, C. J.; Zhang, Y.; Playford, H. Y.; Dove, M. T.; Phillips, A. E.; Tucker, M. G. *RMCProfile7*: Reverse Monte Carlo for Multiphase Systems. *J. Appl. Crystallogr.* **2024**, *57* (4), 1251–1262. https://doi.org/10.1107/S1600576724004175.

(21) Cuillier, P.; Tucker, M. G.; Zhang, Y. Integrating Machine Learning Interatomic Potentials with Hybrid Reverse Monte Carlo Structure Refinements in *RMCProfile*. *J. Appl. Crystallogr.* **2024**, *57* (6), 1780–1788. https://doi.org/10.1107/S1600576724009282.

(22) Aoun, B. Fullrmc, a Rigid Body Reverse Monte Carlo Modeling Package Enabled with Machine Learning and Artificial Intelligence. *J. Comput. Chem.* **2016**, *37* (12), 1102–1111. https://doi.org/10.1002/jcc.24304.

(23) Gereben, O.; Pusztai, L. RMC_POT: A Computer Code for Reverse Monte Carlo Modeling the Structure of Disordered Systems Containing Molecules of Arbitrary Complexity. *J. Comput. Chem.* **2012**, *33* (29), 2285–2291. https://doi.org/10.1002/jcc.23058.

(24) Thompson, A. P.; Aktulga, H. M.; Berger, R.; Bolintineanu, D. S.; Brown, W. M.; Crozier, P. S.; In 'T Veld, P. J.; Kohlmeyer, A.; Moore, S. G.; Nguyen, T. D.; Shan, R.; Stevens, M. J.; Tranchida, J.; Trott, C.; Plimpton, S. J. LAMMPS - a Flexible Simulation Tool for Particle-

Based Materials Modeling at the Atomic, Meso, and Continuum Scales. *Comput. Phys. Commun.* **2022**, *271*, 108171. https://doi.org/10.1016/j.cpc.2021.108171.

(25) Vandermause, J.; Torrisi, S. B.; Batzner, S.; Xie, Y.; Sun, L.; Kolpak, A. M.; Kozinsky, B. On-the-Fly Active Learning of Interpretable Bayesian Force Fields for Atomistic Rare Events. *npj Comput. Mater.* **2020**, *6* (1), 20. https://doi.org/10.1038/s41524-020-0283-z.

(26) Farmahini, A. H.; Bhatia, S. K. Hybrid Reverse Monte Carlo Simulation of Amorphous Carbon: Distinguishing between Competing Structures Obtained Using Different Modeling Protocols. *Carbon* **2015**, *83*, 53–70. https://doi.org/10.1016/j.carbon.2014.11.013.

(27) Peng, L.-M. Electron Scattering Factors of Ions and Their Parameterization. *Acta Crystallogr. A* **1998**, *54* (4), 481–485.

(28) Bick, T.; Dominiak, P. M.; Wendler, P. Exploiting the Full Potential of Cryo-EM Maps. *BBA Advances* **2024**, *5*, 100113. https://doi.org/10.1016/j.bbadva.2024.100113.

(29) Henkelman, G.; Arnaldsson, A.; Jónsson, H. A Fast and Robust Algorithm for Bader Decomposition of Charge Density. *Comput. Mater. Sci.* **2006**, *36* (3), 354–360. https://doi.org/10.1016/j.commatsci.2005.04.010.

(30) Peng, L.-M. Electron Atomic Scattering Factors and Scattering Potentials of Crystals. *Micron* **1999**, *30* (6), 625–648. https://doi.org/10.1016/S0968-4328(99)00033-5.

(31) Zhang, Y.; McDonnell, M.; Liu, W.; Tucker, M. G. Reverse Monte Carlo Modeling for Low-Dimensional Systems. *J. Appl. Crystallogr.* **2019**, *52* (5), 1035–1042. https://doi.org/10.1107/S160057671901080X.

(32) Opletal, G.; Petersen, T. C.; Snook, I. K.; Russo, S. P. HRMC_2.0: Hybrid Reverse Monte Carlo Method with Silicon, Carbon and Germanium Potentials. *Comput. Phys. Commun.* **2013**, *184* (8), 1946–1957. https://doi.org/10.1016/j.cpc.2013.03.004.

(33) Pan, H.; Ganose, A. M.; Horton, M.; Aykol, M.; Persson, K. A.; Zimmermann, N. E. R.; Jain, A. Benchmarking Coordination Number Prediction Algorithms on Inorganic Crystal Structures. *Inorg. Chem.* **2021**, *60* (3), 1590–1603. https://doi.org/10.1021/acs.inorgchem.0c02996.

(34) Wilt, J.; Gong, Y.; Gong, M.; Su, F.; Xu, H.; Sakidja, R.; Elliot, A.; Lu, R.; Zhao, S.; Han, S.; Wu, J. Z. Atomically Thin Al_2O_3 Films for Tunnel Junctions. *Phys. Rev. Applied* **2017**, *7* (6), 064022. https://doi.org/10.1103/PhysRevApplied.7.064022.

(35) Hao, S.; Wolverton, C. Lithium Transport in Amorphous Al_2O_3 and AlF_3 for Discovery of Battery Coatings. *J. Phys. Chem. C* **2013**, *117* (16), 8009–8013. https://doi.org/10.1021/jp311982d.

(36) Thibault-Starzyk, F.; Seguin, E.; Thomas, S.; Daturi, M.; Arnolds, H.; King, D. A. Real-Time Infrared Detection of Cyanide Flip on Silver-Alumina NO_x Removal Catalyst. *Science* **2009**, *324* (5930), 1048–1051. https://doi.org/10.1126/science.1169041.

(37) Ehrhardt, K. M.; Coleman, J. M.; Gu, Y.; Kim, H. S.; Donley, C. L.; Warren, S. C. Freestanding 2D Glasses by Atomic Layer Deposition. *ACS Appl. Mater. Interfaces* **2025**, *17* (13), 20042–20050. https://doi.org/10.1021/acsami.4c18918.

(38) Kresse, G.; Hafner, J. *Ab Initio* Molecular Dynamics for Liquid Metals. *Phys. Rev. B* **1993**, *47* (1), 558–561. https://doi.org/10.1103/PhysRevB.47.558.

(39) Furness, J. W.; Kaplan, A. D.; Ning, J.; Perdew, J. P.; Sun, J. Accurate and Numerically Efficient r^2SCAN Meta-Generalized Gradient Approximation. *J. Phys. Chem. Lett.* **2020**, *11* (19), 8208–8215. https://doi.org/10.1021/acs.jpclett.0c02405.

(40) Groner, M. D.; Fabreguette, F. H.; Elam, J. W.; George, S. M. Low-Temperature Al_2O_3 Atomic Layer Deposition. *Chem. Mater.* **2004**, *16* (4), 639–645. https://doi.org/10.1021/cm0304546.

(41) Davis, S.; Gutiérrez, G. Structural, Elastic, Vibrational and Electronic Properties of Amorphous Al_2O_3 from *Ab Initio* Calculations. *J. Phys.: Condens. Matter* **2011**, *23* (49), 495401. https://doi.org/10.1088/0953-8984/23/49/495401.

(42) Young, M. J.; Bedford, N. M.; Yanguas-Gil, A.; Letourneau, S.; Coile, M.; Mandia, D. J.; Aoun, B.; Cavanagh, A. S.; George, S. M.; Elam, J. W. Probing the Atomic-Scale Structure of Amorphous Aluminum Oxide Grown by Atomic Layer Deposition. *ACS Appl. Mater. Interfaces* **2020**, *12* (20), 22804–22814. https://doi.org/10.1021/acsami.0c01905.

(43) Lee, S. K.; Park, S. Y.; Yi, Y. S.; Moon, J. Structure and Disorder in Amorphous Alumina Thin Films: Insights from High-Resolution Solid-State NMR. *J. Phys. Chem. C* **2010**, *114* (32), 13890–13894. https://doi.org/10.1021/jp105306r.

(44) Nguyen, T. X.; Cohaut, N.; Bae, J.-S.; Bhatia, S. K. New Method for Atomistic Modeling of the Microstructure of Activated Carbons Using Hybrid Reverse Monte Carlo Simulation. *Langmuir* **2008**, *24* (15), 7912–7922. https://doi.org/10.1021/la800351d.

(45) Axel Kohlmeyer. The TopoTools VMD Plugin, 2017.

(46) Humphrey, W.; Dalke, A.; Schulten, K. VMD: Visual Molecular Dynamics. *J. Mol. Graph.* **1996**, *14* (1), 33–38. https://doi.org/10.1016/0263-7855(96)00018-5.

(47) Stukowski, A. Visualization and Analysis of Atomistic Simulation Data with OVITO–the Open Visualization Tool. *Modelling Simul. Mater. Sci. Eng.* **2010**, *18* (1), 015012. https://doi.org/10.1088/0965-0393/18/1/015012.

(48) Miao, J.; Ercius, P.; Billinge, S. J. L. Atomic Electron Tomography: 3D Structures without Crystals. *Science* **2016**, *353* (6306), aaf2157. https://doi.org/10.1126/science.aaf2157.

CHAPTER 5: THE STRUCTURE OF ALUMINA FROM ATOMIC LAYER

5.1 Introduction

Alumina deposition is often considered a model reaction for atomic layer deposition (ALD) due to its high reactivity and self-limiting nature. This process yields highly conformal materials with precisely controlled thickness, finding technological importance in a range of applications, such as stabilizing coatings in batteries,[1–3] heterogeneous catalysis,[4–6] and gate dielectrics in transistors.[7,8] Due to the popularity of ALD alumina, understanding its structure is a major goal. However, the amorphous nature of alumina from ALD requires approaches that do not rely on Bragg diffraction, presenting a significant challenge to structural characterization.

Because of this challenge, previous efforts to characterize amorphous alumina include a wide array of techniques. First-principles molecular dynamics revealed significant quantities of 5-coordinate Al (^{5}Al), in contrast to crystalline phases of Al_2O_3, which only consist of 4-coordinate (^{4}Al) and 6-coordinate Al (^{6}Al).[9] While these simulations agree qualitatively with experiment, reports have found that coordination number depends strongly on synthetic method, making the direct application of these insights to ALD alumina difficult.[10] Experimentally, solid-state ^{27}Al nuclear magnetic resonance (NMR) has been applied to gain insight into short-range order. ALD and plasma-enhanced ALD (PEALD) on Si substrates produced ^{4}Al : ^{5}Al : ^{6}Al ratios of 50:38:12 and 54:41:5, respecitively,[11,12] showing greater fractions of ^{5}Al than other thin film preparation methods such as electrochemistry and physical vapor deposition.[12–14] Others have used a combination of experimental and computational methods to solve for atomistic structures of Al_2O_3,

obtaining similar coordination numbers while gaining insight into structural features such as bond distance and electronic structure.[11,15,16]

While these reports have contributed considerable insights to the structure of amorphous Al_2O_3, alumina made by ALD does not typically possess an Al_2O_3 stoichiometry. Instead, incomplete reactions between precursors result in embedded hydrogen. The quantity of hydrogen is dependent on the growth temperature, with higher temperatures leading to less hydrogen. For example, at 33 °C, the H content is 22%, while at 150 °C, it is 7%.[17,18] To model the effects of hydrogen contamination, Auger parameter shifts have been used to identify MD structures most consistent with experiment. However, Auger parameter shifts are influenced by a variety of factors, including bond angle and length, resulting in an under-constrained inverse problem. Thus, despite the importance of ALD alumina and interest in its structure, much remains unknown about its 3D atomistic structure. One approach to obtain atomistic structures is diffuse scattering with x-rays, neutrons, or electrons. Electron scattering is a compelling approach because the strong interactions between electrons and matter allow the acquisition of high-quality scattering data with small quantities of sample. However, even electrons exhibit poor scattering from light elements such as hydrogen..[19] Thus, even electron scattering measurements of ALD alumina lack adequate information about the position of hydrogen atoms within its structure. This challenge is well known for scattering-based strategies and is a reason why insights from other electron scattering techniques, such as atomic electron tomography, have been limited to systems with heavy elements.[20]

To address this limitation and to characterize the 3D atomistic structure of alumina with hydrogen, we have developed software[cite] that employs Hybrid Reverse Monte Carlo (HRMC). HRMC iteratively perturbs a structure with a Markov-chain Monte Carlo algorithm to fit

experimental scattering while simultaneously minimizing potential energy.[21] By considering energy, HRMC has been found to minimize high-energy configurations and produce structures that are more physically realistic. An added advantage of including energy, which is calculated by an interatomic potential, is that potentials can model the thermodynamics of extremely light atoms. In this way, a computational constraint on the positions of light atoms may be imposed. Here, our HRMC model employs a machine-learned interatomic potential to calculate energy, thus constraining hydrogen sites with DFT-level accuracy. The resulting structures exhibit differences in local coordination geometries, as determined by fingerprinting methods. The difference in structure of alumina with hydrogen demonstrates the critical importance of modeling accurate compositions to understand amorphous material structures and discover structure-property relationships.

5.2 Methods

5.2.1 Alumina preparation and TEM characterization

To examine the structural effects of hydrogen in ALD alumina, we prepared two samples with varying concentrations of H. These samples were deposited on NaCl substrates at 33 °C and 150 °C, producing materials with a nominal thickness of 5 nm and H concentration of approximately 22 at.% and 7 at.%, respectively.[17,18] Following deposition, the samples were transferred onto grids for transmission electron microscopy (TEM) as freestanding materials using a previously described strategy.[22] TEM imaging showed clean and uniform thin films, while the selected area diffraction patterns and the corresponding pair distribution functions (PDFs) indicate that both samples lack long-range order and are therefore amorphous (Figure 5.1). In HRMC, the scattering fit is determined by the residual between the experimental PDF and the PDF of the calculated structure. Therefore, the PDFs in Figure 5.1c were used for our calculations.

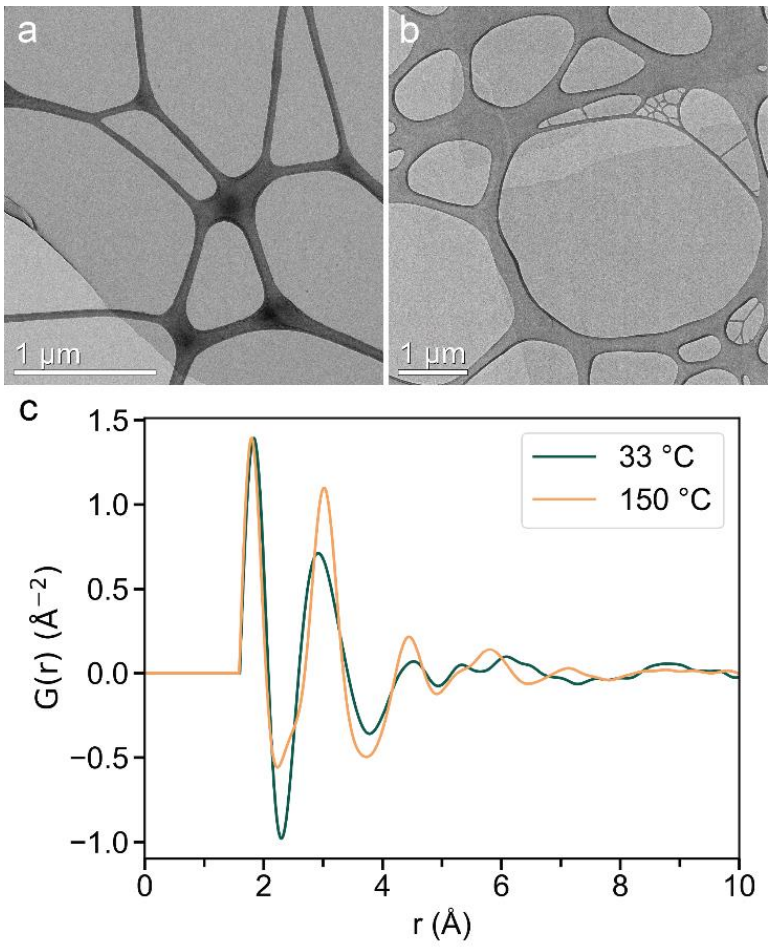


Figure 5.1. (a,b) Bright-field TEM images of ~5 nm-thick alumina prepared by ALD at (a) 33 °C and (b) 150 °C. (c) Pair distribution functions of the ALD alumina at both temperatures.

5.2.2 HRMC calculations

For each sample, we performed HRMC with and without hydrogen. By doing so, we aimed to determine the differences that emerge when hydrogen is accounted for in the structures. For each HRMC simulation, the composition was fixed at the outset of the structure solution process, because HRMC exclusively uses atomic translations, not the addition or removal of atoms, to perturb the structure. The initial aluminum oxide was prepared by expanding α-Al_2O_3 to a density of 2.9 g/cm^3, within the typical range of densities for ALD alumina, to yield a 51.5 nm slab with

1920 atoms (768 Al and 1152 O). Both initial aluminum hydroxide structures were created by expanding AlO(OH) and removing O and H atoms to achieve the correct stoichiometries. Previous studies have found that the O/Al ratio changes slightly with growth temperature, yielding a ratio of 1.7 at low temperatures (33 °C) and 1.6 at high temperatures (150 °C). Thus, we prepared compositions of 1152 Al:1800 O:640 H and 1152 Al:1800 O:210 H, for low and high temperatures, respectively. Densities for both structures were 3.0 g/cm^3.

HRMC calculations were performed under nearly identical condition with the pyHRMC package, which has been described in detail in chapter four. For all calculations, initial temperatures (T) and σ values of 2000 K and 0.4 were used, respectively. The following exponential quenching schemes were used to gradually decrease T and σ and impose increasingly strict constraints as the calculations progressed:

$$T_{n+1} = T_n \cdot q_T^n \quad (5\text{-}1),$$

$$\sigma_{n+1} = \sigma_n \cdot q_\sigma^n \quad (5\text{-}2).$$

where $q_T = q_\sigma = 0.9999$.

An additional important setting in HRMC are coordination constraints, which restrict coordination numbers in the structure. Along with the energy minimization term, this constraint is useful for minimizing unreasonable coordination environments. The pairwise coordination constraints for the aluminum oxide and hydroxide structures are included in Table 5.1. These coordination numbers were selected on the basis of previous ^{27}Al NMR experiments and the constraints that best replicated amorphous Al_2O_3 from molecular dynamics in chapter four.[12,23]

Table 5.1 The coordination number constraints for HRMC calculations of aluminum oxide and hydroxide.

		Neighbor atoms				
Center atom	Aluminum Oxide			Aluminum Hydroxide		
	Al	O	H	Al	O	H
Al	0	4-5	-	0	4-5	0
O	2-4	0	-	2-4	0	1
H	-	-	-	0	1	0

5.3 Results and Discussion

5.3.1 Convergence of PDF residual and energy

Using the conditions described in section 5.2, we performed HRMC calculations of aluminum oxide and aluminum hydroxide for each sample. The convergence of our calculations is shown in Figure 5.2a and 5.2b, where the residuals are decreasing for all calculations. Once converged, these values are expected to fall within the range of typical converged HRMC calculations, between 0.5-10.0.[24–26] The energy of the structure displays an initial increase for all calculations, followed by a decrease or plateau. This behavior is expected, given that atoms must move into transition states to escape the crystalline ordering of the initial structure. Once atoms are sufficiently disturbed and can enter amorphous local coordination environments, the energy decreases correspondingly. As seen in Figure 5.2c and 5.2d, the structures adopt a disordered appearance, consistent with the lack of long-range order in the experimental PDFs.

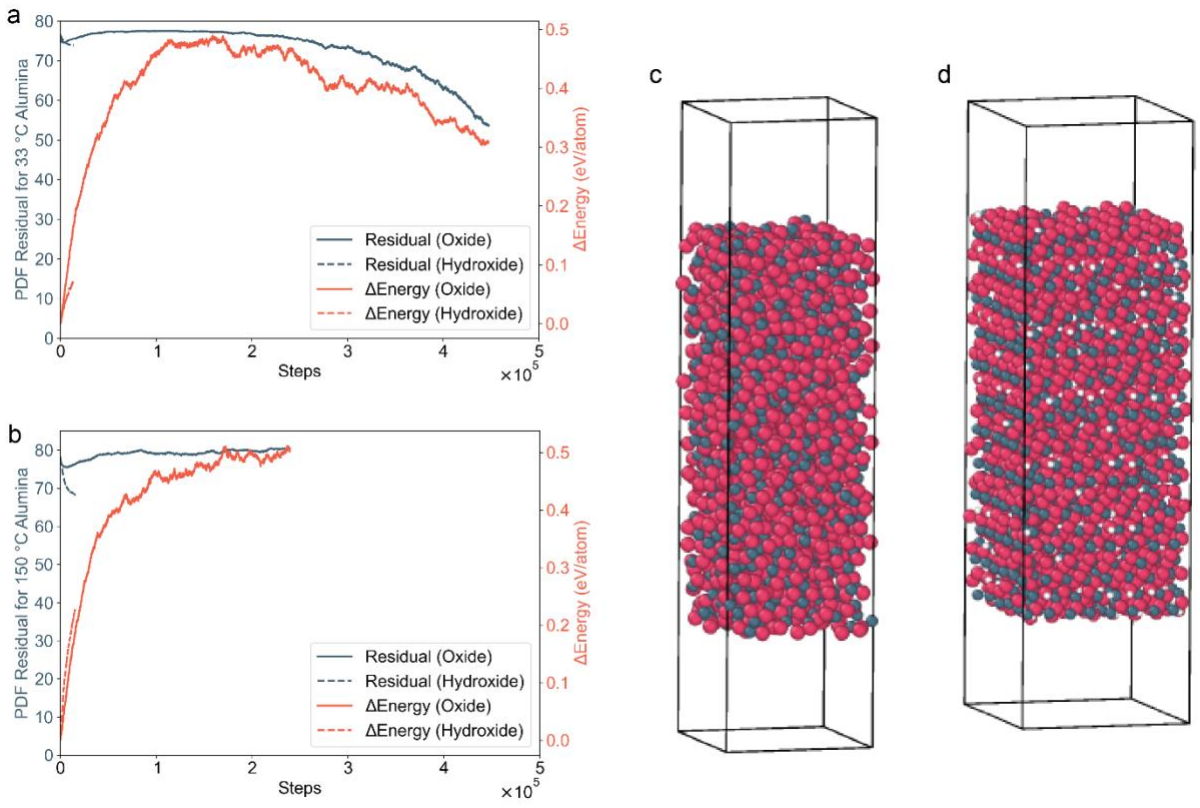


Figure 5.2. Convergence of PDF residual and energy in alumina oxide and aluminum hydroxide HRMC with the samples deposited at (a) 33 °C and (b) 150 °C. Structure cells at the most recent step for simulations on 33 °C alumina using (c) aluminum oxide and (d) aluminum hydroxide.

Interestingly, the hydroxide calculations for both samples show a greater initial decrease in PDF residual compared to the oxide calculations and despite similar or lower energies. We suggest that this trend may arise from the difference in vacancies between the two structures. Because the aluminum hydroxide crystal was prepared by removing atoms from AlO(OH), a large number of vacancies are available at the beginning of the calculation. Atoms may move into these vacancy sites with relatively low energetic cost compared to the initial aluminum oxide structure, in which similar vacancies are not present. This interpretation is somewhat supported by the coordination

number distributions after 16,000 steps for both calculations of the 33 °C sample, where the hydroxide exhibits wider distributions of Al and O coordination, particularly at low coordination numbers (<4 for Al and <3 for O) that are not observed in disordered or crystalline alumina (Figure 5.3). Thus, this behavior is not necessarily an effect of using a more accurate composition of aluminum hydroxide. However, the introduction of vacancies may be a useful general strategy for accelerating HRMC calculations.

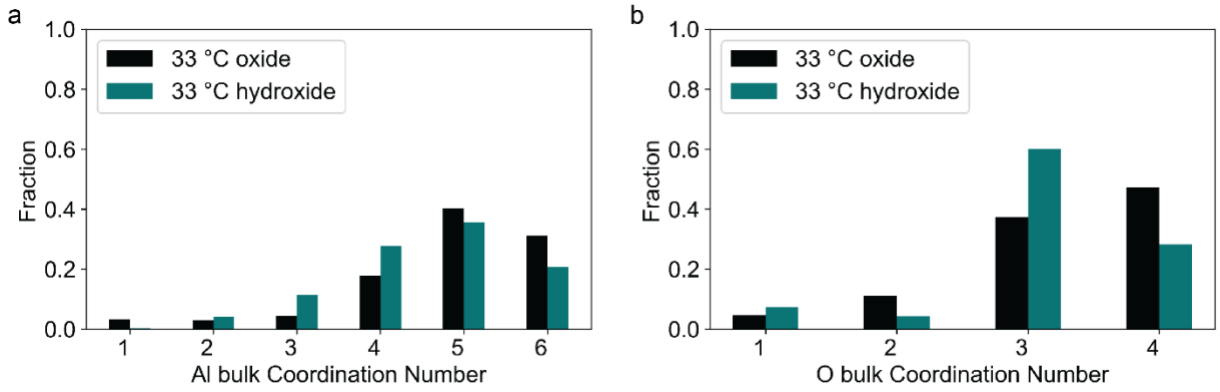


Figure 5.3. (a,b) The HRMC coordination number distributions of (a) Al and (b) O in aluminum oxide and hydroxide for ALD alumina prepared at 33 °C, after 16,000 steps.

5.3.2 Structural effects of hydrogen in alumina

Despite the similar calculation progress observed in our calculcations thus far, noticeable differences emerge upon closer examination of the atomistic structures. To perform this investigation, we performed fingerprinting analysis of the local coordination geometries (Figure 5.4). Coordination geometry fingerprints were obtained using the CrystalNNFingerprint in matminer.[27–29] Fingerprinting was performed on a site-by-site basis for all atoms. Each fingerprint consists of a vector of local structure order parameters, such as tetrahedral or trigonal bipyramidal, and indicates the similarity of the site's coordination environment to each order parameter. The

statistics of the site fingerprints were determined for each atom type with the PartialSiteStatsFingerprint class.[28]

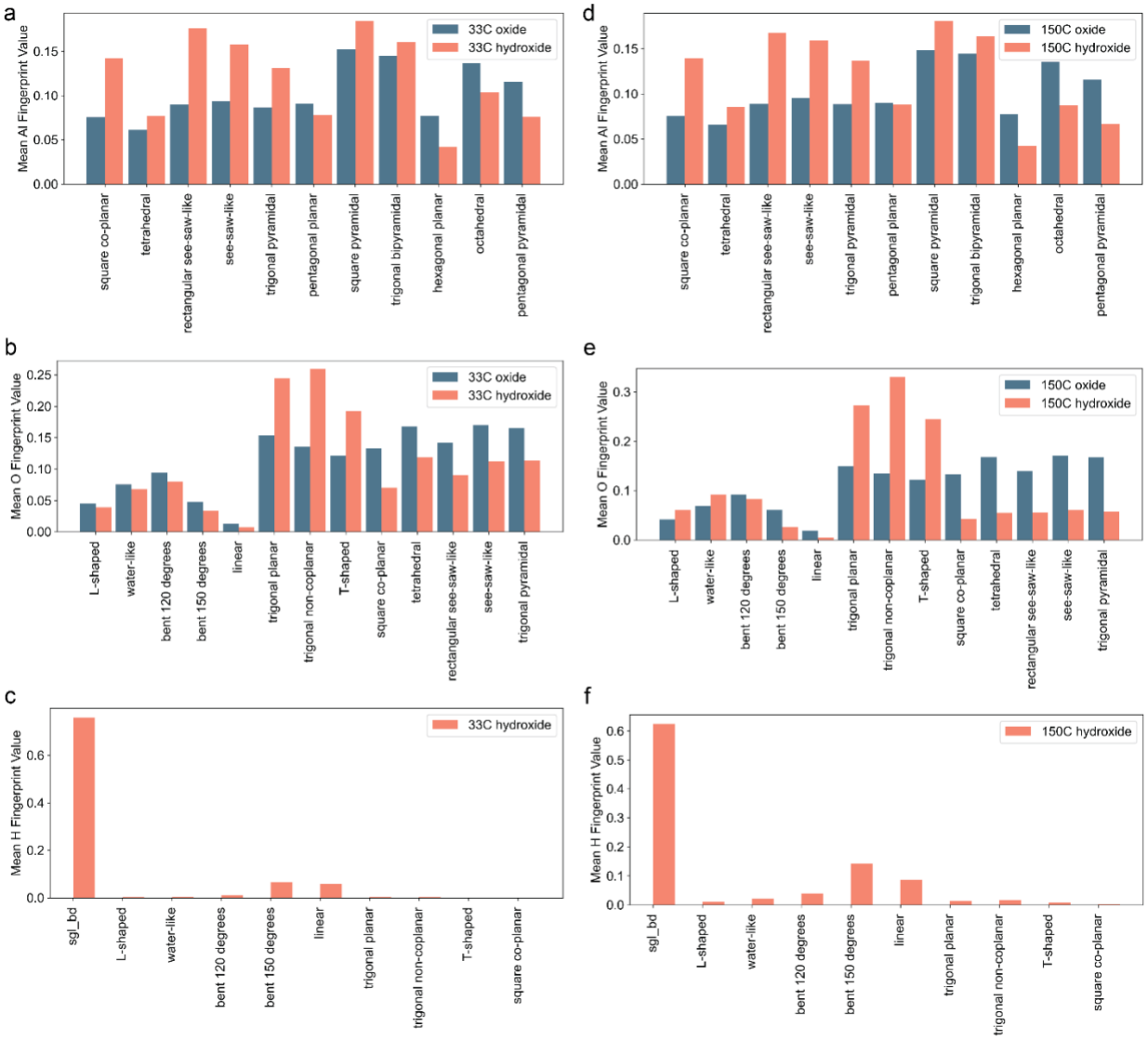


Figure 5.4. The CrystalNNFingerprints in 33 °C alumina of (a) Al, (b) O, and (c) H and in 150 °C alumina in (d) Al, (e) O, and (f) H. The visualized distributions have been limited to 3-6 for Al and 2-4 for O for clarity. Because H did not have a fingerprint from the Al_2O_3 structure, only the H fingerprints of hydroxide structures have been plotted.

Similar differences between the oxide and hydroxide structures can be observed at low and high temperatures (Figure 5.4). For example, the hydroxide exhibits significantly larger fingerprint weights for three-coordinate O geometries than the oxide. Beyond coordination number, different relative intensities of the three-coordinate geometries can be observed between the aluminum oxides and hydroxides. Three-coordinate O is not observed in crystalline forms of Al_2O_3 or AlO(OH) and has been suggested to play a role in glass-forming ability.[23] Understanding the geometries that form to produce such unique coordination numbers may provide insight into the speciic structure-property relationships involved. Once the calculations are converged, further analysis will be performed to make quantitative comparisons of structure.

5.4 Conclusions

ALD, which provides advantages such as ultrathin film thickness and conformal growth, is a popular choice for alumina fabrication. Despite the wide applications of ALD alumina, the structure-property relationships of the material are not fully understood. This knowledge gap exists in large part because of the confounding challenges of a disordered structure and hydrogen contamination in the material. In this study, we employed HRMC calculations to investigate the atomistic structure of amorphous ALD alumina with hydrogen. By applying energy-based computational constraints to our calculations, we obtained experimentally-derived structures of contaminated alumina.

These calculations revealed notable structural differences when performed with experimentally measured levels of hydrogen content, indicating that hydrogen imposes nontrivial effects on the local structure of atoms. Given the known importance of certain coordination structures to the performance of amorphous materials, our findings highlight the importance of accounting for hydrogen contamination when modeling the structure of ALD alumina.

Additionally, the atomistic models provided by our HRMC calculations demonstrate opportunities in discovering structure-property relationships that were previously unattainable. By moving beyond coordination number and obtaining insight into the geometries that give rise to notable properties, our strategy offers an avenue for the rational design of amorphous nanomaterials across applications, from batteries to transistors.

REFERENCES

(1) Woo, J. H.; Trevey, J. E.; Cavanagh, A. S.; Choi, Y. S.; Kim, S. C.; George, S. M.; Oh, K. H.; Lee, S.-H. Nanoscale Interface Modification of $LiCoO_2$ by Al_2O_3 Atomic Layer Deposition for Solid-State Li Batteries. *J. Electrochem. Soc.* **2012**, *159* (7), A1120–A1124. https://doi.org/10.1149/2.085207jes.

(2) Feng, Y.; Tao, R.; Livingston, K.; Sharma, J.; Cullen, D. A.; Lu, Y.; Steenman, W.; Groner, M.; Dameron, A.; Polizos, G.; Li, J. Comprehensive Evaluation of Commercially Scalable Atomic-Layer-Deposited Alumina Coating Impact on Full Cell Battery Performance across Varied Test Conditions. J. *Energy Storage* **2024**, *100*, 113711. https://doi.org/10.1016/j.est.2024.113711.

(3) Yu, M.; Wang, A.; Wang, Y.; Li, C.; Shi, G. An Alumina Stabilized ZnO–Graphene Anode for Lithium Ion Batteries via Atomic Layer Deposition. *Nanoscale* **2014**, *6* (19), 11419–11424. https://doi.org/10.1039/C4NR02576H.

(4) Yi, H.; Du, H.; Hu, Y.; Yan, H.; Jiang, H.-L.; Lu, J. Precisely Controlled Porous Alumina Overcoating on Pd Catalyst by Atomic Layer Deposition: Enhanced Selectivity and Durability in Hydrogenation of 1,3-Butadiene. *ACS Catal.* **2015**, *5* (5), 2735–2739. https://doi.org/10.1021/acscatal.5b00129.

(5) Weng, Z.; Zaera, F. Atomic Layer Deposition (ALD) as a Way to Prepare New Mixed-Oxide Catalyst Supports: The Case of Alumina Addition to Silica-Supported Platinum for the Selective Hydrogenation of Cinnamaldehyde. *Top. Catal.* **2019**, *62* (12–16), 838–848. https://doi.org/10.1007/s11244-019-01163-4.

(6) Ahn, S.; Littlewood, P.; Liu, Y.; Marks, T. J.; Stair, P. C. Stabilizing Supported Ni Catalysts for Dry Reforming of Methane by Combined La Doping and Al Overcoating Using Atomic Layer Deposition. *ACS Catal.* **2022**, *12* (17), 10522–10530. https://doi.org/10.1021/acscatal.2c02599.

(7) Kim, J. B.; Fuentes-Hernandez, C.; Potscavage, W. J.; Zhang, X.-H.; Kippelen, B. Low-Voltage InGaZnO Thin-Film Transistors with Al_2O_3 Gate Insulator Grown by Atomic Layer Deposition. *Appl. Phys. Lett.* **2009**, *94* (14), 142107. https://doi.org/10.1063/1.3118575.

(8) Zhang, X.-H.; Domercq, B.; Wang, X.; Yoo, S.; Kondo, T.; Wang, Z. L.; Kippelen, B. High-Performance Pentacene Field-Effect Transistors Using Al_2O_3 Gate Dielectrics Prepared by Atomic Layer Deposition (ALD). *Org. Electron.* **2007**, *8* (6), 718–726. https://doi.org/10.1016/j.orgel.2007.06.009.

(9) Davis, S.; Gutiérrez, G. Structural, Elastic, Vibrational and Electronic Properties of Amorphous Al_2O_3 from *Ab Initio* Calculations. *J. Phys.: Condens. Matter* **2011**, *23* (49), 495401. https://doi.org/10.1088/0953-8984/23/49/495401.

(10) Gleizes, A. N.; Samélor, D.; Vahlas, C.; Sarou-Kanian, V.; Florian, P.; Massiot, D. Temperature Dependent 4-, 5- and 6-Fold Coordination of Aluminum in MOCVD-Grown

Amorphous Alumina Films: From Local Coordination to Material Properties. *Adv. Sci. Technol.* **2014**, 91, 123–133. https://doi.org/10.4028/www.scientific.net/AST.91.123.

(11) Harper, A. F.; Emge, S. P.; Magusin, P. C. M. M.; Grey, C. P.; Morris, A. J. Modelling Amorphous Materials via a Joint Solid-State NMR and X-Ray Absorption Spectroscopy and DFT Approach: Application to Alumina. *Chem. Sci.*, **2023**, 14, 1155. https://doi.org/10.1039/d2sc04035b.

(12) Lee, S. K.; Park, S. Y.; Yi, Y. S.; Moon, J. Structure and Disorder in Amorphous Alumina Thin Films: Insights from High-Resolution Solid-State NMR. *J. Phys. Chem. C* **2010**, *114* (32), 13890–13894. https://doi.org/10.1021/jp105306r.

(13) Farnan, I.; Dupree, R.; Forty, A. J.; Jeong, Y. S.; Thompson, G. E.; Wood, G. C. Structural Information about Amorphous Anodic Alumina from ^{27}Al MAS NMR. *Philos. Mag. Lett.* **1989**, *59* (4), 189–195. https://doi.org/10.1080/09500838908206342.

(14) Farnan, I.; Dupree, R.; Jeong, Y.; Thompson, G. E.; Wood, G. C.; Forty, A. J. Structural Chemistry of Anodic Alumina. *Thin Solid Films* **1989**, *173* (2), 209–215. https://doi.org/10.1016/0040-6090(89)90136-3.

(15) Young, M. J.; Bedford, N. M.; Yanguas-Gil, A.; Letourneau, S.; Coile, M.; Mandia, D. J.; Aoun, B.; Cavanagh, A. S.; George, S. M.; Elam, J. W. Probing the Atomic-Scale Structure of Amorphous Aluminum Oxide Grown by Atomic Layer Deposition. *ACS Appl. Mater. Interfaces* **2020**, *12* (20), 22804–22814. https://doi.org/10.1021/acsami.0c01905.

(16) Shi, C.; Alderman, O. L. G.; Berman, D.; Du, J.; Neuefeind, J.; Tamalonis, A.; Weber, J. K. R.; You, J.; Benmore, C. J. The Structure of Amorphous and Deeply Supercooled Liquid Alumina. *Front. Mater.* **2019**, *6*, 38. https://doi.org/10.3389/fmats.2019.00038.

(17) Dingemans, G.; Van De Sanden, M. C. M.; Kessels, W. M. M. Influence of the Deposition Temperature on the C-Si Surface Passivation by Al_2O_3 Films Synthesized by ALD and PECVD. *Electrochem. Solid-State Lett.* **2010**, *13* (3), H76. https://doi.org/10.1149/1.3276040.

(18) Groner, M. D.; Fabreguette, F. H.; Elam, J. W.; George, S. M. Low-Temperature Al_2O_3 Atomic Layer Deposition. *Chem. Mater.* **2004**, *16* (4), 639–645. https://doi.org/10.1021/cm0304546.

(19) Ehrhardt, K. M.; Radomsky, R. C.; Warren, S. C. Quantifying the Local Structure of Nanocrystals, Glasses, and Interfaces Using TEM-Based Diffraction. *Chem. Mater.* **2021**, *33* (23), 8990–9011. https://doi.org/10.1021/acs.chemmater.1c03017.

(20) Miao, J.; Ercius, P.; Billinge, S. J. L. Atomic Electron Tomography: 3D Structures without Crystals. *Science* **2016**, *353* (6306), aaf2157. https://doi.org/10.1126/science.aaf2157.

(21) Opletal, G.; Petersen, T.; O'Malley, B.; Snook, I.; McCulloch, D. G.; Marks, N. A.; Yarovsky, I. Hybrid Approach for Generating Realistic Amorphous Carbon Structure Using Metropolis and Reverse Monte Carlo. *Mol. Simul.* **2002**, *28* (10–11), 927–938. https://doi.org/10.1080/0892702040000025584.

(22) Ehrhardt, K. M.; Coleman, J. M.; Gu, Y.; Kim, H. S.; Donley, C. L.; Warren, S. C. Freestanding 2D Glasses by Atomic Layer Deposition. *ACS Appl. Mater. Interfaces* **2025**, *17* (13), 20042–20050. https://doi.org/10.1021/acsami.4c18918.

(23) Lee, S. K.; Ryu, S. Probing of Triply Coordinated Oxygen in Amorphous Al_2O_3. *J. Phys. Chem. Lett.* **2018**, *9* (1), 150–156. https://doi.org/10.1021/acs.jpclett.7b03027.

(24) Farmahini, A. H.; Opletal, G.; Bhatia, S. K. Structural Modelling of Silicon Carbide-Derived Nanoporous Carbon by Hybrid Reverse Monte Carlo Simulation. *J. Phys. Chem. C* **2013**, *117* (27), 14081–14094. https://doi.org/10.1021/jp403929r.

(25) Jain, S. K.; Pellenq, R. J.-M.; Pikunic, J. P.; Gubbins, K. E. Molecular Modeling of Porous Carbons Using the Hybrid Reverse Monte Carlo Method. *Langmuir* **2006**, *22* (24), 9942–9948. https://doi.org/10.1021/la053402z.

(26) Nguyen, T. X.; Cohaut, N.; Bae, J.-S.; Bhatia, S. K. New Method for Atomistic Modeling of the Microstructure of Activated Carbons Using Hybrid Reverse Monte Carlo Simulation. *Langmuir* **2008**, *24* (15), 7912–7922. https://doi.org/10.1021/la800351d.

(27) Zimmermann, N. E. R.; Jain, A. Local Structure Order Parameters and Site Fingerprints for Quantification of Coordination Environment and Crystal Structure Similarity. *RSC Adv.* **2020**, *10* (10), 6063–6081. https://doi.org/10.1039/C9RA07755C.

(28) Ward, L.; Dunn, A.; Faghaninia, A.; Zimmermann, N. E. R.; Bajaj, S.; Wang, Q.; Montoya, J.; Chen, J.; Bystrom, K.; Dylla, M.; Chard, K.; Asta, M.; Persson, K. A.; Snyder, G. J.; Foster, I.; Jain, A. Matminer: An Open Source Toolkit for Materials Data Mining. *Computational Materials Science* **2018**, *152*, 60–69. https://doi.org/10.1016/j.commatsci.2018.05.018.

(29) Pan, H.; Ganose, A. M.; Horton, M.; Aykol, M.; Persson, K. A.; Zimmermann, N. E. R.; Jain, A. Benchmarking Coordination Number Prediction Algorithms on Inorganic Crystal Structures. *Inorg. Chem.* **2021**, *60* (3), 1590–1603. https://doi.org/10.1021/acs.inorgchem.0c02996.